Implementation of Coherent Raman Detected Electron Paramagnetic Resonance

by
Jörg Gutschank

Fachbereich Physik
Universität Dortmund

A thesis submitted for the degree of
Doktor der Naturwissenschaften

revised edition
January 2005

Abstract

The technique of coherent Raman (optically) detected electron paramagnetic resonance (ODEPR), is a relatively new method for the investigation of electronic structure. In this thesis the technique is implemented with a microwave frequency of 35 GHz for the first time.

Two continuous wave (cw) ODEPR spectrometers have been built (14 and 35 GHz). Pulsed microwave excitation is possible at 14 GHz.

The application to ruby demonstrates the working of the technique and the equipment.

When ODEPR is used to analyse metalloproteins, conventional methods like electron paramagnetic resonance (EPR) and magnetic circular dichroism (MCD) are additionally needed. These have also been implemented and they are demonstrated on myoglobin (Mb).

Contents

1 Introduction **6**

2 Theory **8**
2.1 Microwave Modulated MCD 9
2.1.1 EPR 10
2.1.2 MCD 12
2.1.3 Rotating MCD 13
2.2 Coherent Raman Detected EPR 17
2.2.1 General Idea 17
2.2.2 Perturbation Treatment 18
2.3 Pulse Techniques 21
2.3.1 Optically detected saturation recovery 22
2.3.2 Coherent pulse ODEPR 22

3 Samples **24**
3.1 Ruby 24
3.1.1 The Guinea Pig 24
3.1.2 35 GHz ODEPR Sample 25
3.2 Myoglobin 26
3.2.1 Introduction 26
3.2.2 Sample Preparation 27

4 Established Methods **30**
4.1 Magnetic Circular Dichroism 30
4.1.1 MCD Spectrometer 30
4.1.2 MCD Spectra 32
4.2 Electron Paramagnetic Resonance 43

5 Continuous wave ODEPR **46**
5.1 14 GHz ODEPR Spectrometer 46
5.2 35 GHz ODEPR Spectrometer 49

5.2.1 Spectrometer Overview 50
5.2.2 Microwave Cavity 52
5.2.3 Optical Heterodyne Detection 59
5.2.4 Signal-To-Noise Ratio 60
5.3 Automatic Frequency Control 66
5.3.1 General Idea 66
5.3.2 Implementation 67
5.4 ODEPR Spectra 69
5.4.1 Introduction 69
5.4.2 Wavelength Dependence 76

6 Pulsed Microwave Excitation **83**
6.1 Optically detected saturation recovery 83
6.2 Conventionally Detected Pulse EPR 87

7 Summary and Future Prospects **89**
7.1 Conclusion 89
7.2 Outlook 90

A Design Drawings **91**
A.1 Changes to the MCD Spectrometer 91
A.2 35 GHz Spectrometer 94
A.2.1 35 GHz Bridge 94
A.2.2 35 GHz Probe 94
A.2.3 Slide Screw Tuner 96

B Electrical Components **100**
B.1 Electrical Circuitry of the AFC-system 100
B.2 Microwave Parts 103
B.2.1 35 GHz 103
B.2.2 14 GHz 105
B.3 Modelling the Cylindrical Cavity 107

C Myoglobin MCD Data **110**

List of Figures

2.1 A double resonance experiment. 8
2.2 The double resonant ODEPR signal. 9
2.3 Precessing magnetisation. 10
2.4 EPR absorption and dispersion. 11
2.5 C-term MCD. 13
2.6 MCD of rotating transverse magnetisation. 13
2.7 ODEPR lineshapes contain orientational information. 16
2.8 Coherent Raman scattering from a three level system. 17
2.9 $\Lambda_{123}(\omega_L, \omega_{MW})$ 20
2.10 Optically detected saturation recovery. 22

3.2 Optical absorbance of different ruby samples 25
3.1 Definition of α 25
3.3 Structure of Myoglobin 27
3.4 Absorption of reduced and oxidised Myoglobin 28
3.5 Glassing of Hepes with ethanediol 29

4.1 MCD Spectrometer 31
4.2 MCD of Mb 2 32
4.3 MCD overview 33
4.4 MCD spectra for different magnetic fields 36
4.5 MCD amplitudes vs. magnetic field 36
4.6 MCD spectra for different temperatures. Magnetic field 1.5 T. 37
4.7 MCD amplitudes versus temperature. 37
4.8 Soret band MCD spectra of sample V 38
4.9 Soret band MCD spectra for different temperatures 39
4.10 Soret band MCD masterplot 39
4.11 Soret band MCD of sample V at high temperature 40
4.12 Gaussian fit to MCD of Mb 2 41
4.13 MCD and light sources 43
4.14 EPR of Mb 1, 1.6 K 44

4.15 EPR of Mb 1, 20 K 45

5.1 Experimental setup for 14 GHz ODEPR 47
5.2 Overview of the 35 GHz spectrometer. 50
5.3 Field distribution of the TE_{011} cylindrical cavity mode 52
5.4 Mode chart for a cylindrical microwave resonator. 53
5.5 Coupling to the TE_{011} cylindrical cavity mode. 54
5.6 Voltage reflection coefficient S_{11} from the $R = 7$ mm cavity . . 55
5.7 Calculated mode frequencies for $R = 7$ mm 56
5.8 Calculated mode frequencies for $R = 5.6$ mm 57
5.9 Relative power reflected from the microwave cavity. 58
5.10 Noise spectrum of the fully assembled 35 GHz receiver 61
5.11 Receiver arm of the 35 GHz spectrometer. 62
5.12 Gain of the first 3 stages of the heterodyne receiver 64
5.13 Modulating the Dip 66
5.14 Overview of the AFC system. 68
5.15 Co-ordinate system 69
5.16 Energy splitting of the ground state of ruby 70
5.17 35 GHz ODEPR spectra of ruby sample I 72
5.18 Laser power dependence of 35 GHz ODEPR 73
5.19 Microwave power dependence of 35 GHz ODEPR 74
5.20 ODEPR absorption saturated 75
5.21 Predicted ODEPR of the R_2-line of ruby 77
5.22 Fitted ODEPR of ruby I at $\lambda = 692.159$ nm 80
5.23 ODEPR of ruby I at $\lambda = 692.072$ nm and $\lambda = 692.126$ nm . . 81
5.24 Fit result of 35 GHz ODEPR 82

6.1 Experimental set-up for ODSR 84
6.2 ODSR of Ruby 85
6.3 Temperature dependence of Ruby ODSR 86
6.4 Pulse Sequence for T_2 measurements 86
6.5 Echo Decay for Ruby 3 88
6.6 Echo Decay for Ruby I 88

A.1 Overview MCD Spectrometer 92
A.2 Shielding of the Magnetic Field 93
A.3 35 GHz Bridge 95
A.4 35 GHz Cavity 96
A.5 Overview 35 GHz Probe 97
A.6 Slide screw tuner. 98

B.1 11 kHz Phase Shifter. 100

B.2 AFC circuit diagram, part 1 101
B.3 AFC circuit diagram, part 2 102
B.5 Power on Microwave Counter 104
B.4 Output Power from Bridge 104
B.6 Voltage response of diodes 105
B.7 Three dimensional model of the cylindrical microwave cavity. . 107
B.8 Simulated cavity resonances compared to analytical modes . . 108
B.9 Electric fields of the TE_{011} mode 109

C.1 Myoglobin MCD 110

Chapter 1

Introduction

Magnetic resonance experiments can be improved in several ways by means of laser radiation [1]. One such technique is set up and further improved in this thesis.

Optically detected electron paramagnetic resonance (ODEPR) combines advantages of electron paramagnetic resonance (EPR) and magnetic circular dichroism (MCD) to make a coherent Raman scattering experiment. A review can be found elsewhere [2]. We have successfully applied the ODEPR technique to metalloproteins for the first time [3, 4] and provided a theoretical description as MCD detected EPR [5] and as a coherent Raman process [6]. The experimental results on haemoproteins like cytochrome [3, 5], blue copper centres in azurin [7], the high-spin iron-protein rubredoxin [8], and iron-sulfur clusters in ferredoxin have already demonstrated the potential of ODEPR to investigate the electronic structure of paramagnetic metal centres in proteins. Some of these results have been obtained with the hardware, which was build in the course of this thesis.

In this thesis the implementation of ODEPR is described and the technique is applied to the test system ruby. Two continuous wave (cw) ODEPR spectrometers (14 GHz and 35 GHz) and a spectrometer for pulsed microwave excitation have been built. The extension to a microwave pulsed technique promises the possibility to measure also time resolved.

For the interpretation of ODEPR spectra of metalloproteins, EPR as well as MCD have been useful in the past [7, 8], but could not be measured with our previous experimental equipment. These additional techniques have therefore been implemented. They are demonstrated on myoglobin (Mb). Metalloproteins are also the systems, for which the development of the ODEPR technique is intended finally.

EPR is a sensitive probe of the electronic structure of paramagnetic metal ions and is therefore used extensively to probe the active centre of metallo-

proteins [9]. ODEPR is an extension of EPR, which uses a laser beam for detection instead of the direct detection of the absorption or dispersion of the microwave field. It can be related to more conventional optically detected magnetic resonance (ODMR) techniques. In contrast to those, it uses coherent Raman scattering of the laser beam and optical heterodyne detection of the scattered Raman light to detect the EPR signal.

In magnetic resonance experiments, light can be used to enhance the polarisation, to influence the dynamics of the spin system, and, as in the experiment described here, to improve the detection. In suitable systems, optical detection provides a number of advantages: first, optical radiation introduces an additional resonance condition, which can be used to distinguish different signal components and thereby separate the target signal from backgrounds such as impurities. Second, optical radiation can be detected with single photon sensitivity (in contrast to microwave radiation). This has made detection of single spins possible in suitable systems. A third possible use of the optical radiation is that the laser beam breaks the symmetry of isotropic samples, such as powders or frozen solutions. This allows one to derive the orientation of tensorial interactions, such as electron g-tensors or optical anisotropy tensors from non-oriented samples.

Many different methods have been developed to exploit the advantages of optical detection for magnetic resonance [10]. In particular, magnetic resonance of electronically excited states [11] usually requires optical excitation of the sample to populate the excited states. Other techniques measure changes in the MCD [12] or other magneto-optical effects while sweeping through an EPR. The coherent ODEPR technique was first suggested by Dehmelt [13] and realized on alkali vapours [14]. Bloembergen and coworkers suggested an extension to solids [15], which was implemented by Bingham et al. for ruby [16].

It is the aim of this thesis to demonstrate the implementation of the ODEPR technique, in particular at a microwave frequency of 35 GHz, which, to best of my knowledge, is the highest frequency used for ODEPR so far.

The thesis begins with the theoretical description of the experiment. The two theories about ODEPR, which both have been developed in our group, are explained in Chapter 2. Then the two samples, which were investigated, are briefly introduced in Chapter 3, before the conventional techniques EPR and MCD are applied to Mb in Chapter 4. Chapter 5 introduces the ODEPR spectrometers built during this thesis and the 35 GHz measurements on ruby. The possibility to use pulsed microwave excitation is exploited in Chapter 6 for the measurement of relaxation times of ruby. The final chapter gives a conclusion. More details, needed to build an ODEPR spectrometer, can be found in the Appendix.

Chapter 2

Theory

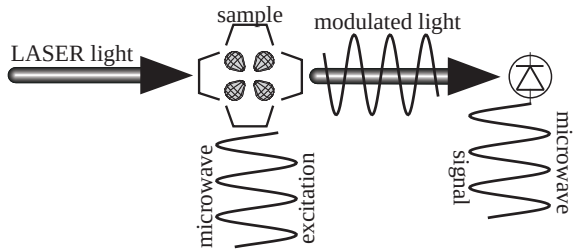

Figure 2.1: The sample is irradiated with laser light and microwaves. The mixed frequency signal is detected by a fast photodiode. The output of the detector is a microwave signal.

ODEPR is a coherent double resonance experiment.

The sample is simultaneously irradiated with microwaves and laser light, which are tuned to an optical and a magnetic dipole transition in the sample. In order to lift the degeneracy of the Zeeman levels, the substance is placed in a magnetic field. If the laser and microwave fields are both resonant with a transition in the sample, the transmitted laser beam is modulated at the microwave frequency. This modulation is picked up by a fast photodiode (see Figure 2.1). The resulting signal can phase-sensitively be down converted (lock-in detected) with microwaves to yield the ODEPR signal.

The resulting signal depends on the optical frequency or wavelength λ as well as on the microwave frequency or the magnetic field B_0 (see Figure 2.2). The signal is maximal when both resonance conditions are fulfilled and it decreases, when either excitation becomes off-resonant.

Two complementary theoretical models exist for analysing the microscopic processes underlying this experiment. While the description as microwave modulated MCD [5] is more intuitive and easier to visualise, the second theory describing ODEPR as coherent Raman scattering [6] makes less assumptions about the system under investigation. It applies without restriction to high spin systems and to sharp resonance lines. The former

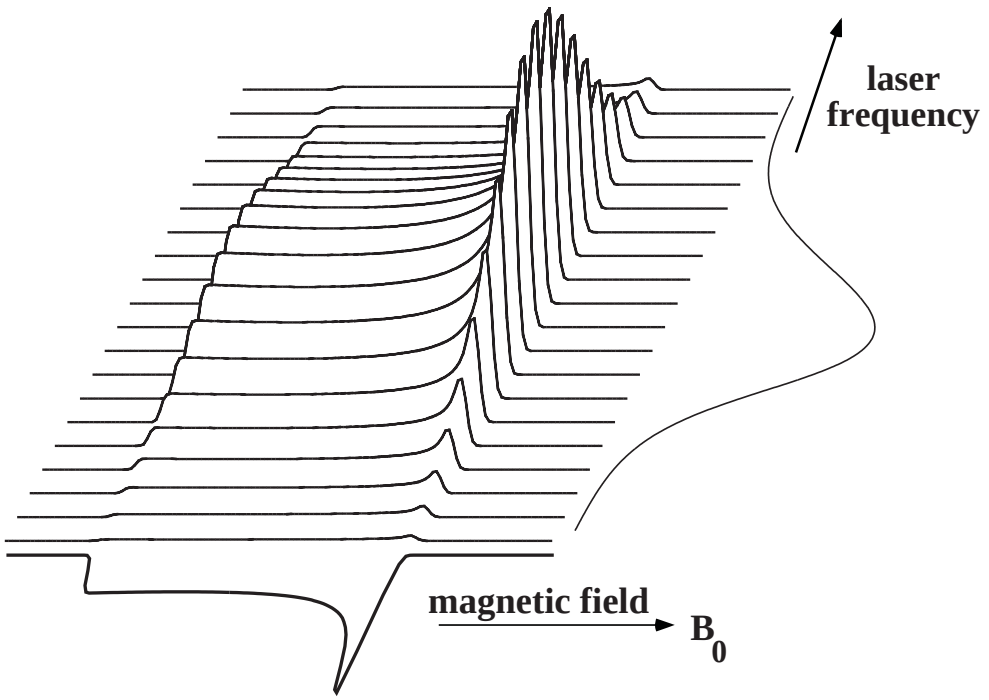

Figure 2.2: The double resonant ODEPR signal depends on the laser as well as the microwave frequency. The result is a complete microwave resonance spectrum for each laser wavelength. The 2 dimensional projections on the axes are cuts through the main resonance at the peaks of the optical and the microwave transitions respectively. The figure was calculated from an ODEPR absorption of an axial system. It is a powder average, as it would be for a frozen aqueous solution of a metalloprotein.

theory has been applied to metalloproteins [5, 7, 8] already, while the latter was only tested on a single crystal: ruby [6].

Both views are presented, before pulsed microwave experiments are discussed.

2.1 Microwave Modulated MCD

The theory of microwave modulated MCD combines two standard techniques for the investigation of electronic structure of paramagnetic metal centres: magnetic circular dichroism (MCD) and electron paramagnetic resonance (EPR). A basic understanding of both these methods is therefore necessary to understand this view on ODEPR.

2.1.1 EPR

EPR [17] investigates the resonance frequency of a precessing magnetisation of a sample under the influence of microwave radiation and a slowly varying magnetic field.

Basics

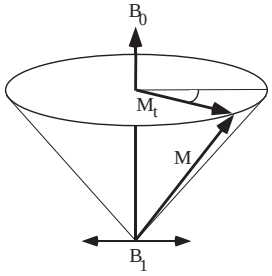

Figure 2.3: The magnetisation M of a paramagnetic sample in a static magnetic field B_0 is precessing. It is kept in continuous precession at a fixed angle to B_0 by a microwave field B_1 oscillating at the Larmor frequency. EPR measures the amplitude of the component M_t transverse to the static field.

Unpaired electrons, e.g. in transition metal ions, possess a magnetic moment

$$\boldsymbol{\mu} = \gamma\hbar\boldsymbol{J} = -g\mu_B\boldsymbol{J} \ , \qquad (2.1)$$

where $\hbar$ is Planck's constant and γ is the gyromagnetic ratio consisting of the spectroscopic splitting factor or g-value g, and the Bohr magneton μ_B. The total angular momentum $\boldsymbol{J}$ (in units of $\hbar$) consists of orbital and spin contributions. The magnetisation $\boldsymbol{M}$ is the vector sum per unit volume of all magnetic moments.

Application of a magnetic field $\boldsymbol{B_0}$ exerts a torque

$$\hbar\frac{d\,\boldsymbol{J}}{dt} = \frac{1}{\gamma}\frac{d\,\boldsymbol{\mu}}{dt} = \boldsymbol{\mu} \times \boldsymbol{B_0} \qquad (2.2)$$

on $\boldsymbol{\mu}$. This equation describes that the magnetic moments $\boldsymbol{\mu}$ (and therefore also $\boldsymbol{M}$) precess around $\boldsymbol{B_0}$ with the angular velocity $\omega_L = \frac{g\mu_B}{\hbar}B_0$, which is referred to as the Larmor frequency. The free precession is damped by relaxation and $\boldsymbol{M}$ would eventually end up aligned with $\boldsymbol{B_0}$. In order to obtain a continuous precession one has to resonantly apply energy to the system. Microwave radiation of amplitude $\boldsymbol{B_1}$ polarised perpendicular to $\boldsymbol{B_0}$ with an angular velocity $\omega_{MW} = \omega_L$ can be used to keep $\boldsymbol{M}$ at precession around $\boldsymbol{B_0}$ (Figure 2.3). In an EPR experiment the frequency of the microwave radiation ω_{MW} is kept constant, while the strength of the magnetic field B_0 is slowly varied, in order to find the field, where the EPR resonance condition

$$\hbar\omega_{MW} = g\mu_B B_0 \qquad (2.3)$$

is fulfilled, so that the precession can be observed. A signal proportional to a transverse component $\boldsymbol{M_t}$ of the magnetisation (or a derivative thereof)

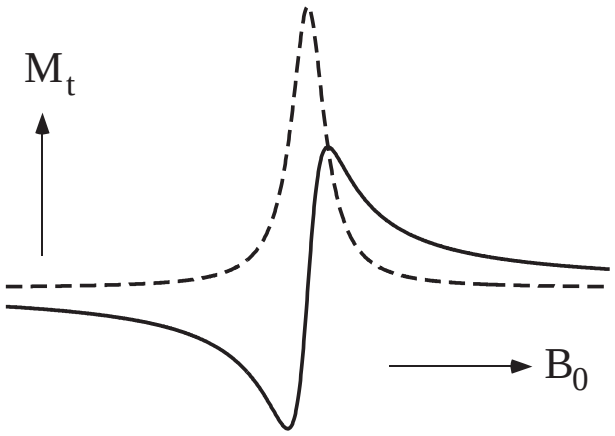

Figure 2.4: Transverse magnetisation as a function of magnetic field B_0. Depending on the detection phase relative to the excitation microwave field B_1, the signal shows an absorption (dashed line) or dispersion (solid line). Conventional EPR spectrometers usually detect the derivatives of these signals.

perpendicular to the magnetic field $\boldsymbol{B_0}$ is measured as a function of B_0. The result is an absorption or dispersion curve, depending on the relative phase of excitation and detection (Figure 2.4). The two signals are proportional to projections of the rotating M_t, which are 90° out of phase relative to each other: when B_0 fulfils Equation 2.3, the absorption signal reaches a maximum in Figure 2.4, while the dispersion signal goes through zero.

Information content

In the simplest case of a free electron, the g-factor has the value $g_f = 2.00232$. In all chemically interesting applications, the electron is in an atomic or molecular orbital and its magnetic moment has contributions from orbital as well as spin degrees of freedom. The g-factor deviates therefore from the free electron value in a way that is characteristic for its environment. In addition, the g-value depends on the orientation of the magnetic field with respect to the local environment of the unpaired electron: the g-value is then a second rank tensor with three principal values g_x, g_y, and g_z [17], where the index refers to the direction of the principal axes. In disordered systems like powders or frozen solutions, the anisotropy of the g-tensor can lead to very broad lines. The principal values of the g-tensor can then be identified by the position of the maximum at the highest and lowest g-values.

The environment of the electron also includes nuclear spins, which couple

to the electron via hyperfine interaction. These couplings split or broaden the EPR lines and are quantified by the hyperfine coupling constant A. Both these dependencies on the environment of the paramagnetic site make EPR spectroscopy a versatile tool for the determination of electronic as well as spatial structure.

A widely used application is the introduction of spin-labels [18] to systems which do not show EPR by themselves. g-values as well as hyperfine coupling constants are sensitive to the orientation of the label relative to the field. Further, hyperfine coupling can give information about the mobility of the spin-label and thus about the dynamics of the system.

Also in inorganic biochemistry EPR is extensively used not only to detect specific metal ions (e.g. 1 μM Fe^{3+} in solution at room temperature), but also for its sensitivity to the surrounding of the ion [19]. EPR can for instance distinguish between 3 different types of copper centres and some proteins contain all of them. Clarification of such a complex situation by EPR and optical spectroscopy was a milestone in inorganic biochemistry [19]. The redox states Fe^{2+} and Fe^{3+} of iron both exist in high- and low-spin states, which can clearly be distinguished by EPR and the g-value gives further information on the surrounding ligands. Consequently EPR was often used to study haems and iron-sulfur clusters. Many other transition metal ions in proteins and enzymes are investigated also by EPR. Sometimes also organic residues in the neighbourhood of metal centres give an EPR signal, like the stable tyrosyl radical.

Variants of EPR, like electron nuclear double resonance and electron spin echo envelope modulation [20] make the identification of hyperfine interaction with the ligands (superhyperfine interaction) easier and are also often used for the investigation of paramagnetic centres and their surroundings.

2.1.2 MCD

Magnetic circular dichroism (MCD) refers to the differential absorbance ΔA of left vs. right circularly polarised light in the presence of a magnetic field. Like optical absorption, it is a resonant phenomenon, but since it can have positive as well as negative sign, it often provides significantly higher resolution than the pure absorption spectrum.

MCD theory [21, 22, 23, 24] distinguishes three terms A, B, C contributing to the spectrum. In paramagnetic samples like ruby or metalloproteins at low temperature the strongly temperature dependent C term usually dominates the other two. Figure 2.5 illustrates the principle for an idealised spin-1/2 system: the static magnetic field in the direction of a beam of circularly polarised light lifts the degeneracy of the two opposite spin states and a

population difference between them is established according to Boltzman's law. Circularly polarised light couples only to one of the two spin states, as indicated by the arrows in Figure 2.5. The thermal population difference therefore implies that the polarisation that couples to the lower energy state is absorbed more strongly than the opposite polarisation.

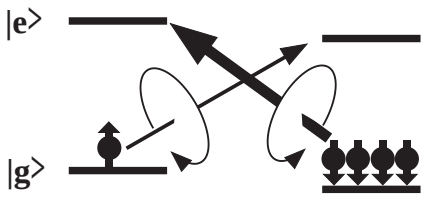

Figure 2.5: C-term MCD. Optical excitation with two opposite circular polarisations from the electronic ground state $|g\rangle$ to the excited state $|e\rangle$ of a paramagnetic sample in a magnetic field. One polarisation finds more electrons of the respective spin than the other.

In a typical MCD experiment ΔA is measured as a function of optical wavelength at fixed magnetic field and for several fixed temperatures. The resulting spectra are characteristic for the surrounding of a metal centre in, for instance, a metalloprotein and can therefore be considered as fingerprints.

Circular dichroism can be induced not only by magnetic fields, but also by other effects that generate a net spin polarisation, such as optical pumping [25] or by transverse magnetisation excited by microwave irradiation, as described in the following.

2.1.3 Rotating MCD

In the model of microwave modulated MCD, a paramagnetic sample in a static magnetic field is considered.

The sample is continuously irradiated with resonant microwaves. The system reaches a steady state with the magnetisation precessing at the microwave frequency around the static field. As explained in Section 2.1.1, a conventional continuous wave EPR experiment measures the component M_t of this magnetisation perpendicular to the magnetic field. In the ODEPR experiment, the same component of the magnetisation is instead probed by laser light. The conservation of angular momentum as a vector quantity during absorption implies that the absorptivity of the material de-

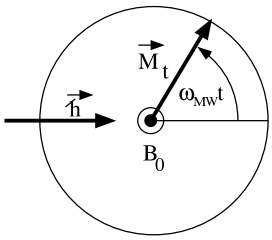

Figure 2.6: Continuous wave excitation of EPR creates a component of magnetisation M_t transverse to the static magnetic field B_0 (perpendicular to the plane of drawing). The MCD of M_t is probed with circularly polarised photons with an angular momentum of $\hbar$.

pends on the instantaneous orientation of the electronic angular momentum. As shown in Figure 2.6, the precessing magnetisation modulates the circular dichroism and therefore the absorptivity of the sample at the microwave frequency.

The resulting signal is therefore proportional to the EPR signal as well as to the MCD of the sample. This effect is completely analogous to MCD, where the circular dichroism due to the magnetisation parallel to the magnetic field is probed, as mentioned in Section 2.1.2.

We have already verified the proportionality of the ODEPR signal to the MCD signal for ruby and for the metalloprotein cytochrome c elsewhere [26, 3]. In the absence of saturation, the proportionality constant between a conventional MCD intensity and the ODEPR signal can be estimated from the EPR parameters:

$$\frac{M_t}{M_z} = \omega_{\mathrm{Rabi}} T_2 \tag{2.4}$$

where M_t is the transverse magnetisation and M_z is the longitudinal magnetisation. ω_{Rabi} is the Rabi angular velocity and T_2 is the phase memory time. This relation follows from the description of EPR with the Bloch equations. The difference in absorbance between left and right circularly polarised light for ODEPR and MCD, $\Delta A_{\mathrm{ODEPR}}$ and ΔA_{MCD}, are proportional to the respective magnetisation component, so that also

$$\frac{\Delta A_{\mathrm{ODEPR}}}{\Delta A_{\mathrm{MCD}}} = \omega_{\mathrm{Rabi}} T_2 \ . \tag{2.5}$$

Information content

The signal generated in the ODEPR experiment depends on the optical as well as on the magnetic resonance condition. The additional resonance condition, compared to conventional EPR spectroscopy, provides a possible mechanism for distinguishing different paramagnetic centres. This is particularly important when pure samples are difficult or impossible to obtain.

Besides the chemical selectivity, the double resonance technique also provides the possibility to obtain information about the orientation of the g-tensor in the molecule. The principle of this is illustrated in Figure 2.7. The lineshape of the ODEPR spectrum (Figure 2.7 c, d) differs significantly from that of the conventional EPR spectrum (Figure 2.7 e). The difference arises from an orientational selectivity: The contribution of every molecule to the total signal is weighted with its MCD sensitivity for the direction of propagation of the laser beam. If a given molecule has the highest MCD sensitivity

along the molecular z-axis (Figure 2.7 a, b), the main signal contribution (Figure 2.7 c) arises from molecules whose z-axis is oriented perpendicular to the static magnetic field. For these molecules, the resonant magnetic field is determined by their g_x and g_y values. The signal intensity is then reduced around the g_z position of the spectrum, since the laser beam hardly sees MCD intensity for molecules with g_z along B_0 (Figure 2.7 a). This is in contrast to conventional EPR, where MCD sensitivity does not come into play (Figure 2.7 e).

To calculate the spectra quantitatively we have developed a theory that combines EPR (to calculate spectral positions) and MCD (to calculate the amplitude). Here only the case of an axially symmetric system is discussed, where the difference of the extinction coefficients $\Delta\epsilon_x$ (x indicating transverse to B_0) for circularly polarised light is [4, 5, 8]

$$\Delta\epsilon_x \propto \int_0^{\pi/2} \sin\theta d\theta\, T(\theta) f(\theta) \left[C_z g_z \frac{g_\perp^2}{g^2} \sin^2\theta + C_\perp g_\perp \left(\frac{g_z^2}{g^2} \cos^2\theta + 1 \right) \right] . \quad (2.6)$$

Here θ is the angle between the molecular z-axis and the static magnetic field, $T(\theta) = \tanh(g(\theta)\mu_B B_0/2kT)$ is the Boltzmann factor, and $f(\theta)$ describes the transverse magnetisation as a function of molecular orientation, amplitude and frequency of the microwave field. $g_\perp$ and g_z are the principal values of the g-matrix perpendicular to and along the molecular z-axis and $g^2 = g_z^2 \cos^2\theta + g_\perp^2 \sin^2\theta$. $C_\perp$ and C_z are the principal values of the optical anisotropy tensor, which describes the MCD sensitivity.

To obtain the g and C values and the orientation from the experimental spectrum, we fit the conventional as well as the optically detected EPR spectrum with the same parameter set. For the additional analysis, it is convenient to calculate the ratio

$$\frac{C_\perp}{C_z} = \tan\gamma$$

which parametrises the direction of the optical anisotropy with respect to the g-tensor axis.

A comparison of ODEPR spectra measured at different optical wavelengths shows strong variations of the amplitude and lineshapes of the spectra. This variation arises because the optical anisotropy tensor C is a characteristic property of each optical transition. As the laser interacts with different transitions, the optical anisotropy changes and, according to Equation 2.6, also the ODEPR spectrum.

To obtain the anisotropy parameters for each optical transition, first the orientation γ is evaluated as a function of the optical frequency ν. Then this

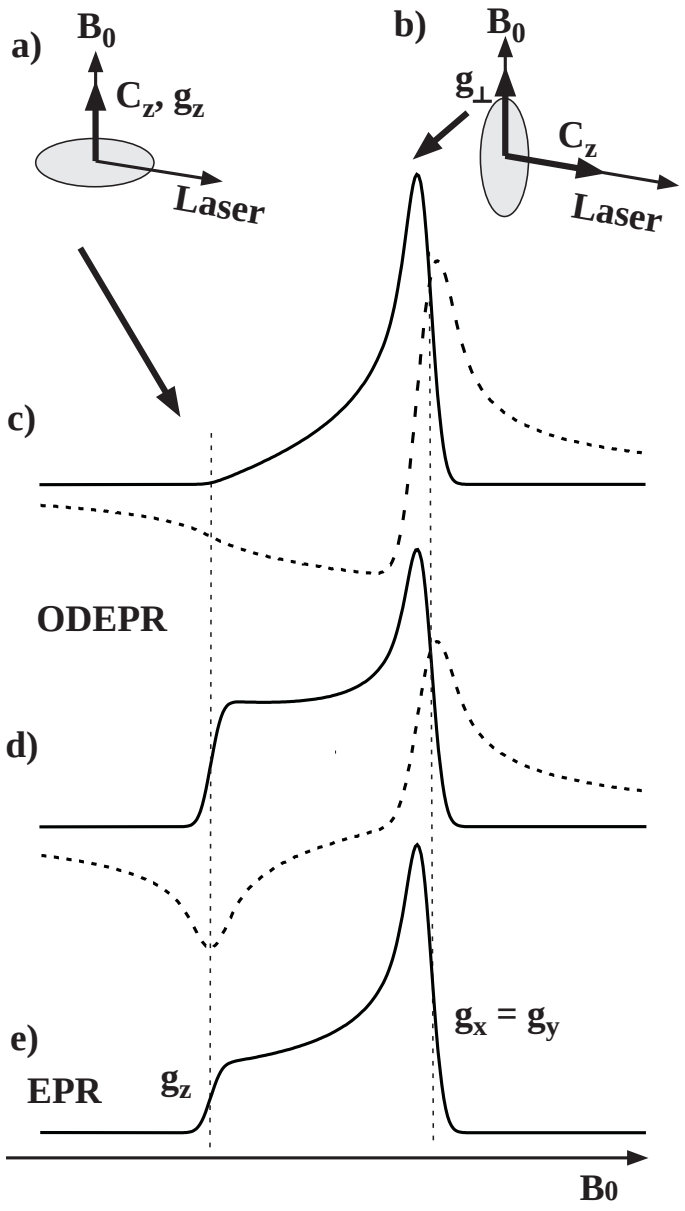

Figure 2.7: ODEPR lineshapes contain orientational information. C_z represents MCD sensitivity in molecular z-direction and the shaded disk represents the plane of the axially symmetric molecule. a) Molecules with MCD sensitivity only along their z-axis do not contribute, when the z-axis is perpendicular to the laser beam. b) They contribute strongly when the z-axis is parallel to the laser beam. c) Calculated ODEPR absorption (solid line) and dispersion (dashed line) of an axially symmetric molecule with MCD sensitivity along its z-axis only. d) Calculated ODEPR when the MCD sensitivity is only perpendicular to the z-axis. e) Calculated conventional EPR absorption. [7, 2]

angle is fitted together with the measured MCD $\Delta\epsilon_z$ (z indicating parallel to B_0) to a sum of contributions i from each optical transition at position p_i with width w_i,

$$\Delta\epsilon_z(\nu) = \sum_i \Delta\epsilon_{zi} e^{-(\nu-p_i)^2/2w_i^2} \tag{2.7}$$

and the orientation angles

$$\gamma(\nu) = \arctan\left(\frac{\sum_i C_{\perp i}\ e^{-(\nu-p_i)^2/2w_i^2}}{\sum_i C_{zi}\ e^{-(\nu-p_i)^2/2w_i^2}}\right) \tag{2.8}$$

Such an analysis has already been demonstrated for 14 GHz ODEPR of azurin [7] and rubredoxin [8]. This successful application to metalloproteins is a strong motivation, to develop the ODEPR technique further, theoretically as well as experimentally.

2.2 Coherent Raman Detected EPR

Our description of the ODEPR experiment as coherent Raman scattering [6] has not yet been applied to metalloproteins quantitatively. It is included here for the analysis of ruby. It is more general than the rotating MCD picture and provides additional insight into the microscopic processes that generate the observed signal.

2.2.1 General Idea

We consider again an EPR transition of a paramagnetic sample in a magnetic field driven by a microwave field, while a laser field is applied in resonance with an optical transition.

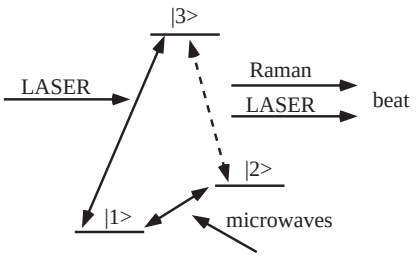

Figure 2.8: Coherent Raman scattering from a 3 level system.

Figure 2.8 shows the three quantum mechanical states that are involved in the process. The microwave field interacts with the transition between levels $|1\rangle$ and $|2\rangle$, while the optical field excites the transition between $|1\rangle$ and $|3\rangle$. The combination of the two fields creates a coherent superposition of states $|2\rangle$ and $|3\rangle$. (This means that the quantum mechanical wave function is a linear combination of the two separate wave functions.)

Physically, the coherence in an optical transition like $|2\rangle \leftrightarrow |3\rangle$ represents the source of an optical field. This additional field propagates parallel to the incident laser field. Its frequency is equal to the sum or difference of the laser and microwave frequencies. The process is known as coherent Raman scattering [27].

Since the two coherent optical fields propagate in the same direction, they are superimposed on the detector and create a beat signal at the difference frequency, which is equal to the frequency of the microwave field applied to the sample.

2.2.2 Perturbation Treatment

The ODEPR signal from a real system can often be viewed as a superposition of Raman scattering processes. The 3 level model, which is described in detail here, suffices to describe one such process. When a particular system is considered, we have to sum over contributions from many such processes.

We consider the interaction of the 3 level system in Figure 2.8 with the laser and microwave fields as a perturbation potential $V(t)$ with the two non-vanishing components

$$\begin{aligned} V_{12}(t) &= -\boldsymbol{\mu}_{12}^{\mathrm{mag}} \boldsymbol{B_1} \left(e^{-i\omega_{\mathrm{MW}}t} + e^{i\omega_{\mathrm{MW}}t}\right) \\ V_{13}(t) &= -\boldsymbol{\mu}_{13}^{\mathrm{el}} \left(\boldsymbol{E}'_{\mathrm{L}} e^{-i\omega_{\mathrm{L}}t} + \boldsymbol{E}'^{*}_{\mathrm{L}} e^{i\omega_{\mathrm{L}}t}\right) \end{aligned} \tag{2.9}$$

for the microwave and laser fields respectively. $\boldsymbol{\mu}_{12}^{\mathrm{mag}}$ and $\boldsymbol{\mu}_{13}^{\mathrm{el}}$ are the magnetic and electric dipole moments of the respective transitions. The microwave field $\boldsymbol{B_1}$ is linearly polarised and described by a real variable, while the electric vector $\boldsymbol{E}'_{\mathrm{L}}$ of the laser field is complex, in order to allow arbitrary polarisation. The Hamiltonian of the system can then be written as

$$\mathcal{H} = \mathcal{H}^0 + V(t) = \begin{pmatrix} E_1 & V_{12}(t) & V_{13}(t) \\ V_{21}(t) & E_2 & 0 \\ V_{31}(t) & 0 & E_3 \end{pmatrix} , \tag{2.10}$$

where the Hamiltonian $\mathcal{H}^0$ of the undisturbed system is given by the energies $E_{1,2,3}$ of the three states.

The time evolution of this system can be described with the density matrix $\rho(t)$. In analogy to similar problems in non-linear optics [28], $\rho(t)$ can be treated in second order perturbation theory. Then

$$\begin{aligned} \dot{\rho}_{nm}^{(0)} &= i\omega_{nm}\rho_{nm}^{(0)} - \gamma_{nm}\left(\rho_{nm}^{(0)} - \rho_{nm}^{eq}\right), \\ \dot{\rho}_{nm}^{(1)} &= \left(i\omega_{nm} - \gamma_{nm}\right)\rho_{nm}^{(1)} - \frac{i}{\hbar}\left[V(t), \rho^{(0)}\right]_{nm}, \\ \dot{\rho}_{nm}^{(2)} &= \left(i\omega_{nm} - \gamma_{nm}\right)\rho_{nm}^{(2)} - \frac{i}{\hbar}\left[V(t), \rho^{(1)}\right]_{nm}, \end{aligned} \tag{2.11}$$

where the upper index indicates the order in the perturbation calculation, γ_{nm} is the relaxation rate from $|n\rangle$ to $|m\rangle$, and $\omega_{nm} = (E_m - E_n)/\hbar$ is the angular velocity of the transition.

The result of the first order perturbation calculation yields

$$\rho_{12}^{(1)} = \rho_{21}^{(1)*} = \left(\rho_{11}^{(0)} - \rho_{22}^{(0)}\right) \omega_R \left[\frac{e^{-i\omega_{MW}t}}{\omega_{12} + \omega_{MW} + i\gamma_{12}} + \frac{e^{i\omega_{MW}t}}{\omega_{12} - \omega_{MW} + i\gamma_{12}}\right], \tag{2.12a}$$

$$\rho_{13}^{(1)} = \rho_{31}^{(1)*} = \frac{1}{\hbar}\left(\rho_{11}^{(0)} - \rho_{33}^{(0)}\right) \left[\frac{\boldsymbol{\mu}_{13}^{el}\boldsymbol{E}'_L e^{-i\omega_L t}}{\omega_{13} + \omega_L + i\gamma_{13}} + \frac{\boldsymbol{\mu}_{13}^{el}\boldsymbol{E}'^{*}_L e^{i\omega_L t}}{\omega_{13} - \omega_L + i\gamma_{13}}\right], \tag{2.12b}$$

where $\omega_R = \boldsymbol{\mu}_{12}^{mag}\boldsymbol{B}_1/\hbar$ is the Rabi angular velocity. Equation (2.12a) describes the spin coherence of the transition $|1\rangle \leftrightarrow |2\rangle$ induced by the microwave field. Equation (2.12b) describes the optical coherence in transition $|1\rangle \leftrightarrow |3\rangle$ induced by the laser field. Optically anti-resonant terms like the first term in the square brackets of Equation (2.12b) are neglected in the following calculation, but terms that are anti-resonant with respect to the microwave frequency are taken into account.

The spin- and optical coherences are partially transferred to the third transition $|2\rangle \leftrightarrow |3\rangle$ in second order. We obtain the Raman coherence

$$\rho_{23}^{(2)} = \frac{\omega_R}{\hbar}\boldsymbol{\mu}_{13}^{el}\boldsymbol{E}'^{*}_L e^{i\omega_L t}\left[\Lambda_{123}(\omega_L, -\omega_{MW})e^{-i\omega_{MW}t} + \Lambda_{123}(\omega_L, \omega_{MW})e^{i\omega_{MW}t}\right], \tag{2.13}$$

with the two-dimensional triple-Lorentzian lines Λ_{123} defined as

$$\Lambda_{123}(\omega_L, \omega_{MW}) = \frac{1}{\omega_{23} - \omega_L - \omega_{MW} + i\gamma_{23}}\left\{\frac{\rho_{33}^{(0)} - \rho_{11}^{(0)}}{\omega_{13} - \omega_L + i\gamma_{13}} + \frac{\rho_{22}^{(0)} - \rho_{11}^{(0)}}{\omega_{21} - \omega_{MW} + i\gamma_{21}}\right\}. \tag{2.14}$$

The first factor of Equation 2.14 describes the resonant behaviour of the Raman wave with respect to transition $|2\rangle \leftrightarrow |3\rangle$: It reaches a maximum when the frequency $\omega_{s,as} = \omega_L + \omega_{MW}$ of the Raman field matches that of the transition frequency. The fractions in brackets describe the resonances of the laser and microwave with the transitions $|1\rangle \leftrightarrow |3\rangle$ and $|1\rangle \leftrightarrow |2\rangle$ respectively. Figure 2.9 shows the dependence of $\Lambda_{123}(\omega_L, \omega_{MW})$ on the microwave and laser frequencies. The magnetic resonances ($\omega_{21} - \omega_{MW} = 0$) and optical resonances ($\omega_{13} - \omega_L = 0$) appear on lines parallel to the frequency axes of the plot, while the Raman resonance appears along the diagonal $\omega_{23} - \omega_L - \omega_{MW} = 0$.

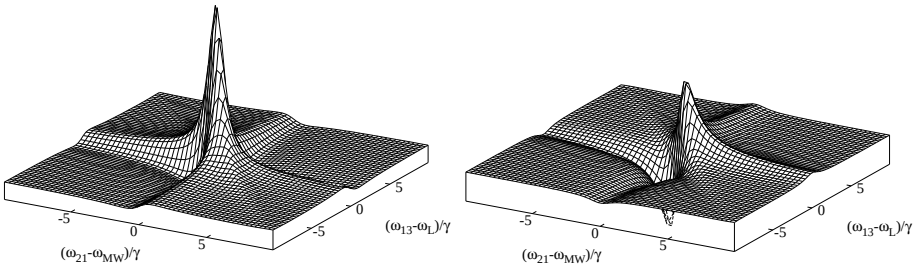

Figure 2.9: Microwave and laser frequency dependence of $\Lambda_{123}(\omega_L, \omega_{MW})$ in arbitrary units (with $\gamma = \gamma_{12} = \gamma_{13} = \gamma_{23}$ and equal population differences). Real part (left) and imaginary part (right) are shown.

The density operator element $\rho_{ij}^{(2)}$ corresponds to an optical polarisation

$$\begin{aligned} \boldsymbol{P}^{(2)} &= N\left(\rho_{23}^{(2)}\boldsymbol{\mu}_{32}^{el} + \rho_{32}^{(2)}\boldsymbol{\mu}_{23}^{el}\right) = \\ &= \left(\boldsymbol{P}_{as}e^{i(\boldsymbol{k}'_{as}\boldsymbol{r}-\omega_{as}t)} + cc\right) + \left(\boldsymbol{P}_{s}e^{i(\boldsymbol{k}'_{s}\boldsymbol{r}-\omega_{s}t)} + cc\right) \end{aligned} \tag{2.15}$$

with $\boldsymbol{k}'_{as,s} = \boldsymbol{k}_L \pm \boldsymbol{k}_{MW}$ and N the number density. Since the rotating wave approximation does not hold for the EPR transitions, we have to include Stokes- as well as anti-Stokes components. The polarisation (2.15) is the source of the Raman waves. We write $\boldsymbol{E}_\alpha e^{i(\boldsymbol{k}_\alpha \boldsymbol{r}-\omega_\alpha t)} + cc$ with $\alpha = L, s, as$ for the laser, Stokes, and anti-Stokes wave, respectively. The wave-vectors $\boldsymbol{k}_{as,s}$ of the Raman fields are functions of the Raman frequencies $\omega_{as,s} = \omega_L \pm \omega_{MW}$. Since the sample is small compared to the wavelength of the microwave, the Raman wave is emitted in the forward direction. It remains weak compared to the laser field, allowing us to use the linear expansion

$$\boldsymbol{E}_\alpha = \frac{i\omega_\alpha^2\mu_0}{2k_\alpha}\boldsymbol{P}_\alpha L \ ,$$

where L is the optical path length in the crystal. Using Equation (2.13) and (2.15), the two Raman waves become

$$E_\alpha = \frac{i\mu_0 L N \omega_R \omega_\alpha^2}{2\hbar k_\alpha}\left(\boldsymbol{\mu}_{31}^{el}\boldsymbol{E}_L\right)\boldsymbol{\mu}_{23}^{el}\Lambda_{123}^*(\omega_L, \pm\omega_{MW})$$

where the plus sign is for the anti-Stokes field and the minus for the Stokes field.

The optical fields at the end of the crystal contain components with frequencies ω_L and $\omega_L \pm \omega_{MW}$. The Raman waves are polarized along $\boldsymbol{\mu}_{23}^{el}$ and

$\boldsymbol{\mu}_{32}^{el}$, while the laser field is polarized along $\boldsymbol{E}_L$. When the signal is detected on a quadratic detector, it includes, besides a dominant dc component, components oscillating at the microwave frequency and its second harmonic. The first harmonic arises from beats between the laser field and each of the Raman sidebands, while the second harmonic is due to the beat between the two sidebands. The spatial components of the Raman field can be detected separately by projecting the (Raman plus laser) field onto a direction determined by a polarizer. Writing $\boldsymbol{E}^{(P)}$ for the fields behind the polarizer, the heterodyne signal at the microwave frequency becomes

$$I(\omega_{MW})^{(P)} = \Re\left[4\sqrt{\frac{\varepsilon_r\varepsilon_0}{\mu_0}}e^{-i\omega_{MW}t}\left(\boldsymbol{E}_{as}^{(P)}\boldsymbol{E}_L^{*(P)} + \boldsymbol{E}_s^{*(P)}\boldsymbol{E}_L^{(P)}\right)\right] \tag{2.16}$$

$$= \Re\left[\frac{i2LN\omega_R\omega_L}{\hbar}e^{-i\omega_{MW}t}\left\{\left(\boldsymbol{\mu}_{31}^{el}\boldsymbol{E}_L\right)\left(\boldsymbol{\mu}_{23}^{el(P)}\boldsymbol{E}_L^{(P)*}\right)\Lambda_{123}^{*}(\omega_L,\omega_{MW})\right.\right.$$

$$\left.\left. - \left(\boldsymbol{\mu}_{13}^{el}\boldsymbol{E}_L^{*}\right)\left(\boldsymbol{\mu}_{32}^{el(P)}\boldsymbol{E}_L^{(P)}\right)\Lambda_{123}(\omega_L,-\omega_{MW})\right\}\right]$$

where the approximation $\omega_{as} \simeq \omega_s \simeq \omega_L$ was made for the amplitudes.

Experimental considerations often make it desirable to measure the difference between two signals. One way to do so is by modulating the polarization of the light incident on the sample in combination with phase sensitive detection. In the ODEPR experiments of this thesis the light was modulated between left and right circularly polarised. The dot product of electric dipole moments and laser field in Equation 2.16 becomes then

$$\left(\boldsymbol{\mu}_{31}^{el}\boldsymbol{E}_L\right)\left(\boldsymbol{\mu}_{23}^{el(P)}\boldsymbol{E}_L^{(P)*}\right) = \frac{E_0^2}{2}\left(\mu_{31}^{+}\mu_{23}^{-} - \mu_{31}^{-}\mu_{23}^{+}\right) \tag{2.17}$$

where E_0 is the amplitude of the electrical laser field and $\mu_{ij}^{\pm}$ are the circularly polarised transition dipoles between levels j and i.

After phase sensitive detection, the signal consists of differences of intensities $I(\omega_{MW})^{(+,-)}$ for the two circular polarisations '+' and '−'.

2.3 Pulse Techniques

Pulse experiments are frequently used in magnetic resonance mainly due to their high temporal as well as spectral resolution. Pulse nuclear magnetic resonance is standard for many years, whereas in EPR pulse experiments are only possible for a couple of years due to the technical challenges. Often the relaxation times are so short (some 10 ns) that the 'ringing' of the electronic components overlaps with the desired signal.

In the case of optically detected pulse EPR we distinguish between incoherent techniques which are only concerned with population differences between the levels involved, and coherent techniques which are a straightforward extension of the coherent Raman scattering described in Section 2.2.

2.3.1 Optically detected saturation recovery

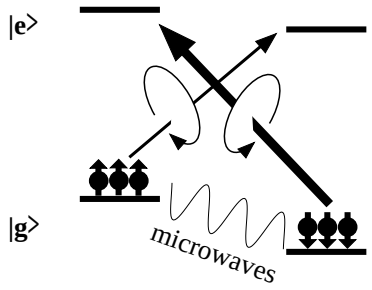

Figure 2.10: Optically detected saturation recovery. The ground state population is equalised with microwaves and absorption for both light polarisations becomes equally likely.

C-term MCD as described in Section 2.1.2 can be destroyed by equalising the ground state populations, so that the magnetisation is destroyed and transitions for both circular polarisations are equally likely.

The ground state populations can be equalised by application of a saturating microwave field as shown in Figure 2.10. This can for instance be done by a series of pulses of different duration until the MCD signal vanishes. At the end of the saturation period, thermal equilibrium is re-established within the recovery time T_1, which is the spin-lattice relaxation time. The MCD intensity ΔA is proportional to the recovering magnetisation:

$$\Delta A \propto M(t) = M_0 \left(1 - e^{-\frac{t}{T_1}}\right) , \tag{2.18}$$

where M_0 is the magnetisation in thermal equilibrium.

This method is concerned with population rather than coherence. It does not contain any phase information and is therefore considered as an incoherent method. Optically detected saturation recovery is used to measure T_1.

2.3.2 Coherent pulse ODEPR

Coherent transient studies of electronic as well as nuclear transitions have been demonstrated by Wei et. al. [29] on nitrogen-vacancy centres in diamond. They have demonstrated that versatile pulse magnetic resonance methods like transient nutation, rotary echo, free induction decay (FID), spin echo, delayed FID (inversion recovery), and spin-locking can be detected optically.

All these techniques are straightforward combinations of pulse EPR [30] and the coherent ODEPR technique. Wei et. al. use a coherent Raman picture, similar to the description in Section 2.2.

Pulse ODEPR techniques can yield a deeper understanding of the dynamics of light matter interaction, which cannot be obtained by cw measurements. We have therefore made first attempts to extend our ODEPR experiments to the time domain. In contrast to the low (30-150 MHz) frequency experiments of Wei et. al. we would work at 14 GHz, which leads to more demanding specifications of the optical receiver. The spectrometer described in Section 5.1 has been modified for pulse experiments in collaboration with Mirko Meier [31].

Chapter 3

Samples

Two different substances have been used for the experiments in this thesis: a ruby single crystal and aqueous solutions of the metalloprotein myoglobin.

3.1 Ruby

Ruby is a red, paramagnetic crystal. It consists of a corundum lattice Al_2O_3 with chromium Cr^{3+} impurities at lattice positions of aluminium ions. The rhombohedral unit cell contains 6 anions and 4 cations and has 3 fold rotational symmetry. The space group is D_{3d^6} ($R\bar{3}C$). Alternatively a hexagonal unit cell can be defined, which then contains 18 anions and 12 cations [32]. For its spectroscopic features some lower symmetry terms are essential. A detailed discussion of these can be found in the literature [33].

3.1.1 The Guinea Pig

Ruby is well characterised theoretically as well as experimentally. A summary for optical spectroscopy can be found in [33]. A detailed theory about the spectral features of ruby is given by Sugano, Tanabe, and Kamimura [34]. In this thesis ruby was chosen, because it is a well established 'guinea pig' also for ODEPR: We have demonstrated the main ideas of the microwave modulated MCD approach (Section 2.1) with the wavelength dependence of ruby ODEPR elsewhere [26, 3] and we have applied the coherent Raman theory (Section 2.2) to the ODEPR of ruby [6].

With these prerequisites ruby is an ideal candidate for the extension of our technique to 35 GHz and also to pulsed microwave excitation.

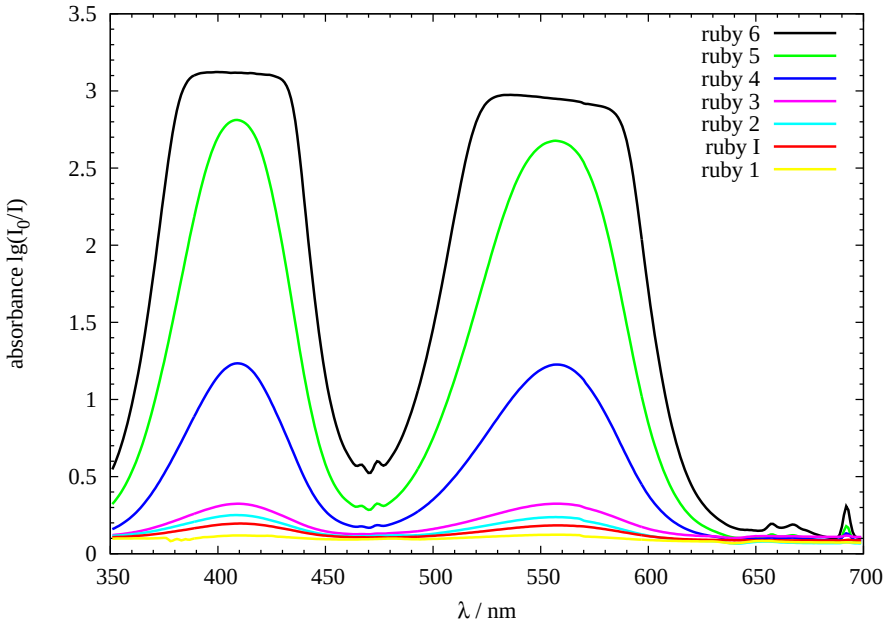

Figure 3.2: Optical absorbance of different ruby samples. The samples are listed in order of decreasing absorbance.

3.1.2 35 GHz ODEPR Sample

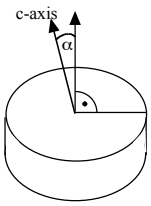

Figure 3.1: The angle α between the c-axis and the surface normal.

A small piece of a not oriented ruby crystal of unknown concentration was found and oriented with Laue measurements by Gisela Pike of our preparation lab. The final orientation of $\alpha = (0.0 \pm 0.2)°$, where α is the angle between the symmetry axis and the surface normal of the sample (Figure 3.1), was determined again with a Laue measurement*.

The sample is referred to as ruby sample 'I'. In order to estimate the concentration of sample I, the optical absorbance for all ruby samples was measured, see Figure 3.2. From this figure we can see that the absorbance of sample I is between those of samples 1 and 2. Since the optical path through

*There is a report about the details of the preparation with the reference number 2023 for the work order to the preparation lab. The accuracy of this measurement is determined by the measurement of the distance between the sample and the photo-paper (±1 mm, Gisela Pike, personal communication).

sample	integral	l	Cr:Al per atom	α
1	33.9	2.2 mm	6×10^{-5}	10°
2	51.1	2.2 mm	2×10^{-4}	7°
3	66.6	2.2 mm	5×10^{-4}	7°
4	183.1	2.2 mm	1.7×10^{-3}	2°
5	408.0	2.2 mm	5×10^{-3}	6°
6	589.7	2.2 mm	9×10^{-3}	unknown
I	45.5	1.1 mm	$(4 \pm 1) \times 10^{-4}$	$(0.0 \pm 0.2)°$

Table 3.1: List of ruby samples. l is the optical path length and α the orientation. The column 'integral' gives the area under the absorption curves from Figure 3.2.

sample I is only 1.1 mm, while all the other samples are 2.2 mm long, the concentration of sample I can be estimated from these measurements to be close to that of sample 3. Table 3.1 shows the integrals of the absorbance, the pathlength l, the concentration c, and the orientational angle α for each sample. The values for the concentration and orientation of samples 1 to 6 were taken from [35], while the integral is the area under the respective curve in Figure 3.2. The pathlength was determined by measuring the sample thickness with a calliper gauge. The orientation for sample I is from the Laue measurement, while its concentration can be estimated from the integral of the absorbance. Assuming validity of the Lambert-Beer law [36, 37], $A = \epsilon c l$, where A is the absorbance, ϵ the molar extinction, c the concentration, and l the optical path length, we can conclude that the integral of the absorption curve divided by c and l should be a constant. For the samples 1 to 6 this constant has a relative error of more than 30%. This gives the accuracy of the nominal concentrations in Table 3.1. Further, we can estimate the concentration of sample I, as given in the table.

3.2 Myoglobin

3.2.1 Introduction

Myoglobin (Mb) is a relatively well understood, yet complicated, test substance. ODEPR of Mb has never been measured and for our particular sample we did neither have MCD nor EPR results at hand. For this thesis Mb was chosen to demonstrate the procedure of sample preparation and preliminary experiments of MCD and EPR, which are clearly needed before

ODEPR can successfully be tried.

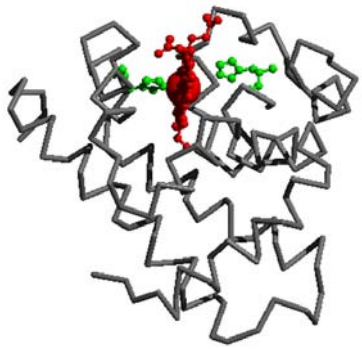

Figure 3.3: Structure of Metmyoglobin from horse heart. The two key histidines are shown in green and the haem in red. The central iron is displayed enlarged.

Since the elucidation of its three-dimensional structure [38] Mb [39] together with the very similar, but more complex haemoglobin [40, 39] has become one of the best understood metalloproteins.

Mb is an oxygen-carrying haemoprotein in the muscles of vertebrates. Its non-polypeptide prosthetic group is protoporphyrin IX, which together with a central iron atom constitutes the heam group (Figure 3.3). The single polypeptide chain has 153 amino acids and a mass of 18 kD (1 Dalton = 1 atomic mass unit). The overall dimensions of Mb are about $45 \times 35 \times 25$ $\mathring{A}^3$. 75 % of its backbone are in an α-helical conformation. The well defined interior of the protein mainly consists of non-polar residues. The only two polar residues inside Mb are the proximal and the distal histidine, which have a critical function at the oxygen binding site.

In its natural surrounding the iron in Mb is in the Fe^{2+} oxidation state, i.e. ferromyoglobin. Without oxygen it is in the high spin form. When it gets oxygenated (not oxidised!) it is low spin oximyoglobin (MbO_2), in which the iron is smaller and fits better into the porphyrin ring.

Depending on the preparation, the sample changes the oxidation state of the central iron from reduced ferromyoglobin, MbO_2, to oxidised ferri- or metmyoglobin, $Mb^+(H_2O)$, where the iron is in the oxidation state Fe^{3+} with the sixth coordination site being occupied by water or hydroxide [41].

The Mb experiments presented in this thesis were done on metmyoglobin from horse heart.

3.2.2 Sample Preparation

Our sample is horse heart Mb (M1882) from Sigma[†]. The preparation of the sample followed a procedure also used by Harriet Seward[‡].

The Mb powder was dissolved in 50 mM Hepes[§] buffer at pH 7. To have a well defined high-spin ferric sample the solution was fully oxidised with

[†]http://www.sigmaaldrich.com

[‡]Harriet Seward, School of Chemical Sciences, UEA Norwich, personal communication.

[§]http://resorg.com/hepes.htm

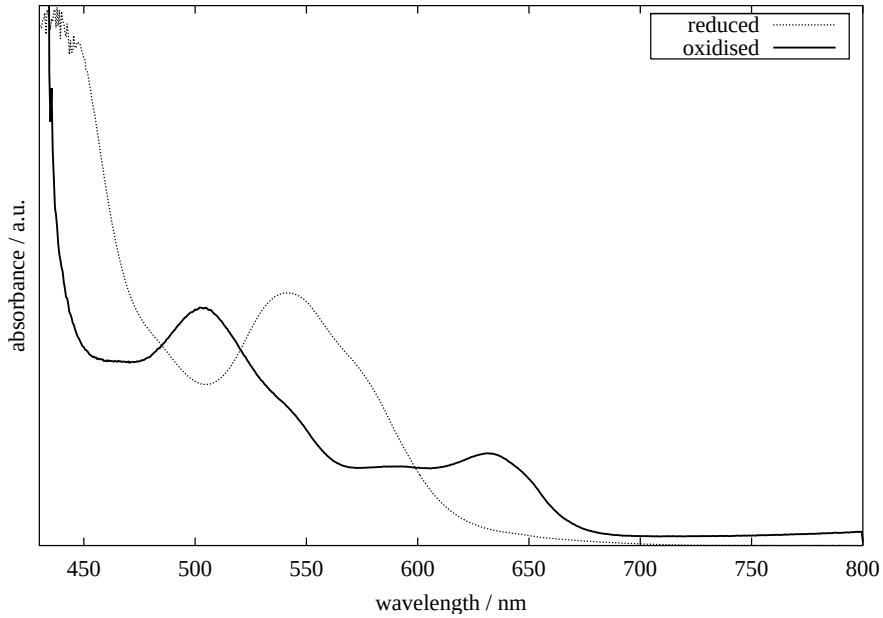

Figure 3.4: Optical absorption spectrum of Mb in its reduced and oxidised form.

name	concentration	remarks
UEA	unknown	Norwich, not properly oxidised
Mb 1	7.7 mM	MPI Dortmund
Mb 2	1.69 mM	MPI
raw	unknown	MPI, without ethanediol, no oxidising agent
Mb I	unknown	prep-lab, Mb:ethanediol = 1:1
Mb II	unknown	prep-lab, 3:1
Mb III	unknown	prep-lab, 30:25 + sucrose
Mb IV	unknown	prep-lab, 5:4 + sucrose
Mb V	31 μM	prep-lab
Mb VI	284 μM	prep-lab, no oxidising agent, but mainly high-spin
Mb 1b	1.22 mM	prep-lab, diluted from sample Mb 1

Table 3.2: Myoglobin samples.

a freshly made stock solution of potassium ferricyanide, $K_3Fe(CN)_6$, in a 1:1 (ferricyanide:Mb) molar ratio. The reaction takes less than half an hour. The oxidation state was checked with the absorption spectrum. The oxidised state can clearly be identified from the absorption peak at 500 nm and the absence of a peak at 540 nm (Figure 3.4). The ferricyanide was removed from the solution by running it down a gel filtration column, PD-10 from Pharmacia. Note that the filtration process will further dilute the sample, because the filter is rinsed with buffer. Since most of our experiments are done at low temperature we added ethanediol, a glassing agent, by a 50:50 volume ratio. We need to make a glass in order to reduce the scattering of light. Finally the concentration of the sample was determined by its well known Soret band extinction coefficient of $\epsilon(410\text{ nm}) = 188\text{ cm}^{-1}\text{mM}^{-1}$ [42].

Since the above recipe did not yield satisfactory glasses, the mixture of buffer and glassing agent was investigated further in collaboration with Gisela Pike from our preparation lab: 11 mixtures of Hepes and ethanediol with variable ratios of 60:40 to 40:60 by volume were prepared in steps of 2%, filled into optical cuvettes of 1 mm thickness, and frozen quickly in liquid nitrogen.

The result was documented by taking photographs under a microscope. Figure 3.5 shows a 50:50 mixture as an example. Since variation of the ratio did not improve the glasses, glucose was systematically added, which allegedly[¶] should improve glassing of metalloprotein samples. This assertion could not be verified.

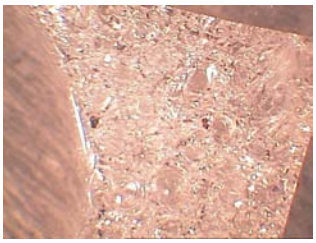

Figure 3.5: Glassing of a 50:50 mixture of Hepes and ethanediol. The sharp edge on the top and right indicates the dimensions of the cuvette (width 1 cm). The rounded edge on the left indicates the surface of the glass towards the open end of the cuvette.

Several samples have been prepared over the years and they are listed in chronological order in Table 3.2. The first sample, 'UEA' was provided by Myles Cheesman from the University of East Anglia (UEA) in Norwich. The samples labelled with arabic numbers are my first attempts in collaboration with the Max Planck Institute (MPI) in Dortmund, while the ones labelled with roman numbers were done either by Gisela Pike or myself in the preparation lab. When concentrations are given they were determined by optical absorption spectroscopy, as explained above.

[¶]Myles Cheesman, School of Chemical Sciences, UEA Norwich.

Chapter 4

Established Methods

Two standard methods, MCD (Section 2.1.2) and EPR (Section 2.1.1), are combined in the ODEPR technique. An understanding of both experiments, MCD and EPR, is therefore essential for improving the new technique.

4.1 Magnetic Circular Dichroism

MCD is used as a fingerprint method in inorganic biochemistry, i.e. it gives a spectrum which is characteristic for a certain surrounding of a metal centre in a metalloprotein. MCD is not only sensitive to the geometry of the site, but also to the kind of ligand.

Here MCD of myoglobin (Mb) is measured. For our Mb samples no MCD was measured before. However, MCD of Mb has been done before [43, 44, 45, 46, 47, 48] and theories to treat high spin haem MCD have been developed [49, 50].

4.1.1 MCD Spectrometer

For the MCD measurements a Jasco J500A spectropolarimeter was purchased. It was modified (see Appendix A.1 for the design drawings) to connect it to an Oxford Spectromag bath cryostat with a superconducting split coil magnet. Further the Xenon lamp and the photomultiplier tube of the J500A were protected from the magnetic field with iron shields, since Jasco recommended to do so.

Without shield, the magnetic field at the position of the photomultiplier was (40 ± 5) mT, with a 1.5 T field at the place of the sample. It was not measured within the shield, since the set-up works fine and the measurement would have been difficult for mechanical reasons.

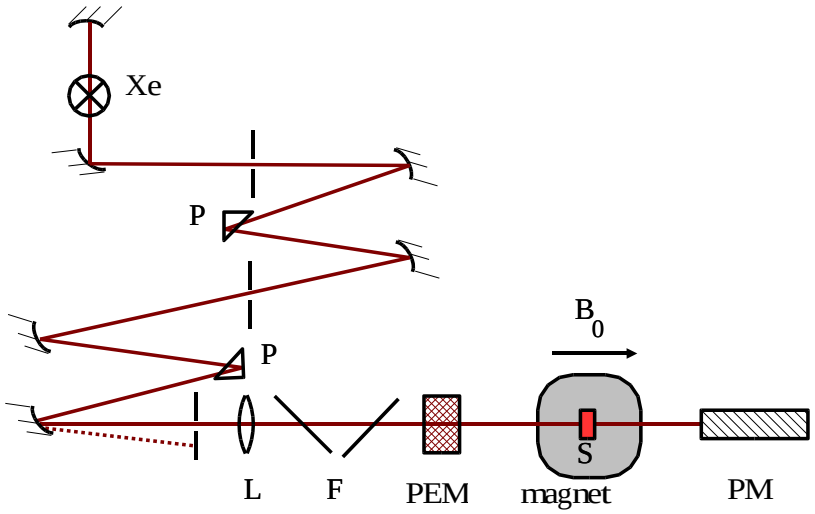

Figure 4.1: Schematic sketch of the optical components of the MCD spectrometer. Xe: Xenon arc lamp; P: prism; L: lens; F: optical filter; PEM: photoelastic modulator; S: sample; B_0 static magnetic field; PM: photomultiplier tube.

The wavelength of the spectrometer can be varied between 180-700 nm with a double prism monochromator. Figure 4.1 shows a schematic overview of the optical set-up. Light is provided by a water cooled Xe arc lamp (450 W). The two prisms differ in their axial design in order to select a linear polarisation, as well as the desired wavelength. With the photoelastic modulator (PEM) the light is modulated between left and right circularly polarised with a frequency of 50 kHz, before it passes through the sample. The light is detected with a photomultiplier tube. A lock-in amplifier which is referenced to the PEM detects the difference in absorbance. Instead of normalising to the photocurrent, the Jasco J500A keeps the current constant with an electronic regulation which adjusts the photomultiplier voltage in order to achieve this.

The optical system can be nitrogen purged, to protect it from reactions with ozone from the lamp. This is especially important in the ultra violet region. The cryostat windows are de-misted with nitrogen from the reservoir of the cryostat. (see drawings in Appendix A.1)

The wavelength calibration of the spectrometer was done by Uwe Damm [51], while the MCD amplitude was calibrated with a 6 ‰ aqueous solution of camphor-sulfonic acid ammonium salt ($C_{10}H_{16}O_4S$) from Sigma (Product

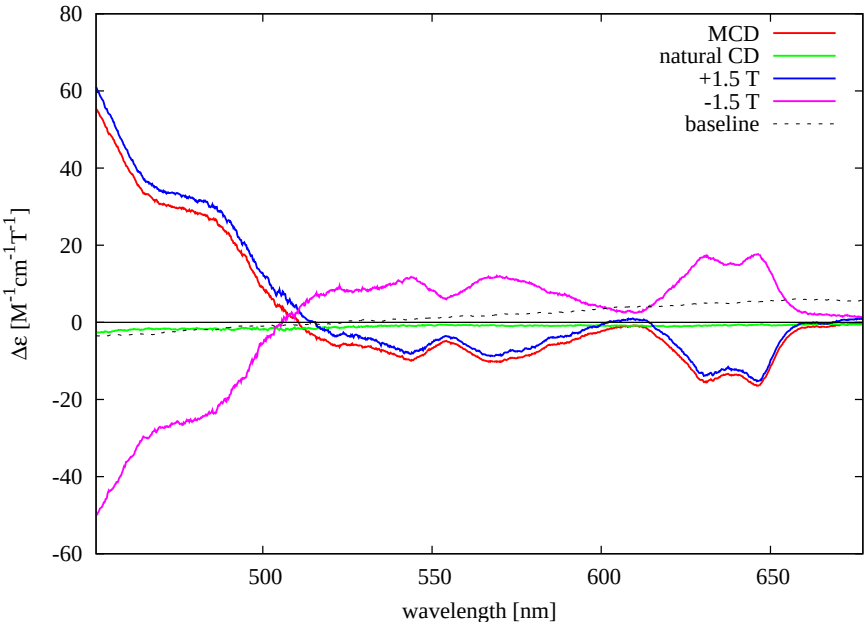

Figure 4.2: MCD of Mb 2, concentration $c = 1.69$ mM, temperature about 6 K.

number 18,836; molecular weight 249.33). The 290.5 nm peak was taken to have a difference in extinction between left and right circularly polarised light of $\Delta\epsilon = \Delta A/(c \cdot l) = 2.4\ \mathrm{cm}^{-1}\mathrm{M}^{-1}$ in agreement with the technical reports 43 and 44 of the European Chirality Services*. c is the concentration and $l = 1$ mm the optical path through the sample. This value for $\Delta\epsilon$ differs slightly from older calibrations by other groups (e.g. $2.2\ \mathrm{cm}^{-1}\mathrm{M}^{-1}$ in [46]).

4.1.2 MCD Spectra

MCD was measured for two Mb samples, labelled '2' and 'V' respectively (see Table 3.2 for a list of samples).

Figure 4.2 shows spectra in the visible wavelength range at 6 K at a magnetic field of ±1.5 T. The trace labelled 'MCD' is the difference of the ±1.5 T scans divided by 2, while the trace 'natural CD' (circular dichroism) is the sum of these spectra divided by 2. The baseline was measured from a 50:50 mixture of Hepes and ethanediol at +1.5 T, but at a temperature of 4.2 K.

In principle a baseline measurement should not be necessary, since all

*http://digilander.libero.it/ecssrl

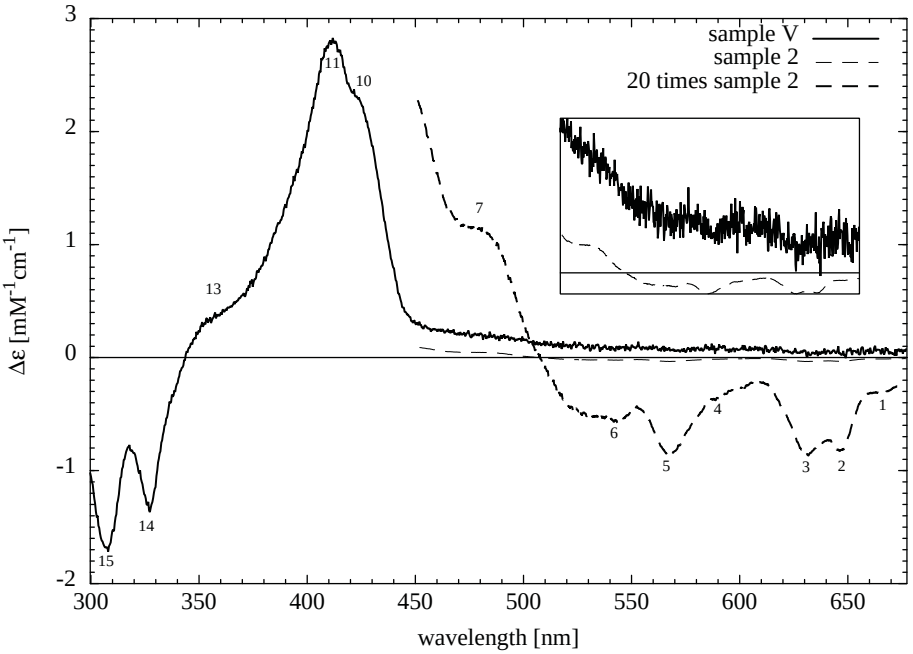

Figure 4.3: MCD overview, temperature 4.2 K, magnetic field 1.5 T

effects independent of the magnetic field should cancel when subtracting the spectra for positive and negative field direction. Moreover it is very unclear, whether such a baseline measurement properly represents the effects of the solvent and glassing agent within the sample, since it is cooled down separately and might glass in a different way. The baseline is presented only for completeness and not used for the following data. Instead a measurement with sample but without magnetic field can be used for baseline correction, if the opposite field direction was not measured.

During most of the measurements on sample 2 it was unclear whether an inversion of the field is advisable and technically possible with the magnet and controller used. As soon as Oxford Instruments agreed that we can invert the field, this was done for all spectra. As a consequence, all following spectra on sample 2 were taken only with positive field direction, while all spectra on sample V represent the difference between spectra of positive and negative field direction.

Figure 4.3 shows an overview over the complete spectral region under investigation. The spectra were taken in liquid helium with normal pressure, i.e. a temperature of 4.2 K. The data from sample 2 are shown in normal scale and a second time enlarged by a factor of 20. The inset shows the

number	λ_M Myles [nm]	λ_J Figure 4.3 [nm]	feature
1	—	670	tiny trough
2	642	648	trough
3	632	631	trough
4	592	590	tiny trough
5	562	567	trough
6	548	544	tiny trough
7	479	478	shoulder
8	446	—	peak
9	423	—	trough
10	—	424	shoulder
11	410	412	peak
12	368	—	trough
13	—	359	shoulder
14	324	328	trough
15	—	307	trough

Table 4.1: Peaks, troughs, and shoulders in the MCD of Mb, summarising the features from Figure 4.3 and comparing to Myles Cheesman's data (Figure C.1).

region between 460 nm and 677 nm, to compare the two samples.

From the inset we can clearly see, that in the overlapping region the two samples show qualitatively the same features in the MCD. There is a significant offset of unclear origin between the two measurements. Data of sample 2, 1.69 mM, were used to investigate the visible region and sample V, 31 μM, for the ultraviolet, so called Soret, band.

As a first check of the spectral features of the MCD of our Mb from horse heart at pH 7 we compare the data to a 4.2 K MCD spectrum of Mb from horse skeletal muscle at pH 5.5, provided by Myles Cheesman (see Appendix C), bearing in mind that the origin of the sample, the preparation, the magnetic field, and the pH are different. Table 4.1 shows the wavelengths of the main features in the spectra. The visible region down to 460 nm shows mainly the same features with slight shifts in wavelength. The amplitude of the data of Figure 4.3 compared to Myles Cheesman's data differs. The magnetic field for Myles' data is unknown, but probably between 1 and 5 T, so that the absolute scale cannot be compared. However, this cannot explain the obvious difference in baseline and changes in sign. Feature number 3, for

instance, shows a $\Delta\epsilon$ of -13 $M^{-1}\text{cm}^{-1}$ and -43 $M^{-1}\text{cm}^{-1}$ for the two data sets, while feature 4 gives +1 $M^{-1}\text{cm}^{-1}$ and -20 $M^{-1}\text{cm}^{-1}$ respectively.

In contrast to the visible region, the Soret band clearly differs from the data provided by Myles Cheesman. Features 8, 9, and 12 are not seen, instead there are shoulders (features 10 and 13) which might indicate, that another chromophore with strong MCD is overlapping the actual Mb MCD. A possible explanation would be, that the oxidising agent $K_3Fe(CN)_6$ was not fully removed with the gel filtration column.

For this reason the MCD of ferricyanide was measured, to rule out that unclear features in the spectrum originate from it. Ferricyanide has a rather strong MCD in the Soret band region which looks qualitatively similar to the features found, when we compare sample V to a linear combination of MCD of Mb without ferricyanide and MCD of ferricyanide. Besides we found by MCD of the filtrate that small amounts of $K_3Fe(CN)_6$ of the order of tens of μM pass the gel filtration column PD 10.

However, the features common between Figure 4.3 and the data provided by Myles Cheesman clearly indicate, that we measure the MCD of Mb.

Visible bands

Sample 2 was used for measurements in the visible region. Spectra for different magnetic fields at a temperature of 4.2 K are displayed in Figure 4.4. A baseline correction was not made and the field was not inverted for these measurements, so the 0 Tesla spectrum shows basically the natural CD of the sample and the set-up. Features 1 to 6 from table 4.1 can be identified in Figure 4.4. The amplitudes of these 6 features are shown in Figure 4.5 for the data from Figure 4.4 and some additional spectra. The amplitudes in Figure 4.5 were baseline corrected by the 0 T data. All MCD amplitudes show a linear dependence on magnetic field, as expected. The slopes of the linear regressions are given in the figure.

Figure 4.6 shows MCD spectra of Mb 2 at different temperatures. The most striking temperature effect is the inversion of features 1, 5, and 6 above 10 K.

An attempt to analyse the temperature dependence is shown in Figure 4.7. The MCD amplitudes of the spectra of Figure 4.6 are plotted against reciprocal temperature for the features identified earlier. Especially feature 7 shows a linear dependence in 1/T without offset, which is a strong indication of dominating C-term MCD. Also the other features show nearly linear 1/T dependence, but the origin of their offsets is unclear.

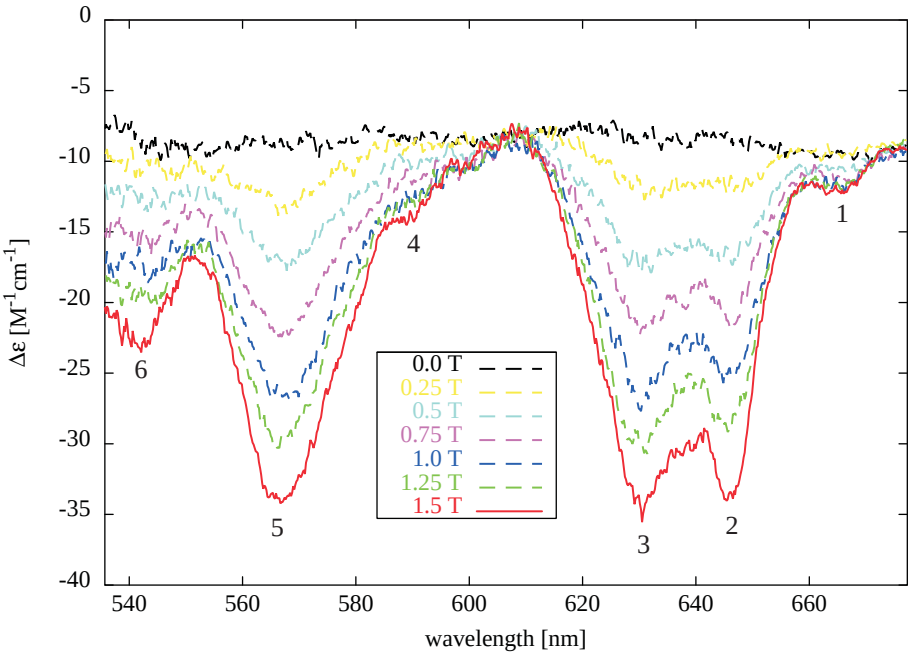

Figure 4.4: MCD spectra of sample Mb 2 for different magnetic fields, temperature 4.2 K. The numbers refer to those in Table 4.1.

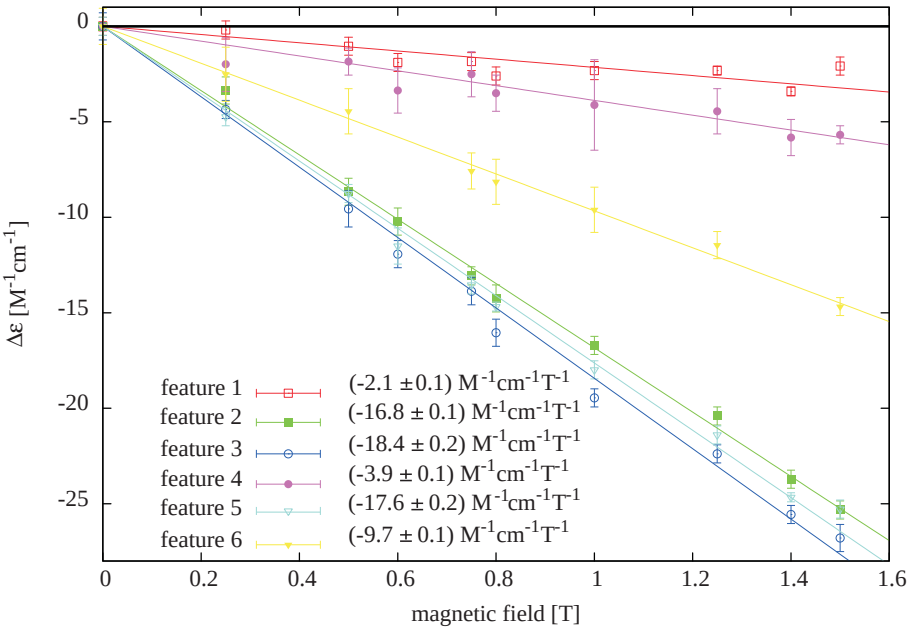

Figure 4.5: MCD amplitudes versus magnetic field show a linear relationship.

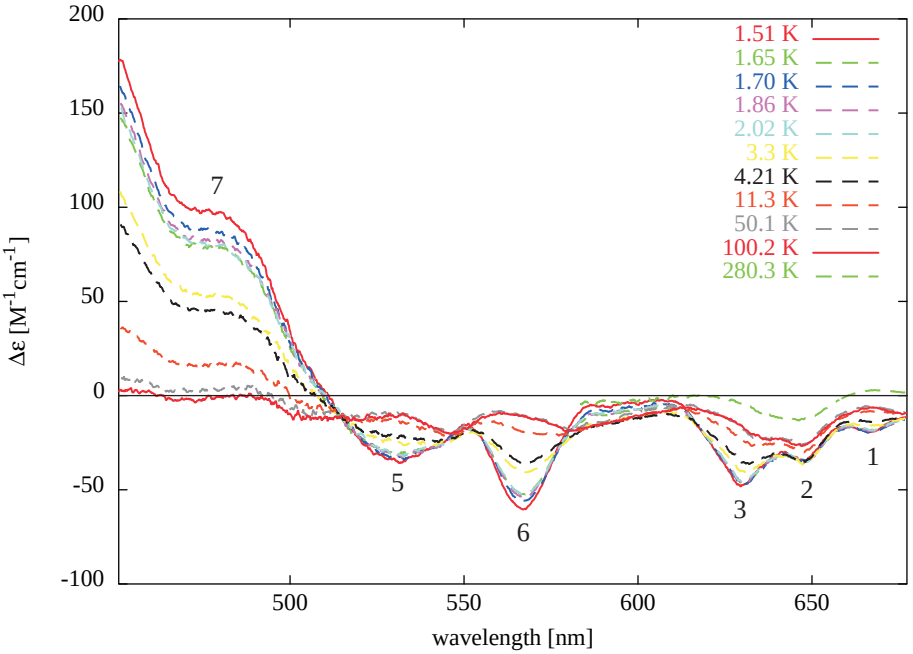

Figure 4.6: MCD spectra for different temperatures. Magnetic field 1.5 T.

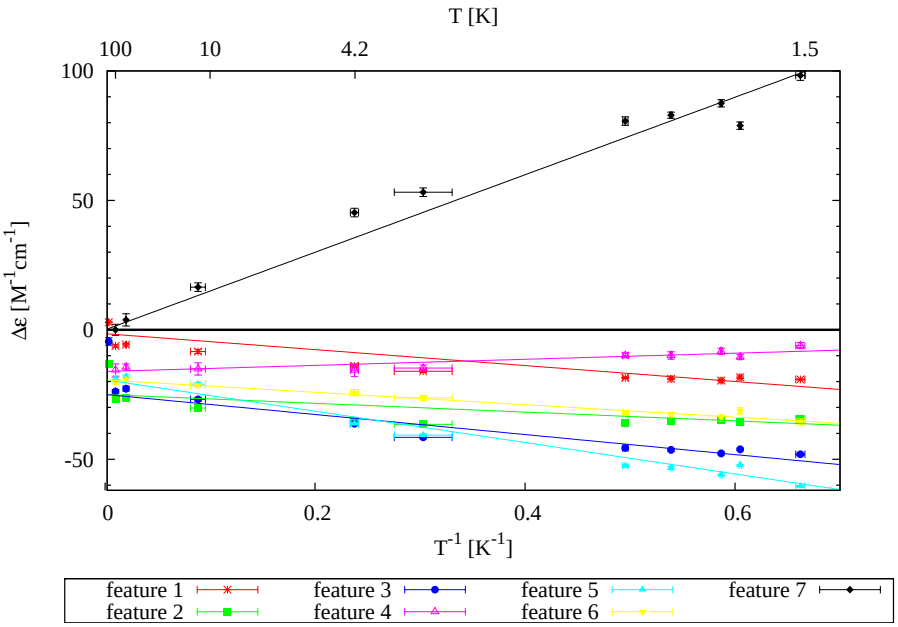

Figure 4.7: MCD amplitudes versus temperature.

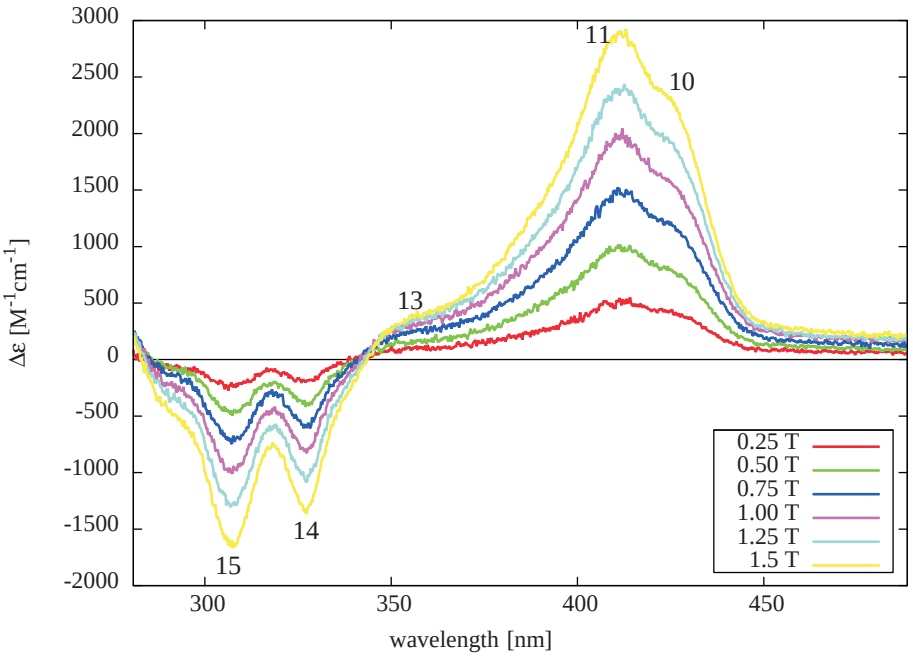

Figure 4.8: Soret band MCD spectra of sample V for different magnetic fields, temperature 4.2 K.

Soret band

For the measurements in the UV sample V was used.

Figure 4.8 shows spectra for different magnetic fields. The magnetic field dependence is linear for all features in the spectrum (master-plot not shown). This indicates that even at low temperature we are still in the Curie regime when the fields are not higher than 1.5 T.

Soret band MCD spectra of sample V for different temperatures are shown in Figure 4.9. Features (see Table 4.1 and Figure 4.3 for numbering of features) 14 and 15 show a linear dependence on reciprocal temperature, while features 10 and 11 have an additional part not varying so strongly with temperature. This can clearly be seen from the low temperature data in Figure 4.10. This figure is an attempt to create a master-plot for C-term MCD by scaling the MCD amplitude with T/B. The MCD of features 14 and 15 is constant in this representation, i.e. linear in reciprocal temperature, while features 10 and 11 increase. Possible reasons for this can be MCD A and B terms in this spectral region. When going to higher temperatures, also features 14 and 15 are not dominated by the C-term any longer. There is some other effect, which leads to a bigger positive value of $\Delta\epsilon T B_0^{-1}$ for increasing

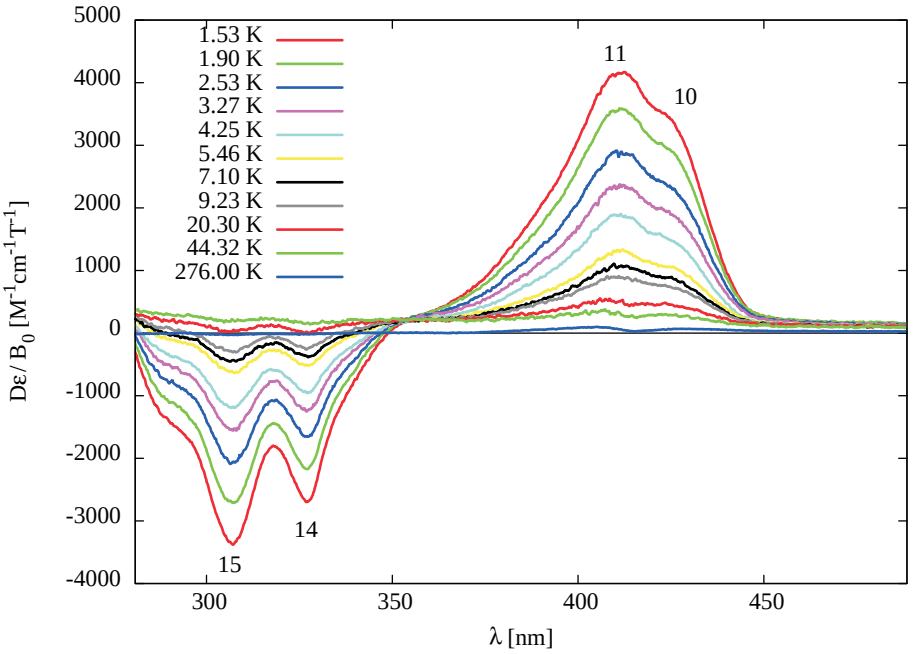

Figure 4.9: Soret band MCD spectra for different temperatures between 1.5 K and 276 K. Magnetic field 1.5 T.

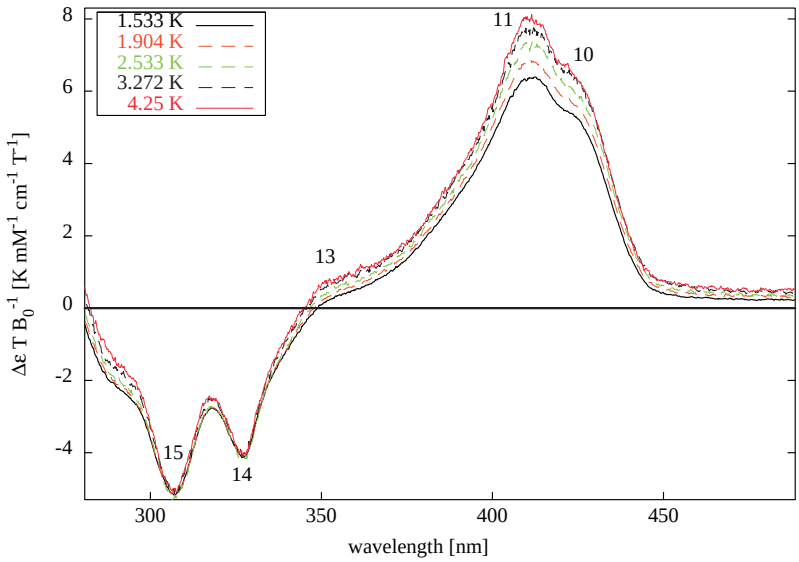

Figure 4.10: Soret band MCD of sample V at low temperature. The MCD amplitudes are multiplied by the respective temperature and devided by the magnetic field to give a masterplot for C-term MCD.

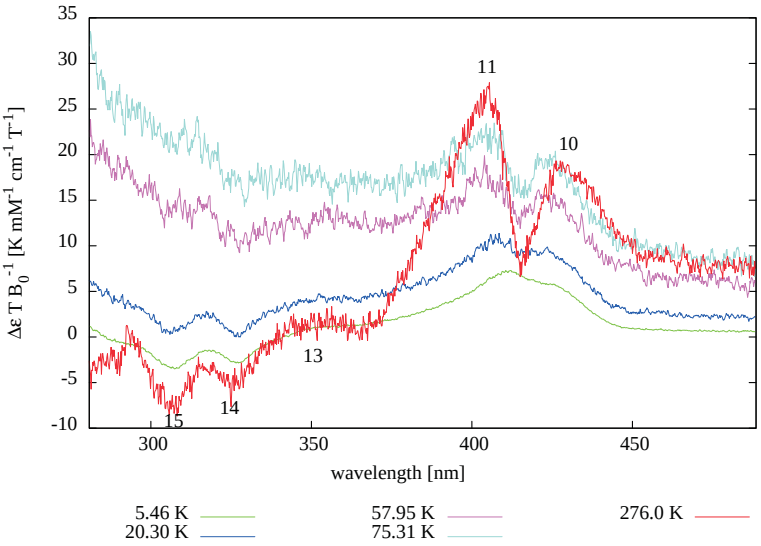

Figure 4.11: Soret band MCD of sample V at higher temperature. The MCD amplitudes are multiplied by the respective temperature.

T, even in regions of negative MCD.

Figure 4.11 shows this effect. The overlap of the 276 K spectrum and the 5.5 K spectrum in the low wavelength region might indicate, that the effect is related to the fact that the sample is a glass. When it is heated to 276 K it becomes liquid and features 14 and 15 go back to their regular C-term behaviour. The other features are not purely C-term anyway, therefore an overlap is not expected around 400 nm.

Assignment of Transitions to the Spectra

Results from others who did MCD on Mb can be found in the literature [43, 44, 45, 46, 47, 48].

Bolard and Garnier [48] measured absorption, CD, and MCD of ferri- and ferro-myoglobin derivatives from sperm whale. They found a splitting of the so called Q_0 and Q_1 absorption bands with CD. Their analysis of A-, B-, and C-terms in the MCD remains tentative and they only consider transitions which are supposed to arise from low spin haem. They tabulate their findings from a Gaussian analysis of CD about the energies of the Q_0 and Q_1 transitions, but they explicitly exclude our derivative MetMbH_2O, because its CD is too flat for a proper analysis. With their assignments they follow Stephens *et al.* [52]. Bolard and Garnier measured at 25° C and when doing MCD they had a fixed magnetic field of 0.32 T opposite to the direction

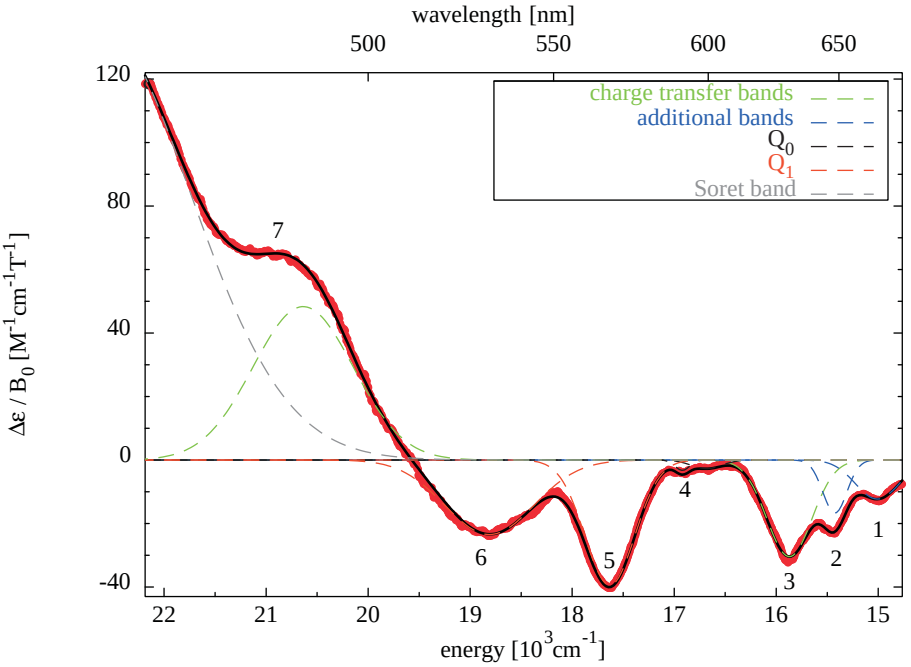

Figure 4.12: MCD of Mb 2 at 1.5 K and 1.5 T. Red line: measured MCD spectrum; black line: sum of the fitted Gaussian lines.

of propagation of the light (this is opposite to the convention in [21], which we follow here).

They found charge transfer transitions to the porphyrin Π^* orbitals around 16 $\cdot 10^3$ cm^{-1} and 20 $\cdot 10^3$ cm^{-1}, which is supposed to be due to high spin haem. Further they give the approximate position of the Soret band as 25 $\cdot 10^3$ cm^{-1} and the Q-bands as $Q_0 = 17 \cdot 10^3$ cm^{-1} and $Q_1 = 18.5 \cdot 10^3$ cm^{-1}. They also found splittings of both Q-bands into two Gaussians respectively.

Assuming that no A-term dominates anywhere in the spectrum at low temperature, we can model the spectrum with Gaussian absorption curves. We find the above mentioned bands plus two more in the high wavelength end of the spectrum, see Figure 4.12.

From these Gaussian lines we can conclude, that our features 3 and 7 are the charge transfer transitions to the porphyrin Π^* orbitals. Feature 4 and a small trough next to it, which was not identified in Figure 4.3, constitute the two Q_0 bands, while features 5 and 6 clearly are the two Q_1 bands. Features 1 and 2 are new and remain unassigned. Possibly they are due to a splitting of the charge transfer band at very low temperature.

Vickery *et al.* [46] found a derivative shape of the Soret band at 413 nm

($24.2 \cdot 10^3$ cm^{-1}) at a temperature of 22° C, which can also be seen in our data at 276 K, red line in Figure 4.11. Even though a derivative shape is usually indicative of A term MCD, Vickery *et al.* claim that in the case of the Soret band of Mb it is due to two C-terms of opposite sign and shifted in energy. About their low temperature data Vickery *et al.* write: 'Low temperature MCD spectra to -147° were recorded [...], but these did not clarify the spectra. Some increase in intensity, but little change in shape of all bands was observed.' This view is only partially supported by the measurements presented here. At very low temperature, the derivative shape is nearly gone compared to the absorptive features in the spectrum. It can only be seen as a shoulder in our data, feature 10 in Figure 4.3 and Figure 4.10. Especially Figure 4.10 indicates, that this feature is not solely C-term. Unfortunately Vickery *et al.* do not present their low temperature data. However, also in Myles Cheesman's data (Appendix C) the derivative shape around 400 nm is the strongest feature in the Soret band spectrum, while our low temperature data show very broad features, mainly linear in 1/T, overlapping this one. This strongly indicates, that the broad features in our spectrum have a different origin than Mb MCD.

In the ultraviolet region we can therefore only assign feature 10, which becomes a derivative shape at high temperature, as the Soret band of Mb.

Conclusion

With the modified CD spectrometer it is now possible to measure variable temperature MCD in our lab. This has been demonstrated on Mb.

The dependence on temperature T and magnetic field B_0 is to a good approximation B_0/T, indicating, that up to 1.5 T and down to 1.5 K we are still in the linear, so called Curie, region of MCD.

The spectra in the visible reveal the same features as found by Bolard and Garnier [48] before, plus two additional bands (features 1 and 2, Table 4.1). One of these bands (feature 2) can also be identified in a spectrum provided by Myles Cheesman (Appendix C).

The ultraviolet region of the spectrum seems to be obscured by strong features, which cannot be found in spectra measured by other groups. This is attributed to an experimental error, rather than new physics of Mb. The most likely explanation is that some of the oxidising agent sneeked through the filter column during preparation.

The analysis of the Gaussian bands presented here is tentative and could be continued, analysing all bands over the whole range of measured temperatures. However, further analysis of Mb MCD is beyond the scope of this thesis.

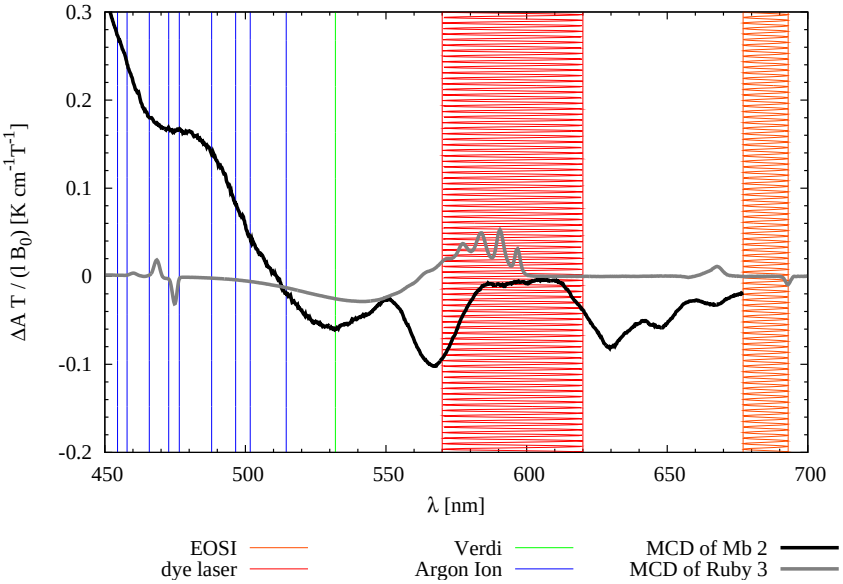

Figure 4.13: MCD of ruby and myoglobin are shown together with the available light sources for the ODEPR experiment (Ruby data were recorded by Birgit Börger in Norwich, UK).

The MCD of a new metalloprotein sample like Mb can be used as an indicator for its ODEPR. Figure 4.13 shows the MCD of Mb 2 and ruby 3, scaled with optical path length l, temperature T, and magnetic field B_0. The main light sources for our ODEPR experiments are indicated in the figure. In such a representation, we can compare the MCD intensity of different materials and, at the same time, see at which wavelength an ODEPR measurement is technically possible.

4.2 Electron Paramagnetic Resonance

In order to facilitate the ODEPR experiments not only MCD but also EPR can now be measured within the same cryostat. Conventional EPR is actually measured with the same microwave set-up as ODEPR. For these measurements the 14 GHz spectrometer, described in Section 5.1, is used with the additional field modulation for EPR. This feature allows us to check EPR parameters like resonance field and g-values under the same conditions as for ODEPR. It should however be kept in mind, that the spectrometer is not optimized for conventional EPR, since the optical cavity has thick copper

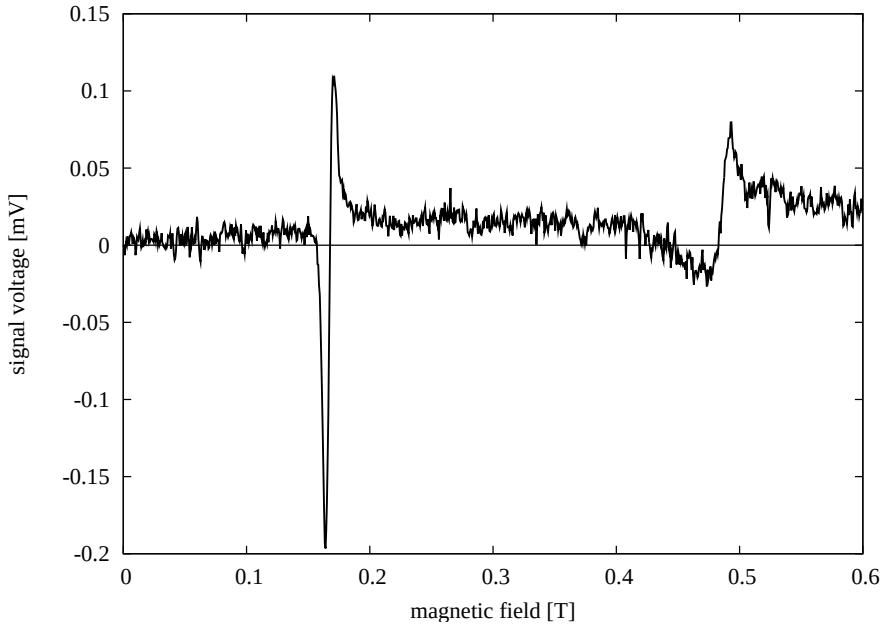

Figure 4.14: EPR of 7 μl of Mb 1 at 1.59 K, 13.97 GHz, 340 mW.

walls in order to increase the Q-factor, which reduce the efficiency of the field modulation.

Even though the spectrometer can in principle measure absorption and dispersion, the dispersion phase signal is usually not used since it can sometimes be distorted by the AFC-system (automatic frequency control, Section 5.3), which is locked to the sample cavity, like in other absorption type EPR spectrometers [53]. The absorption phase in its derivative shape will usually be taken as the EPR signal.

Figure 4.14 shows the derivative of the EPR absorption of 7 μl of Mb 1 (Table 3.2). This volume of the 7.7 mM sample corresponds to 3×10^{16} spins. The spectrum was recorded with 340 mW of power, at a temperature of 1.59 K, where two resonances can clearly be identified. The modulation frequency of the magnetic field was 6.5 kHz, the current in the modulation coils was 0.26 A.

In Figure 4.15 at a temperature of 20 K, with a microwave power of about 330 mW, and a sample volume of 21 μl, we mainly see the low field resonance. It represents the g-value in the haem plane. It is $g_\perp = 6.08 \pm 0.02$, where the error is a rough estimate from 2 different scans.

The high field resonance which was seen in the low temperature spectrum in Figure 4.14 can hardly be seen in the 20 K spectrum in Figure 4.15. The

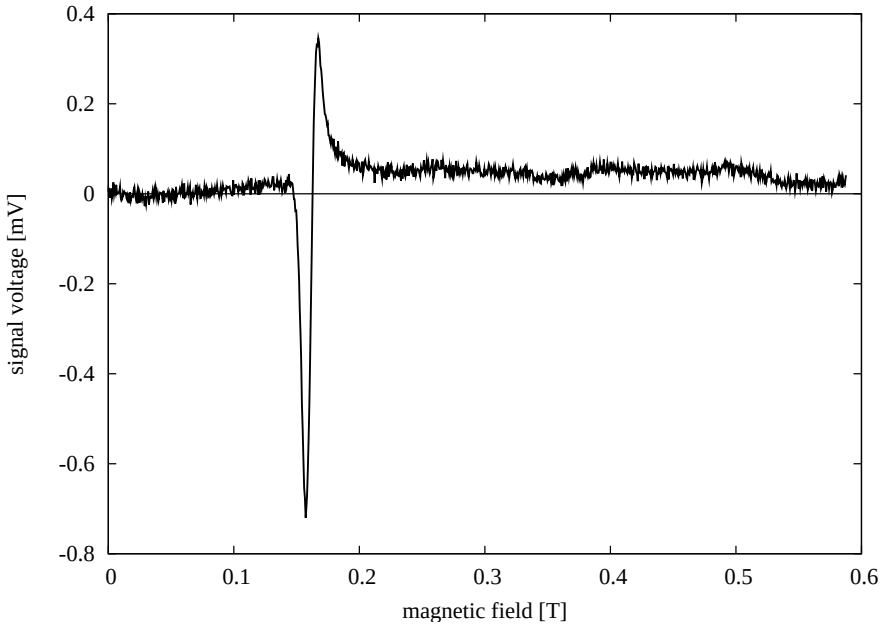

Figure 4.15: EPR of 21 μl Mb 1 at 20 K, 13.90 GHz, 330 mW.

high field resonance is known to saturate much easier with power than the low field resonance [54]. It therefore vanishes with temperature as the population differences become smaller.

Power dependent measurements of the peak to peak EPR derivative of the low field resonance at 9 K and 1.5 K as well as temperature dependent measurements were performed, but did not yield any new information.

Mb derivatives have been studied extensively with EPR before and a review was published as early as 1983 [55]. In these studies high-spin derivatives of metmyoglobins in water showed g-values of $g_{||} = 2.0$ and $g_{\perp} = 6.0$, which is confirmed with the above results from our sample. A very small rhombic distortion to the otherwise axial symmetry is mentioned in the literature, but this could only be measured by crystal studies. The axial coefficient is given as $D = 8.8$ cm^{-1} and the rhombic coefficient $E = 0.2$ cm^{-1}, giving a rhombicity of $\frac{E}{D} = 0.02$.

Chapter 5

Continuous wave ODEPR

This chapter describes the actual ODEPR spectrometer implementations and experiments.

The experimental set-up (Figures 5.1, 5.2) required for ODEPR experiments is based on a conventional EPR spectrometer, augmented by a laser and some optical components for controlling the laser beam. The incident light is usually modulated between left and right circularly polarised with a photoelastic modulator.

ODEPR is a transverse experiment, i.e. the direction of propagation of light $\boldsymbol{k}$, which is parallel to the microwave magnetic field $\boldsymbol{B_1}$, is perpendicular to the quasi static magnetic field vector $\boldsymbol{B_0}$.

In the experiment the magnetic flux density B_0 is slowly swept over the resonance while the sample is irradiated with microwaves and laser light. The light after the sample carries the ODEPR signal, which is extracted in the heterodyne receiver.

Finally the signal is displayed vs. magnetic field, measured with a Hall probe.

5.1 14 GHz ODEPR Spectrometer

The 14 GHz ODEPR Spectrometer is similar to a prototype ODEPR spectrometer used in our lab earlier [16, 56]. The main differences are the new possibility to measure dispersion and absorption phase at the same time and the field modulation, which allows detection of conventional EPR now.

The 14 GHz set-up is displayed in Figure 5.1 and Table 5.1 shows a part list of the components; numbers identify the components in the figure.

Light for the coherent optical excitation is provided by a laser ((1) in Figure 5.1). After the polariser (2) and the PEM (3) the light passes through

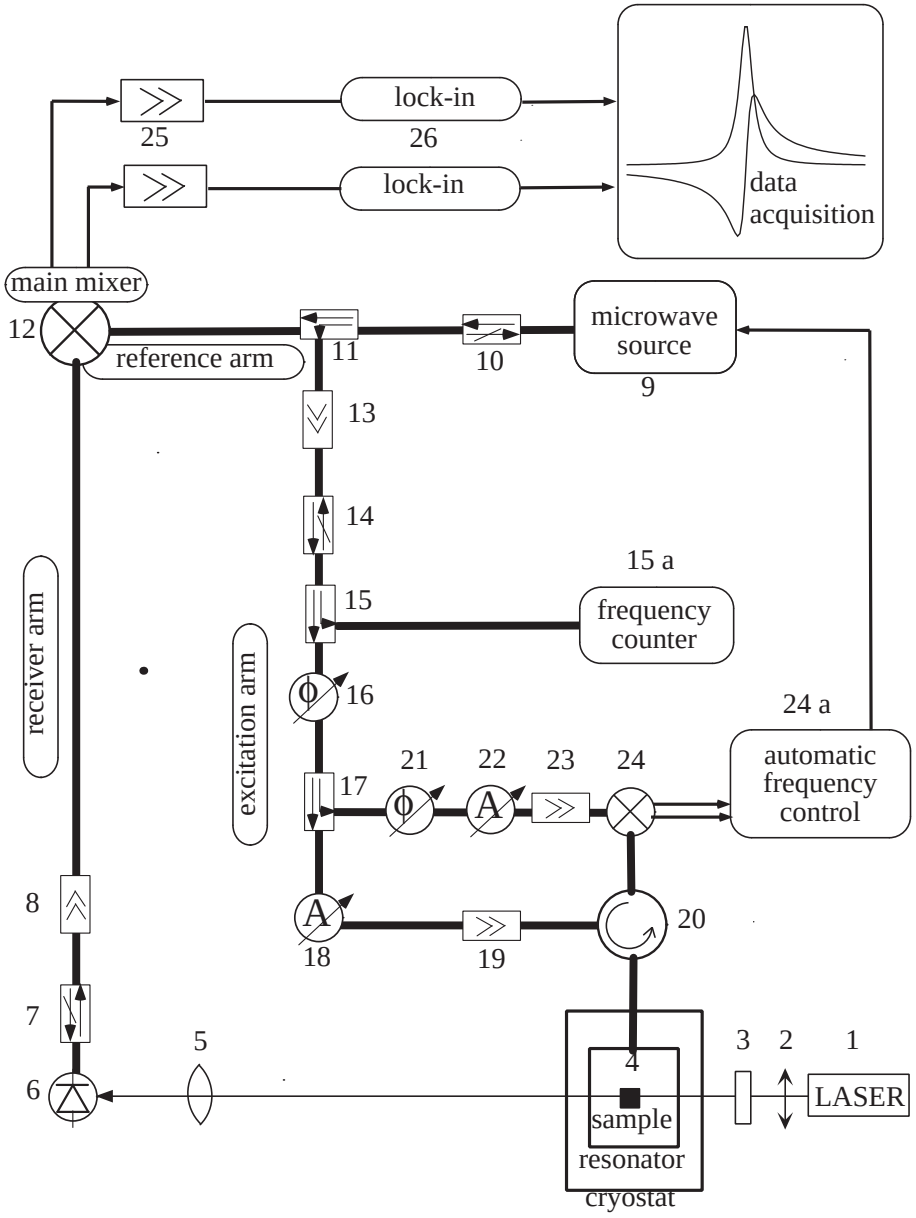

Figure 5.1: Experimental setup. The microwave frequency part is indicated with thick black lines. A part-list can be found in Table 5.1.

number	spectrometer part
1	laser
2	polariser
3	photoelastic modulator: frequency 50 kHz
4	sample: ruby or frozen aqueous solution of the metalloprotein cuvette: quartz glass cylinder, length: 0.5 mm, diameter: 3mm resonator: TE_{102} mode rectangular cavity, optical access along B_1 magnet: super-conductive split-coil, 0 to 3 T cryostat: helium bath cryostat, 1.5 to 300 K
5	optics, i.e. mirrors and lenses
6	fast photodiode: 21 GHz bandwidth
7	isolator
8	low noise amplifier: 1.25 dB max. noise figure, 30 dB gain
9	solid state oscillator:13.4 to 14.1 GHz, 10 dBm
10	isolator
11	directional coupler:10 dB
12	quadrature mixer: typical conversion loss 11 dB
13	amplifier:12 dB
14	isolator
15	directional coupler: 10 dB
15 a	frequency counter
16	phase shifter: manually adjustable
17	directional coupler: 10 dB
18	attenuator: 0 to 50 dB adjustable
19	amplifier: 30 dB
20	circulator
21	phase shifter: manually adjustable
22	attenuator: to adjust local oscillator power of mixer 24
23	amplifier: 20 dB
24	quadrature mixer
24 a	automatic frequency control, see Section 5.3
25	two-channel amplifier: 60 dB, 1 kHz - 1 MHz
26	two lock-in amplifiers

Table 5.1: Part list of the 14 GHz spectrometer. The numbers correspond to those in Figure 5.1.

the sample (4). The sample is mounted inside a rectangular TE_{102} mode microwave cavity [26]. The modulated light signal (or local oscillator and Raman side-band) is detected with a fast photodiode (6) which is connected to the microwave receiver set-up.

The microwaves from a solid state oscillator (9) are split (coupler 11) into an excitation arm and a reference arm, which is the local oscillator of a quadrature microwave mixer (12, main mixer). This mixer down converts the ODEPR signal from the fast photodiode (6). The excitation arm includes a phase shifter (16) to select the amount of dispersion and absorption on the two quadrature detection channels and an attenuator (18) to adjust the amplitude of the excitation field. Some microwave power is coupled (15) out from the excitation arm to measure the microwave frequency. A frequency lock system (21-24a, see also Section 5.3) keeps the microwave frequency locked to the cavity resonance.

Since the sample is cooled to liquid helium temperature, heat losses must be minimised. We therefore replaced a section of the usual microwave guide by a stainless steel waveguide, which has significantly lower thermal conductivity. This waveguide section is gold plated for good electrical conductivity.

The 50 kHz modulation from the PEM is down converted in two separate lock-in amplifiers (25) and the ODEPR signal recorded by a computer, which controls also the magnetic field sweep.

Conventional EPR can be measured on the output of mixer 24 with an additional pre-amplifier and a lock-in amplifier referenced to the frequency of an additional magnetic field modulation.

5.2 35 GHz ODEPR Spectrometer

As with all magnetic resonance techniques, we can also improve the spectral resolution of ODEPR by increasing the microwave frequency. In conventional EPR it is common, to measure at several frequencies. This is especially favourable, when the Hamiltonian contains field-dependent as well as field-independent parts [20]. Moreover, at higher frequency the spin lattice relaxation time T_1 is expected to be shorter and saturation of the EPR transitions less likely. This is, however, not always confirmed experimentally [57].

The obvious technical limit in our case is the availability of a high speed photodetector. The price of microwave components, which seems to grow with frequency, is another important factor. In the attempt to go to higher frequencies, the availability of some 35 GHz components and the technical limits led to the decision to try to build a spectrometer for 35 GHz ODEPR.

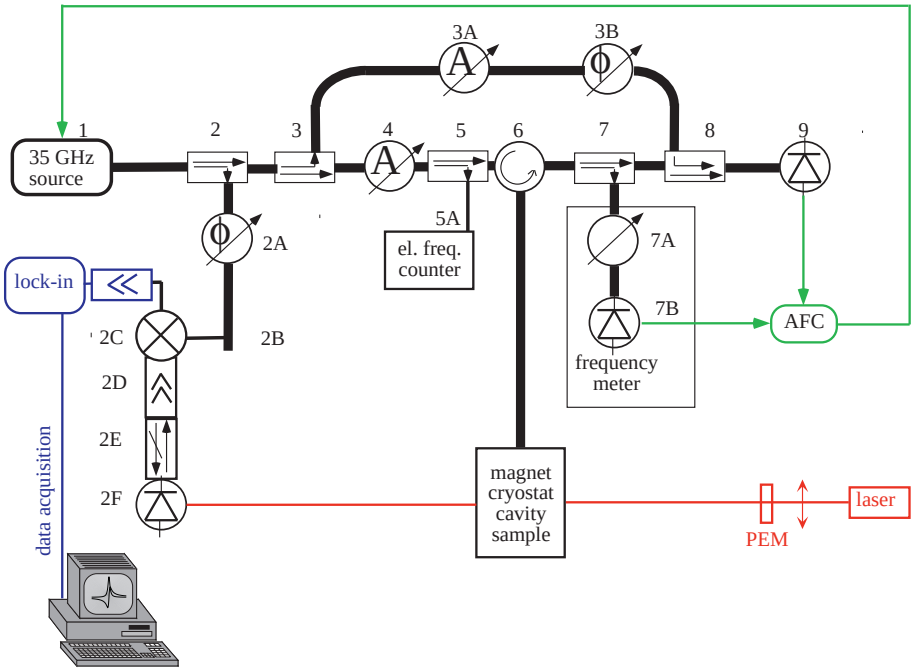

Figure 5.2: Overview of the 35 GHz spectrometer.

5.2.1 Spectrometer Overview

The general concept for the 35 GHz spectrometer is similar to that at 14 GHz. However, the higher frequency calls for wave-guides as the main microwave lines, rather than semi-rigid coax cables. This spectrometer has only a single phase mixer and the automatic frequency control (AFC) detection uses detector diodes, which yield a voltage proportional to the microwave power. These differences are basically due to the higher prices for the high frequency components.

Figure 5.2 shows the set-up of the 35 GHz ODEPR spectrometer. The microwave parts are numbered in the figure, for identification. A list of the microwave parts can be found in Table 5.2.

Microwave radiation is emitted from the solid state oscillator 1. It reaches the microwave cavity via the excitation arm, i.e. directional couplers 2 and 3, attenuator 4, coupler 5, and circulator 6.

Microwaves reflected from the cavity return to circulator 6 and proceed via the directional couplers 7 and 8 to the detection diode 9. Via the reference arm, i.e. coupler 3, attenuator 3A and phase shifter 3B, the signal can be combined with a coherent reference in the 3 dB coupler 8, before the detection. This will allow the detection of EPR derivative absorption as

main arm	side arm	microwave component
1		microwave source, tunable 34.5-35.6 GHz, 22 dBm
2		directional coupler, 10 dB, to optical receiver
	2A	phase shifter
	2B	WR 28 waveguide to K-connector adapter
	2C	microwave mixer
	2D	low noise amplifier
	2E	isolator
	2F	fast photodiode
3		directional coupler 3 dB, to reference arm
	3A	variable attenuator
	3B	variable phase shifter
4		attenuator
5		directional coupler, 10 dB, to counter
	5A	electronic frequency counter
6		circulator
7		directional coupler, 20 dB, to AFC detection
	7A	tunable (frequency calibrated) cavity
	7B	detector diode
8		directional coupler, 3 dB, from reference arm
9		detector diode

Table 5.2: Microwave part list of the 35 GHz Spectrometer.

well as dispersion signals on diode 9, when additionally the magnetic field is modulated.

For AFC (Section 5.3) there is an additional detection arm: coupler 7, tunable cavity 7A, and detection diode 7B. The tunable cavity 7A has a calibrated frequency scale. Therefore this detection arm can in principle be used for frequency determination. However, the more comfortable method is to measure the frequency with the electronic frequency counter 5A connected via a waveguide to coax adapter and a flexible coax cable to coupler 5. The main use of the older tunable cavity frequency meter is, that it can be used to calibrate the scan width of the AFC system.

Optical excitation (red in Figure 5.2) is provided by a laser, a linear polariser and a photoelastic modulator (PEM). The optical signal is detected on photodiode 2F of the optical detection arm of the microwave set-up. This arm includes coupler 2, phase shifter 2A, waveguide to coax adapter 2B, mixer 2C, low noise amplifier 2D, isolator 2E and fast photodiode 2F. After detection with the fast photodiode the signal is amplified and then down converted phase sensitively in mixer 2C. As with the 14 GHz spectrometer, the resulting 50 kHz signal is amplified and further down converted with a lock-in amplifier.

5.2.2 Microwave Cavity

The microwave resonator is one of the critical components in an ODEPR spectrometer. Its main function is to provide a high microwave magnetic field $\boldsymbol{B_1}$ (per input microwave power) parallel to the direction of propagation of light $\boldsymbol{k}$, which is perpendicular to the static magnetic field $\boldsymbol{B_0}$.

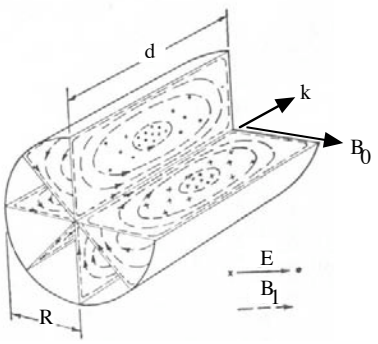

Figure 5.3: Field distribution of the TE_{011} cylindrical cavity mode [58]. Optical access, $\boldsymbol{k}$, for ODEPR is along the axis of the cylinder, at the maximum magnetic field $\boldsymbol{B_1}$, perpendicular to the static field $\boldsymbol{B_0}$.

Commercially available microwave resonators are usually designed for a different geometry, if optical access is available at all. A home made resonator has therefore been considered.

Barrett [59] discusses different kinds of resonators for a longitudinal experiment. Even though his experiment has a different geometry, it also needs to be optimised for a strong $\boldsymbol{B_1}$, so that most of his findings are relevant also for our transverse ODEPR. Barrett considers the cylindrical TE_{011} mode as the 'ideal' choice, but since he does not have enough space in his cryostat, he uses the rectangular TE_{102} mode. For the same reasons I had to choose the rectangular cavity at 14 GHz, but at 35 GHz the shorter wavelength allows a cylindrical design in the TE_{011} mode in our set-up.

The cavity interior is a hollow cylinder of radius R and length d, with one adjustable wall for mechanical frequency tuning. Figure 5.3 shows the field distribution [58] of the chosen cavity mode. $\boldsymbol{B_1}$ is strongest at the axis of the cylinder along which we also provide the optical access. From the distribution of the fields we can also infer, that a hole for optical access in the middle of the circular wall would not disturb the symmetry of the current distribution which follows the electric field distribution close to the wall. We would expect circular currents concentric with the cylinder.

Having decided on the operating mode of the cavity, we still have the choice between an infinite number of diameter to length ratios, $2R/d$, to meet the desired frequency. The specified operating range of the microwave source of the spectrometer is 34.5 to 35.566 GHz. Three slightly different designs have been tested during this thesis. Figure 5.4 shows a mode chart for the cylindrical cavity [60]. From such a plot, we can see which other modes are in our way for a given value of $(2R/d)^2$ for our frequency. We can then

choose a proper diameter for our cavity design. The TE_{011} mode is marked red in the figure. My first two cavity designs fall into the blue region, since the separation of modes is big there and the identification easier. A third design was tested, which falls into the green region, since a better quality factor Q can be achieved for $2R/d = 1$ [60].

Figure 5.4: Mode chart for a cylindrical microwave resonator [60]. The desired TE_{011} mode is indicated with a red line and the regions to which our cavities belong are marked blue and green. R is the cavity radius, d its length, and ν the resonance frequency of the respective mode.

Coupling to the TE_{011} mode

Most lines of the spectrometer as well as the probe are WR 28 rectangular wave-guides (7.11 mm by 3.56 mm inner cross section [61]). The microwaves need to go from such a wave-guide into the cavity.

In order to couple as much of the incoming power as possible into the resonator, the impedance of the cavity has to be matched to the output impedance of the spectrometer. A very simple way to modify the impedance of the cavity is a circular iris between the wave-guide and the cavity [60].

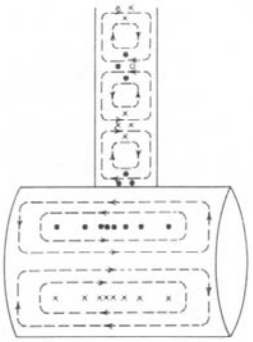

Figure 5.5: Coupling to the TE_{011} cylindrical cavity mode with a WR28 wave-guide from the round wall of the cylinder [60].

The circular iris can be viewed as a combination of an inductive and a capacitive coupling slit. An iris means a slot or hole in a wall at the end of a wave-guide. An inductive iris would be a rectangular slot parallel to the short dimension of the guide, while a slot along the longer dimension gives capacitive coupling. The centred circular iris which we use contains elements of both. The theoretical behaviour of cavity and iris can be described with the help of an equivalent circuit [60]. However, for the experimental spectrometer design the obvious way is tedious but straightforward: drill the hole bigger until maximum coupling is reached.

For a cylindrical cavity in the TE_{011} mode the coupling can be done from the ends or, as we do it, from the side of the cylinder. Figure 5.5 shows how the field distribution in the guide fits to the distribution in the cavity.

First Design

The first cavity design was with $R = 7$ mm and d variable by a few mm around the same value. At 35 GHz this corresponds to the blue region in Figure 5.4. Figure 5.6 shows the absorption due to the TE_{211}, TE_{011}, and TE_{311} modes of this cavity. The frequency resolution of the network analyser is too low (20 MHz) when sweeping over 10 GHz, so that parts of the modes (FWHM $\leq$ 20 MHz) are not resolved and the dips are much deeper in reality. The modes were identified by calculating the mode frequencies with

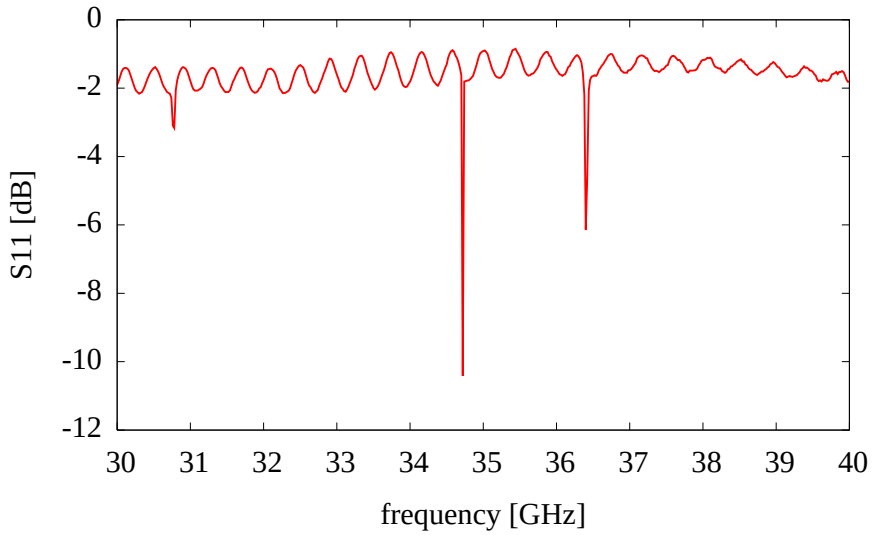

Figure 5.6: Voltage reflection coefficient S_{11} from the $R = 7$ mm cavity design. The modes were identified as TE_{211}, TE_{011}, and TE_{311}.

the following equations [62]:

$$\nu_{mnp}^{\mathrm{TE}} = \frac{c}{2\pi\sqrt{\epsilon_r}}\sqrt{\frac{X_{mn}'^2}{R^2} + \frac{p^2\pi^2}{d^2}} \tag{5.1}$$

$$\nu_{mnp}^{\mathrm{TM}} = \frac{c}{2\pi\sqrt{\epsilon_r}}\sqrt{\frac{X_{mn}^2}{R^2} + \frac{p^2\pi^2}{d^2}} \tag{5.2}$$

where ν_{mnp}^{TE} and ν_{mnp}^{TM} are the eigenfrequencies of the TE and TM mode respectively, denoted by the integers m, n, p. c is the velocity of light in vacuum and ϵ_r is the dielectric constant of the cavity interior. X_{mn} is the n-th root of the m-order Bessel function ($J_m(X) = 0$) and X_{mn}' is the n-th root of the derivative of the m-order Bessel function ($J_m'(X') = 0$). Figure 5.7 shows the calculated frequencies for the TE_{011} and its neighbouring modes with and without liquid helium in the cavity. The calculation is only a rough approximation, since it ignores the sample holder and the sample. Moreover it does neither include the finite conductivity of the material, nor the coupling hole and the optical access holes. The TM_{210} mode and also the TM_{111} (degenerate with TE_{011}) is suppressed, when the movable wall is made slightly smaller in diameter than the cylinder, so that no currents can flow from one wall to the other.

The design works and first ODEPR signals were recorded with this cavity. However, the modes in Figure 5.6 are so close to each other, that they can

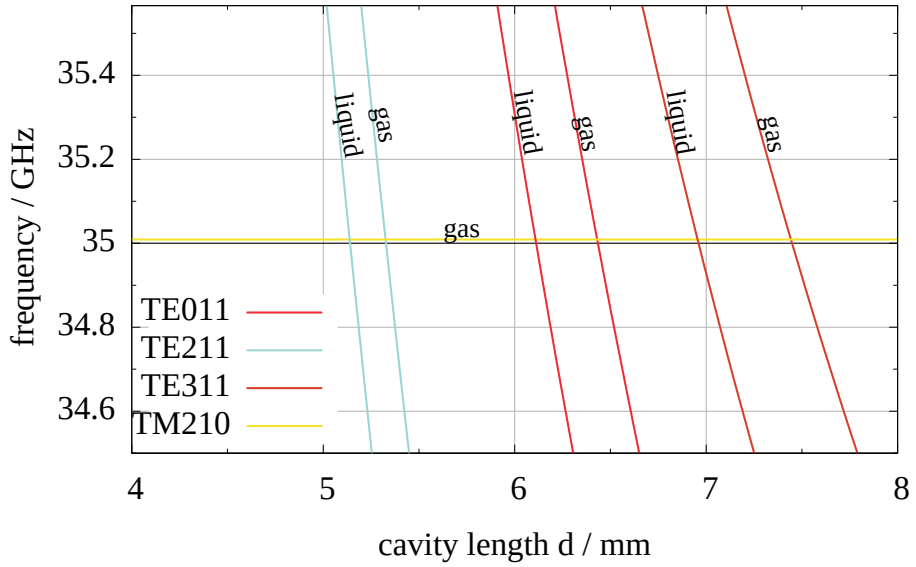

Figure 5.7: Calculated mode frequencies versus cavity length d for a cavity radius of $R = 7$ mm. All modes were calculated with a dielectric constant of 1 for air or gaseous helium and a second time with 1.048 for liquid helium.

all be shifted into the spectrometer frequency range of 34.5 to 35.566 GHz by means of mechanical tuning. This also means that care must be taken not to use the wrong cavity mode, which can easily happen when the cooling of the cavity and the incoming helium move the modes back and forth in frequency. Moreover the cavity does not have any mechanism to adjust the coupling from the wave-guide to the cavity at low temperature. The size of the optimum coupling hole was found to be 2.7 mm in diameter at room temperature. Besides this design does not provide any means of modulation for the static magnetic field B_0.

Second Design

A second design was supposed to provide coils for field modulation. Two slots were cut in the middle of the cylinder jacket (at $\frac{d}{2}$) in order to prevent eddy currents from the modulation field.

This design was a complete failure, since it did not show any microwave absorption peak at all. Even though the slots were parallel to the electric field lines of the TE_{011} cylindrical cavity mode, they have a finite width. In the middle of the cylinder jacket the current is maximum. Obviously the slots disturbed the current so much, that resonance was not observed.

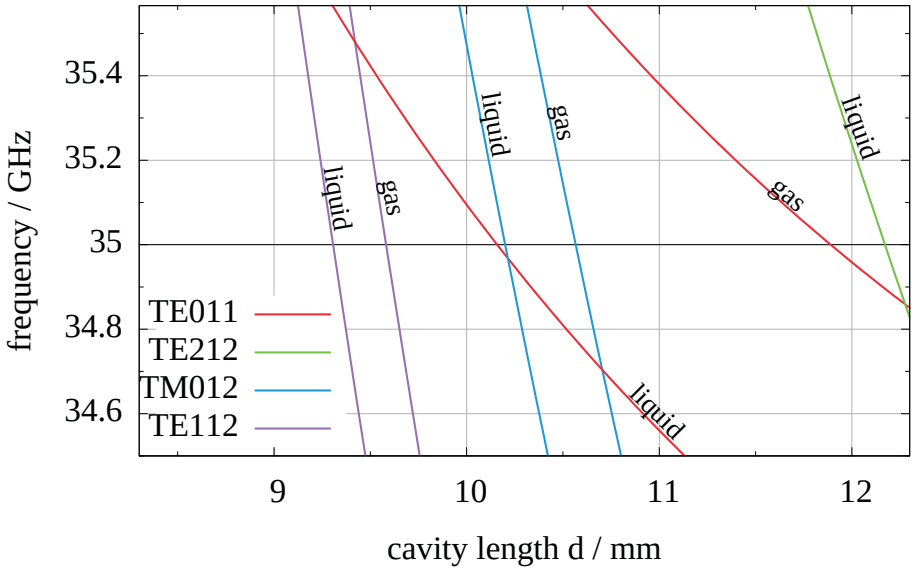

Figure 5.8: Calculated mode frequencies versus cavity length d for a cavity radius of $R = 5.6$ mm. All modes were calculated with a dielectric constant of 1 for air or gaseous helium and a second time with 1.048 for liquid helium.

Third Design

The final design provides field modulation. It has no slots to prevent eddy currents, but the width of the cavity wall was reduced at places under the modulation coils. The mechanical details of this design with its complete probe can be found in Appendix A.2.2. A numerical calculation of the electromagnetic behaviour of this design is the topic of Appendix B.3.

Field modulation can be done with two coils of about 100 windings each. They can be mounted on a teflon holder (Figure A.5) at the side of the cavity. The wire of 0.3 mm diameter is glued to the holder with epoxy resin. Furthermore the new cavity suppresses the unwanted TM_{111} mode (degenerate with TE_{011}), because the movable wall was reduced in size, so that it cannot touch the side walls of the cavity. A connection of the side and the end wall of the cylinder would be needed for the current distribution of TM_{111} [60]. Moreover the inner dimensions were changed to $R = 5.6$ mm and 8.3 mm $\leq d \leq$ 12.3 mm, since all TE_{0np} cylindrical modes have maximum Q for $d = 2R$ [60]. As a further feature a coupling mechanism was introduced in order to modify the coupling at low temperature [63].

Figure 5.8 shows the calculated frequencies for the modes of this newer

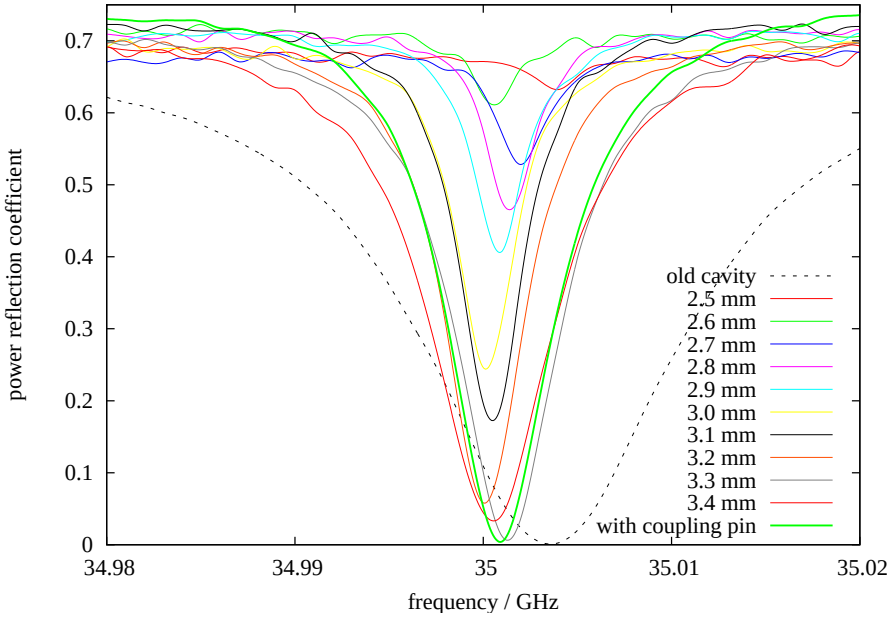

Figure 5.9: Relative power reflected from the microwave cavity for different coupling hole diameters.

design. This chart can be used to identify the modes, which fall into the relevant frequency range. In practice, the TM modes are suppressed, so that in air only the TE_{011} and the TE_{112} can be tuned to be within the range of the ODEPR spectrometer.

The microwave coupling was optimised by drilling the coupling hole bigger until maximum coupling was reached. Figure 5.9 shows the result at room temperature with an empty cavity. At a hole diameter of 3.4 mm the dip is already decreasing, i.e. the cavity is slightly over-coupled. With the newly introduced coupling mechanism we can fine tune the coupling by inserting a little coupling pin into the coupling hole, see green line in the figure. We find a FWHM of 6 MHz, giving an unloaded Q of about 5800 at room temperature.

Unfortunately this design is more sensitive to a change in dielectric constant at the position of the sample, because its electric fields reach further into the centre (Appendix B.3). For measurements on ruby the cavity could not be used, since the TE_{011} mode could not be tuned into the frequency range of the spectrometer with ruby ($l = 1.1$ mm, $d = 3.7$ mm) inside.

5.2.3 Optical Heterodyne Detection

The ODEPR signal is extracted from the laser light by means of optical heterodyne detection in the receiver arm of the spectrometer (parts 2F to 2C in Figure 5.2).

The light-signal with a carrier frequency of about $4 \cdot 10^{14}$ Hz contains Fourier sidebands at 35 GHz and the 50 kHz modulation frequency of the PEM. This signal is converted to an electrical signal of 35 GHz carrier frequency in the fast photdiode (2F) and goes through the isolator (2E) which protects the diode from reflections. The first amplification stage is a low noise amplifier (2D). The amplified signal is down converted in the microwave mixer (2C), before it goes through another amplification stage at low frequency (50 kHz). Finally the 50 kHz modulation is removed in the lock-in amplifier.

For a good receiver, the following elements are most important:

- optics which focus the beam to a size at most equal to the active area of the detector (and which fully overlap Raman wave and local oscillator laser light)
- a photodetector with high bandwidth and responsivity
- a low-noise amplifier with a noise figure low enough and amplification high enough, so that the following receiver stages do not introduce more noise
- a lock-in amplifier with a high dynamic reserve (detectable signal power per noise power in dB)

The optics will not be described in detail, since many different configurations are used. Usually it consists of mirrors and lenses and sometimes an optical fibre system.

Two different photodiodes were used for the 35 GHz experiments. The New Focus 1437M was also used at 14 GHz. For this detector the free light beam was focused with a lens onto the diode. The other detector is a New Focus 1004, which is fibre coupled. Table 5.3 shows the specifications of the two detectors.

The low noise amplifier is a Miteq JSD4-34353565-38-10P, with a noise figure of between 3.07 and 3.38 dB depending on the frequency. Such a bad noise figure (for comparison, the 14 GHz low noise amplifier has a maximum noise figure of 1.25 dB) is normal for commercially available components at 35 GHz.

For the final lock-in detection we use a Stanford Research SR830 with a dynamic reserve of >100 dB.

	1004	1437M
wavelength range	400-900 nm	400-1650 nm
3 dB bandwidth	35 GHz (min.)	21 GHz (25 GHz specified)
conversion gain	6.6 V/W	5 V/W
responsivity	0.2 A/W	0.2 A/W
output impedance	100 Ω	200 Ω (50 Ω specified)
noise equivalent power	70 pW/$\sqrt{\text{Hz}}$	90 pW/$\sqrt{\text{Hz}}$
cw saturation power	5 mW	10 mW
max. pulse power	200 mW	200 mW
detector material	GaAs	InGaAs/Schottky
detector diameter	12 μm	25 μm
dc gain	1 mV/μA	1 mV/μA

Table 5.3: Specifications of the two fast photodiodes. The specified bandwidth of our version of the 1437M differs from the official specifiations, because the load resistor was changed to 200 Ω. Conversion gains and responsivities are specified at the optimal wavelength.

5.2.4 Signal-To-Noise Ratio

The most important criterion for the system performance of a spectrometer is its signal-to-noise ratio: if it is bigger than 1, a signal can be observed with a single scan.

Since a signal can conveniently be measured as peak to peak voltage S^{pp}, we use also peak to peak noise voltage N^{pp}, when we want to compare with the signal. This means a factor of $2\sqrt{2}$ compared to root mean square (rms) noise N, which is more convenient when noise figures are analysed.

Noise at the Receiver Output

A good 35 GHz ODEPR signal from the R-lines of Ruby has $S^{\text{pp}} = 350$ μV with a noise of $N^{\text{pp}} = 11$ μV and a bandwidth of 0.125 Hz. The bandwidth of the experiment is determined by the time constant and the roll-off of the lock-in amplifier.

Noise measurements confirm an rms noise voltage of

$$\frac{N}{\sqrt{\text{Hz}}} = (12 \pm 1)\frac{\mu\text{V}}{\sqrt{\text{Hz}}} \tag{5.3}$$

at the lock-in amplifier of the fully assembled spectrometer. The noise spectrum is shown in Figure 5.10. The main peak at 11 kHz results from the

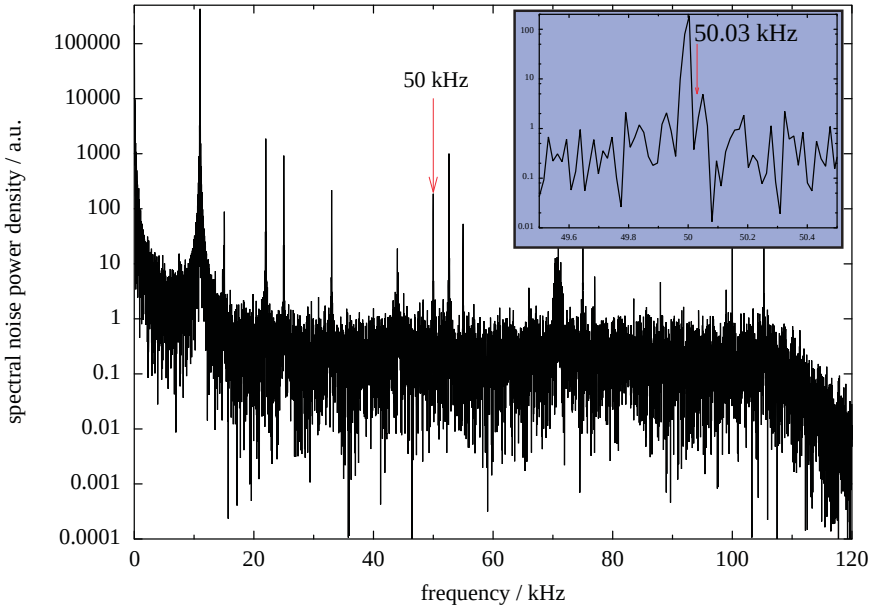

Figure 5.10: Noise spectrum of the fully assembled 35 GHz receiver. The red arrows indicate the optical modulation frequency (50.03 kHz) of the spectrometer. The inset shows the region around 50 kHz enlarged.

modulation of the AFC system (Section 5.3), while the decrease at the high frequency end comes from a low pass filter in the measurement. Since the figure shows a noise peak at 50 kHz it is important to notice, that the exact PEM frequency is at 50.03 kHz and happens to fall into a trough of the spectrum (see inset in the figure).

Noise of a Multi-Stage Receiver

For a proper noise analysis of the system, the receiver arm of the spectrometer can be viewed as a multistage receiver (Figure 5.11).

In order to characterise a system made of many successive stages we can introduce a noise figure F, which can be defined as the ratio of the power signal to noise ratios before and after the device.

$$F = \frac{P_{\mathrm{S}}^{(\mathrm{in})}/P_{\mathrm{N}}^{(\mathrm{in})}}{P_{\mathrm{S}}^{(\mathrm{out})}/P_{\mathrm{N}}^{(\mathrm{out})}} \tag{5.4}$$

Another figure of merit is the gain G, which is the ratio of signal powers after

and before the device.

$$\begin{aligned} G &= P_{\mathrm{S}}^{(\mathrm{out})}/P_{\mathrm{S}}^{(\mathrm{in})} \\ \text{therefore } F &= \frac{P_{\mathrm{N}}^{(\mathrm{out})}}{P_{\mathrm{N}}^{(\mathrm{in})} G} \end{aligned} \tag{5.5}$$

The gain G_i and noise figures F_i for the separate devices i in a cascade of components relate to the overall gain G and noise figure F via Friis' formula [64]

$$\begin{aligned} F &= F_1 + \frac{F_2 - 1}{G_1} + \frac{F_3 - 1}{G_1 G_2} + ... \\ \text{and } G &= G_1 G_2 G_3 ... \end{aligned} \tag{5.6}$$

In the following we will denote the respective decibel values with lower case letters g_i and f_i, so that $G_i = 10^{g_i/10}$ and $F_i = 10^{f_i/10}$.

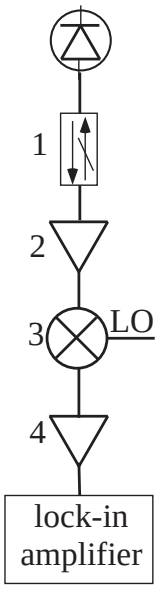

Figure 5.11: Receiver arm of the 35 GHz spectrometer, consisting of photodiode, isolator (1), low noise amplifier (2), mixer (3), low frequency amplifier (4), and lock-in amplifier.

We consider now the relevant items in the 35 GHz heterodyne receiver (Figure 5.11).

The first step in the cascade is the isolator (1 in Figure 5.11). Since no data-sheets were available the S-parameters [61] of the isolator were measured with a Wiltron Model 36 B network analyser (at the *Lehrstuhl für Hochfrequenztechnik*). In our noise measurement (Equation 5.3) the local oscillator frequency was 34.665 GHz. At this frequency the transmitted voltage is $S_{21} = -0.58$ dBc. Since it is given in dB, this is also the power gain $g_1 = -0.58$ dB, i.e. $G_1 = 0.875$. The noise figure of a passive device is equal to its loss [65], therefore $f_1 = 0.58$ dB, or $F_1 = 1.143$.

Noise introduced via the local-oscillator into the mixer is not specified by the manufacturer and ignored in the following analysis. Instead, we treat stage 3 as a passive device, with the noise figure given by its loss: $f_3 = 5.8$ dB.

The gain of the LF amplifier was measured to be $g_4 = 59.7$ dB. The input impedance of this device is 54 Ω at 50 kHz, so that we will consider it matched to the mixer output impedance of 50 Ω. With 50 Ω at the input to the amplifier, the noise at the output was measured with the lock-in amplifier

to be

$$\frac{N_{\text{out4}}}{\sqrt{\Delta\nu}} = 2.2\frac{\mu\text{V}}{\sqrt{\text{Hz}}} \; . \tag{5.7}$$

The noise of the $R = 50\ \Omega$ resistor at a temperature $T = 290K$ is [66, 64]

$$\frac{N_{\text{in4}}}{\sqrt{\Delta\nu}} = \sqrt{4k_BTR} = 0.89\frac{\text{nV}}{\sqrt{\text{Hz}}} \; . \tag{5.8}$$

Replacing the powers in Equation 5.5 by the squares of the voltages, we can calculate the noise figure of the LF amplifier. It is

$$\begin{aligned} F_4 &= \frac{P_{\text{N}}^{(\text{out4})}}{P_{\text{N}}^{(\text{in4})}G_4} = \frac{N_{(\text{out4})}^2}{N_{(\text{in4})}^2 G_4} \\ f_4 &= 8.16 \text{ dB} \end{aligned} \tag{5.9}$$

This amplifier is the only non-commercial device in the cascade, it was made in the electronics workshop of our institute. Its bad performance might be taken as a hint to use commercial devices also for the low frequency parts, when it is critical. In this case, however, we see from Table 5.4, that its contribution to the overall noise figure of the system is small.

The noise on the input of this last stage in the cascade is already too low to be measured directly with the lock-in amplifier.

The noise figures and gains for the other items in the cascade were taken from the data-sheets at the above mentioned frequency and are also given in Table 5.4, which summarises the specifications. The 'contribution to F' is the respective summand in the Friis' formula, i.e. the contribution of this stage to the overall noise figure.

index	item	gain	noise figure	contribution to F
1	isolator	-0.58 dB	0.58 dB	1.143
2	low noise amplifier	26 dB	3.1 dB	1.191
3	mixer	-5.8 dB	5.8 dB	0.008
4	LF amplifier	59.7 dB	8.16 dB	0.061

Table 5.4: Contribution of the four stages to the system noise figure.

With Equation 5.6 we can calculate the gain g and noise figure f of the receiver.

$$\begin{aligned} g &= 79.3 \text{ dB} \\ f &= 3.8 \text{ dB} \end{aligned} \tag{5.10}$$

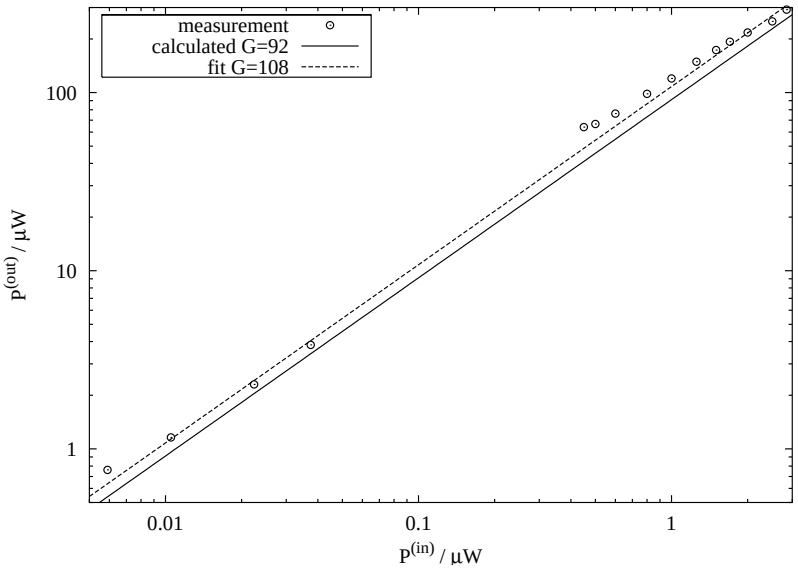

Figure 5.12: Gain of the first 3 stages of the heterodyne receiver. The dashed line shows a linear fit ($G = 108 \pm 3$) to the measurement (circles) and the solid line shows the calculated gain.

For comparison, the common gain of stages 1, 2, and 3 in the cascade (Figure 5.11) was measured with a network analyser as an external source.

For this measurement the power from the network analyser was measured with a Hewlett-Packard Model 435 B power meter for several power settings between 0.45 μW and 2.85 μW at a frequency of 35 GHz. Since the usual input powers of the heterodyne receivers are lower than that, a nominally 20 dB attenuator was calibrated with the network analyser (result: 18.8 dB $\pm$ 0.5 dB). The lower powers, which cannot be measured accurately with the power meter, could then be calculated from the powers in the μW range.

The calibrated terminal of the network analyser was then connected to the isolator (1 in Figure 5.11) to provide the input power $P^{(\mathrm{in})}$. The output from the mixer (3) was connected to an oscilloscope parallel to a 50 Ω termination. The network analyser was set to a fixed frequency of 35 GHz, while the local oscillator frequency of the heterodyne receiver was adjusted around 35 GHz to watch a beat signal in the range of 400 kHz to 2 MHz. The amplitude of the beat signals did not depend significantly on the frequency. The rms voltage of the beat was recorded for different power settings and its square divided by 50 Ω was taken to be the output power $P^{(\mathrm{out})}$ after the third stage of the cascade. The result is displayed in Figure 5.12. From the gain of the

separate components we expect $G = G_1G_2G_3 = 92$ (19.6 dB), whereas the fit to the data gives $G = 108 \pm 3$ (20.3 dB). The relative deviation of the calculation from the fit of roughly 15% gives a measure for the reliability of the above calculations.

Noise at the Receiver Input

With no light on the diode, the noise will be dominated by the thermal noise in the resistors. The thermal noise at the input of the receiver is $k_BT = 4 \cdot 10^{-21} \frac{\mathrm{W}}{\mathrm{Hz}}$.

Knowing the output noise $P_{\mathrm{N}}^{(\mathrm{out})} = N_{\mathrm{out}}^2/50\Omega$ after the final stage of the receiver cascade (Equation 5.3) and the gain g and noise figure f of the cascade (Equation 5.10) we can calculate the noise at the input of the receiver and compare with the expected noise.

From Equation 5.5 we get

$$\frac{P_{\mathrm{N}}^{(\mathrm{in})}}{\Delta\nu} = \frac{P_{\mathrm{N}}^{(\mathrm{out})}}{FG\,\Delta\nu} = 1.4 \cdot 10^{-20}\ \frac{\mathrm{W}}{\mathrm{Hz}} \tag{5.11}$$

That the resulting noise is slightly higher, than the thermal noise k_BT indicates, that the assumed noise figures from the data sheets are too low, at least for the assembled spectrometer. Especially the noise introduced via the local oscillator of the mixer was not taken into account.

Comparison to 14 GHz ODEPR

The 14 GHz prototype spectrometer had a double sideband gain of 86.8 dB [26]. The one described in Section 5.1 has only 82.4 dB, due to the slightly weaker home built amplifier. This value corresponds to 79.4 dB amplification for each quadrature channel, compared to 79.3 dB for the 35 GHz instrument, which has only one channel.

Also the noise performance is comparable. At 14 GHz it is 13 to 14 $\frac{\mu\mathrm{V}}{\sqrt{\mathrm{Hz}}}$ [56] compared to $(12 \pm 1)\frac{\mu\mathrm{V}}{\sqrt{\mathrm{Hz}}}$ as found above.

However, we clearly find bigger signals at 14 GHz. For example at 692.2 nm the peak-to-peak voltage of a 14 GHz spectrum is of the order of 1 mV (optical power 780 μV, microwave power about 90 mW), while at 35 GHz we measure only about 100 μV (optical power 700 μV, microwave power about 40 mW). This can be attributed to the higher power available and to the better conversion of the signal in the photodetector at lower frequency.

In conclusion, the worse signal-to-noise ratio of the 35 GHz spectrometer relative to that of the 14 GHz spectrometer has to be attributed to less signal, not to more noise. Possible improvements to the 35 GHz spectrometer should

therefore aim at higher signals, for instance by increasing the microwave or optical excitation power.

5.3 Automatic Frequency Control

Systems for automatic frequency control (AFC) have been designed and built. These electronic feedback systems are used to stabilise the frequency of the 14 GHz as well as the 35 GHz spectrometer.

5.3.1 General Idea

The use of an AFC system is to keep the microwave (MW) frequency at the resonance frequency of the microwave cavity while recording (in our case ODEPR) spectra.

There are two different concepts to keep the frequency of spectrometers at the desired value. One concept is to lock a servo loop to the spectrometer cavity, the other is to have a separate temperature stabilised MW cavity to lock to. While the former method prevents slow frequency drifts the latter is useful to stop fluctuations and distortions of the frequency axis of the spectrum (see [53], chapter 6). With our AFC we mainly want to prevent drift of the frequency. Therefore we lock our AFC loop to the actual sample cavity.

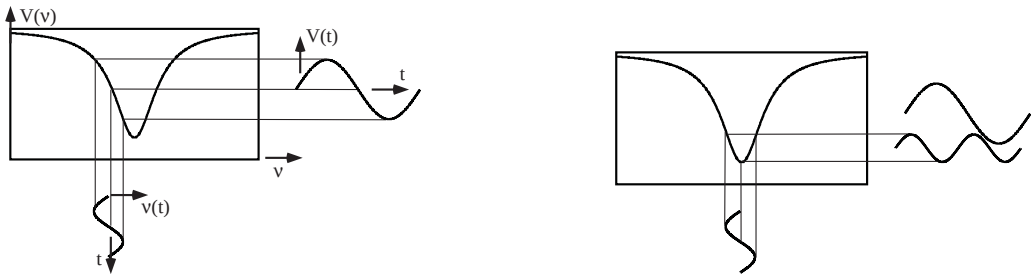

Figure 5.13: Modulating the Dip. On resonance the response is a second harmonic signal.

Figure 5.13 illustrates the general idea behind the working of an AFC. The MW frequency of the spectrometer is frequency modulated with a frequency ($\nu = 11$ kHz) that has no disturbing harmonics coinciding with other frequencies in the spectrometer. A sinusodial frequency $\nu(t)$ modulates the voltage going into the microwave cavity where the MWs are partly absorbed. The voltage $V(\nu)$ reflected from the MW cavity therefore shows a dip (Figure

5.13) at the resonance frequency. This voltage $V(\nu)$ is of course also modulated with the modulation frequency $\nu(t)$ (and higher harmonics). This leads to a sinusodial time dependence of the detected voltage $V(t)$ when we approximate the side of the dip by a straight line. When the mean MW frequency comes closer to the middle of the dip the previously sinusodial $V(t)$ is distorted and its amplitude decreases. When it reaches the resonance frequency the amplitude is lowest and the time dependence is the second harmonic (22 kHz) of the modulation. Another way to look at it is, that the amplitude of the outcoming modulation voltage is approximately the derivative of the dip, which is zero in the middle of the dip.

The idea of AFC is to adjust the mean microwave frequency electronically in such a way, that the voltage $V(t)$ which is reflected from the MW cavity approaches zero amplitude. If we achieve this, the MW frequency stays on resonance. The operator of the system can assure himself of its working by watching the second harmonic signal on a scope.

5.3.2 Implementation

The electronics of the AFC system (see also Appendix B.1) can be separated into two modules: a mod-module (modulation), which provides the 11 kHz signal with the desired amplitude and offset; and the PI-module (proportional-integral controller), which demodulates the signal from the microwave mixer with the 11 kHz reference and provides an error signal. From this error signal, the modulation module can generate a corrected offset for the 11 kHz signal, which is fed back to the microwave source. In older versions of the AFC system, the PI-module is replaced by a lock-in amplifier.

A simplified overview of the spectrometer is given in Figure 5.14. The figure shows only those parts of the spectrometer which are relevant for AFC.

The mod-module modulates the frequency of the MW about its mean value $\frac{\omega_c}{2\pi}$. The modulation frequency is $\frac{\omega_m}{2\pi} = 11$ kHz. Therefore the frequency modulated voltage has the following time dependence

$$\sin\left(\omega_c t + m\frac{\omega_c}{\omega_m}\cos(\omega_m t)\right)$$

where m is a proportionality constant and t is the time. The time dependence of the modulated frequency is the derivative of the argument of the sine:

$$\nu(t) = \frac{\omega_c}{2\pi}\left(1 - m\sin(\omega_m t)\right)$$

$\frac{m\omega_c}{2\pi}$ is the variation width of the frequency which can be set manually at the mod-module. An additional dc offset from the mod-module also adjusts the carrier frequency $\frac{\omega_c}{2\pi}$.

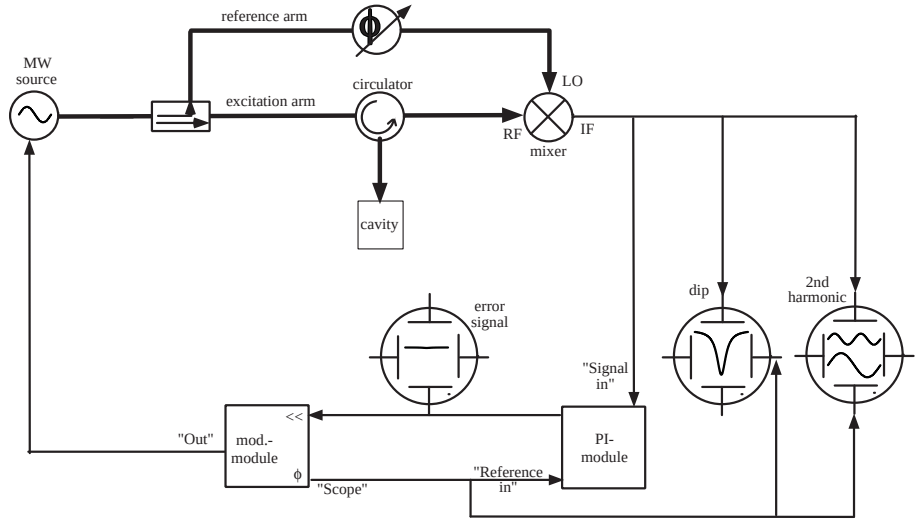

Figure 5.14: Overview of the AFC system.

The modulated microwaves are split between excitation arm and reference arm of the spectrometer. From the excitation arm the microwaves go down to the cavity and a circulator takes the reflected waves to a mixer (or diode in the case of the 35 GHz spectrometer). Here the signal is mixed with the phase shifted reference (ϕ) from the reference arm. If we adjust the phase of the reference arm we can see the microwave absorption or dispersion at the intermediate frequency (IF) output of the mixer. Since we want a dip for AFC we adjust the phase in the reference arm to see the absorption. Note: the original 14 GHz set-up and our 35 GHz set-up do not use a reference arm and a mixer, but just a MW detection diode instead of the mixer. The reason for this new set-up is the possibility to use a quadrature mixer and detect absorption and dispersion of conventional electron paramagnetic resonance.

The 11 kHz signal from the IF output of the MW mixer is demodulated with a mixer in the PI-module of the AFC. The output from the PI-module should be zero when the system is locked to the middle of the dip and non-zero when the frequency deviates from resonance. This 'error' signal is fed back to the mod-module where it is added to the offset voltage which determines the mean frequency of the MW source. In this way the mean MW frequency is readjusted to the resonance of the MW cavity. The amplification of the feedback can be adjusted with the proportional and integral regulation knobs on the PI-module while the phase of the 11 kHz reference from the mod-module can be changed with a phase shifter. Further the operator can monitor the MW dip, the error signal from the PI-module, the second

harmonic signal and the 11 kHz reference on the three oscilloscopes in the set-up.

5.4 ODEPR Spectra

5.4.1 Introduction

We have already experimentally proved the validity of both, the rotating MCD theory, as well as the coherent Raman description of the ODEPR experiment at 14 GHz elsewhere [3, 6]. In particular, we have shown how relative orientations of the optical and magnetic tensors can be obtained from metalloprotein ODEPR spectra [7, 2] and we have analysed the R-lines of ruby at 14 GHz [6]. These results were partly obtained with the prototype spectrometer [16, 56] and partly with that described in Section 5.1. Here we can therefore focus on the new possibility to measure ODEPR at 35 GHz.

Energy Levels

First 35 GHz ODEPR spectra were obtained on the R_2-line of our test system ruby. We have already described the relevant energy contributions for ODEPR on the R-lines of ruby elsewhere [6]; a summary is presented here.

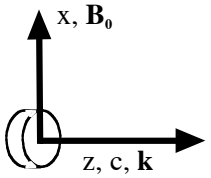

Figure 5.15: Coordinate system. The cylinder indicates the ruby sample.

The crystal is mounted with its symmetry axis c along the laser beam $\boldsymbol{k}$, i.e. perpendicular to $\boldsymbol{B_0}$. We use a co-ordinate system with the x axis along $\boldsymbol{B_0}$ and the z axis along the c axis of the sample. The ground state Hamiltonian can be written in matrix form (in a basis $\phi_{g;n}(n = 1, 2, 3, 4)$, where states can be labelled by the magnetic quantum numbers $|M_S^z\rangle$ with M_S^z = -3/2, -1/2, 1/2, 3/2) as

$$\mathcal{H}_g = \begin{pmatrix} D & \frac{\sqrt{3}}{2}\Omega_x & 0 & 0 \\ \frac{\sqrt{3}}{2}\Omega_x & -D & \Omega_x & 0 \\ 0 & \Omega_x & -D & \frac{\sqrt{3}}{2}\Omega_x \\ 0 & 0 & \frac{\sqrt{3}}{2}\Omega_x & D \end{pmatrix} , \tag{5.12}$$

where D is the zero field splitting parameter and $\Omega_x = g_x\mu_B B_x$ is the Larmor frequency. μ_B is the Bohr magneton and B_x is the magnetic field perpendic-

ular to the c-axis of the crystal. The eigenvalues are

$$E_{1,3} = -\frac{1}{2}\Omega_x \mp \sqrt{\Omega_x^2 + D^2 + \Omega_x D}\,, \tag{5.13}$$

$$E_{2,4} = \frac{1}{2}\Omega_x \mp \sqrt{\Omega_x^2 + D^2 - \Omega_x D}\,. \tag{5.14}$$

The eigenvalues are plotted versus magnetic field in Figure 5.16. The ver-

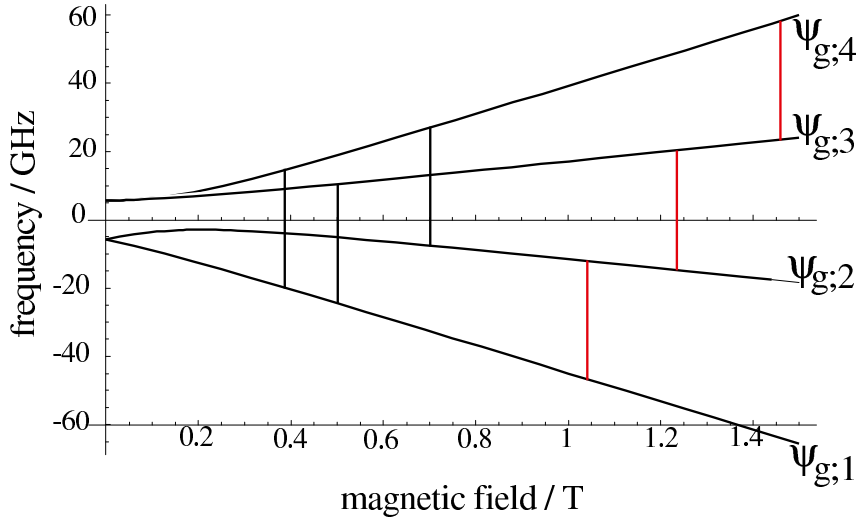

Figure 5.16: Energy splitting of the ground state of ruby due to a magnetic field perpendicular to the c-axis of the crystal. The vertical lines indicate energy differences of 35 GHz, while the nomenclature of the respective eigenstate $\psi_{g;n}$ is indicated on the right. Transitions which are observed in the ODEPR experiment are highlighted in red.

tical lines in this figure represent energy differences corresponding to the microwave frequency of 35 GHz. The corresponding field values are 0.393 T, 0.501 T, 0.707 T, 1.057 T, 1.234 T, and 1.464 T. The microwave transitions of the ODEPR signal, which we observe, correspond to the three high field resonances.

In the basis of the states $\phi_{e;5,6} = \left|{}^2E, u_+, -\frac{1}{2}\right\rangle$, $\left|{}^2E, u_-, \frac{1}{2}\right\rangle$ and $\phi_{e;7,8} = \left|{}^2E, u_-, -\frac{1}{2}\right\rangle, \left|{}^2E, u_+, \frac{1}{2}\right\rangle$, the Hamiltonian for the excited states is

$$\mathcal{H}_e = \frac{1}{2}\begin{pmatrix} -\lambda_R - \Omega_z^{(1)} & \Omega_x^{(1)} & 0 & 0 \\ \Omega_x^{(1)} & -\lambda_R + \Omega_z^{(1)} & 0 & 0 \\ 0 & 0 & \lambda_R - \Omega_z^{(2)} & \Omega_x^{(2)} \\ 0 & 0 & \Omega_x^{(2)} & \lambda_R + \Omega_z^{(2)} \end{pmatrix},$$

where λ_R is the separation between the two R lines, $\Omega_z^{(1,2)} = g_z^{(1,2)}\mu_B B_0 \sin(\theta)$ and $\Omega_x^{(1,2)} = g_x^{(1,2)}\mu_B B_0 \cos(\theta)$, where $g_{x,z}^{(1,2)}$ are the splitting factors of the excited state. Since the excited state has a highly anisotropic g tensor, the misalignment of angle θ between c axis and the laboratory z axis has to be taken into account. The superscripts (1) and (2) refer to the R_1 and R_2 line respectively.

The energy eigenvalues E_n of $\mathcal{H}_e$ are:

$$E_{5,6} = E(R_1) \mp \frac{1}{2}\sqrt{\Omega_x^{(1)2} + \Omega_z^{(1)2}}\,, \tag{5.15}$$

$$E_{7,8} = E(R_2) \mp \frac{1}{2}\sqrt{\Omega_x^{(2)2} + \Omega_z^{(2)2}}\,. \tag{5.16}$$

Transition-Matrix Elements

In addition to the energies E_n, we need also the eight eigenstates $\psi_{g;n}(n = 1..4)$ and $\psi_{e;n}(n = 5..8)$ of the two Hamiltonians. The matrices $\mathbf{M_g}$ and $\mathbf{M_e}$, which contain the $\psi_{g;n}$ and $\psi_{e;n}$ as their columns diagonalise $\mathcal{H}_g$ and $\mathcal{H}_e$, respectively.

$\mathbf{M_g}$ and $\mathbf{M_e}$ transform all transition matrix elements from the basis $\phi_{g,e;n}$ to the basis $\psi_{g,e;n}$, in which the Hamiltonians are diagonal:

$$\mu_g^{z,mag} = g_z\mu_B \mathbf{M}_g^T \mathbf{S'}_{z,g} \mathbf{M}_g \tag{5.17}$$

$$\mu_e^{z,mag} = \mathbf{M}_e^T \mu'^{mag} \mathbf{M}_e\,, \tag{5.18}$$

$$\mu^{\pm} = \mathbf{M}_e^T \mu'^{\pm} \mathbf{M}_g\,, \tag{5.19}$$

where the prime denotes variables in the basis $\phi_{g,e;n}$. The left hand side are the transition matrix elements for the magnetic transitions within the ground ($\mu_g^{z,mag}$) and excited ($\mu_e^{z,mag}$) states and the circularly polarised optical transitions ($\mu^{\pm}$) in the basis $\psi_{g,e;n}$.

The explicit form [6] of the eigenvectors and transition matrix elements is not repeated here for brevity. With the eight relevant states $\psi_{g,e;n}$ the system is defined.

Experimental Checks

ODEPR was measured on the R_2 line of ruby sample I. All measurements were done at low temperature, where the ODEPR signal is strongest due to the Boltzmann factor. The optical power on the photodiode was around or slightly lower than 1 mW. Figure 5.17 shows spectra at 4 different wavelengths. The experimental parameters are given in the figure.

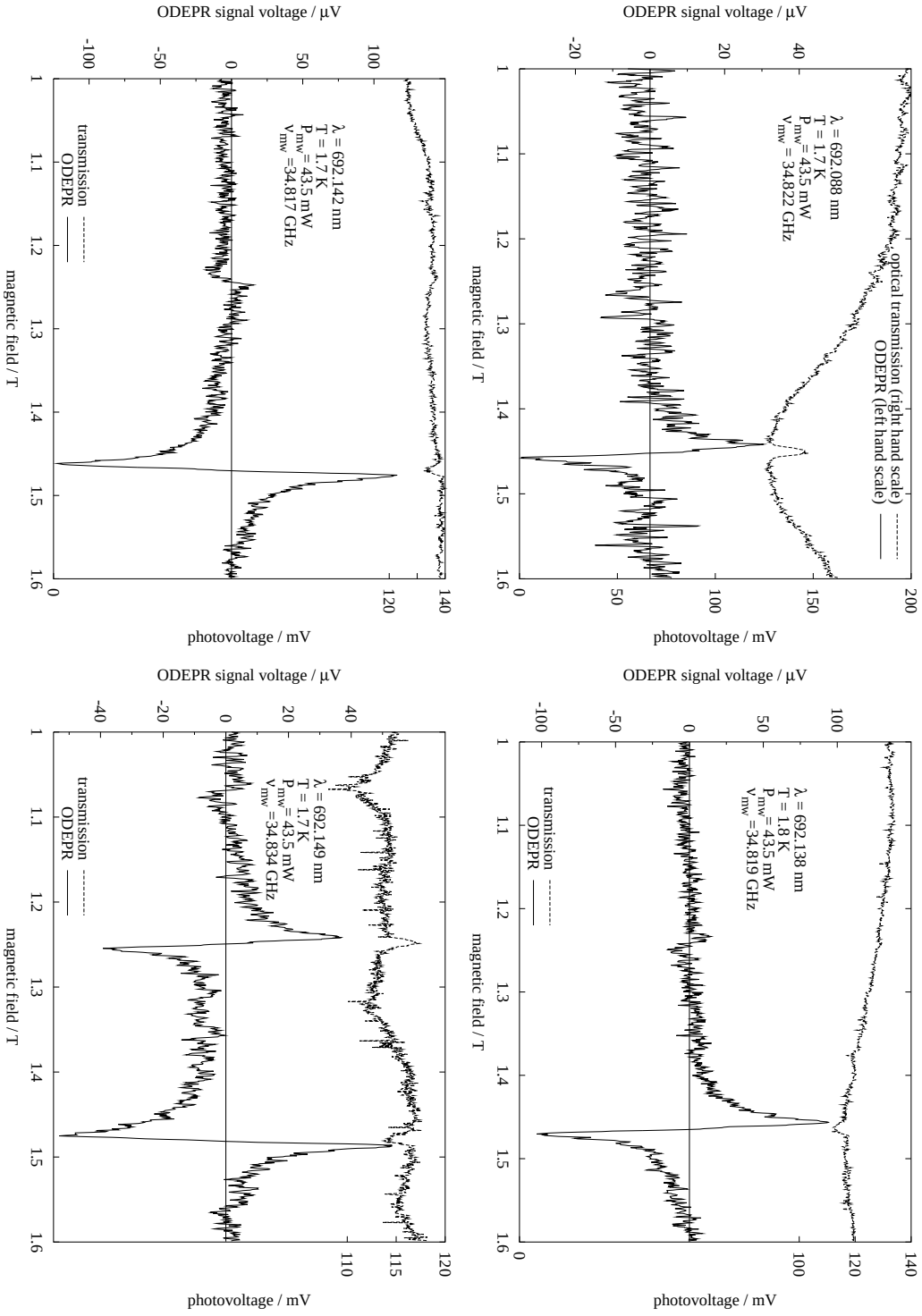

Figure 5.17: 35 GHz ODEPR spectra of ruby sample I. The left hand scale gives the ODEPR signal voltage. The optical transmission is shown as dc photo-voltage of the optical detector on the right hand scale.

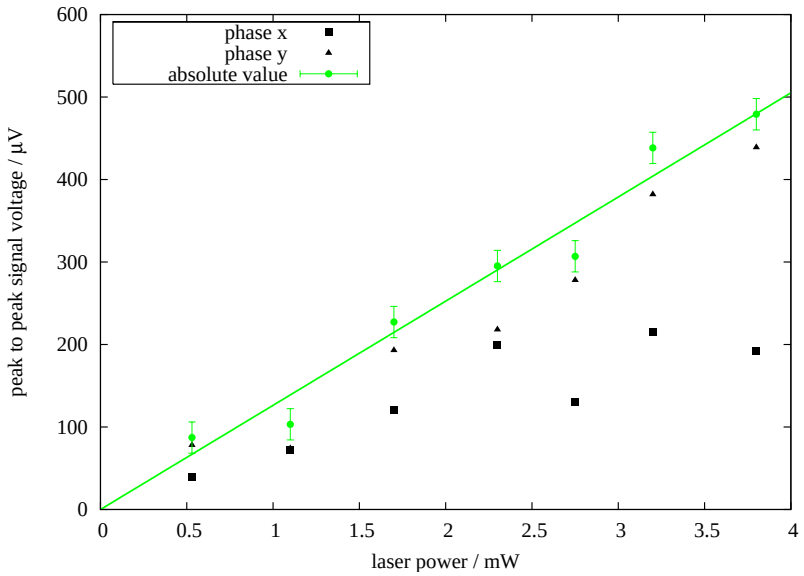

Figure 5.18: Laser power dependence of 35 GHz ODEPR on the example of the high field resonance, $\lambda = 692.14$ nm.

At 692.088 nm (upper left in Figure 5.17) we see mainly the high field transition in the ODEPR spectrum, which arises from the ground states $\psi_{g;3}$ and $\psi_{g;4}$ (Figure 5.16). When we increase the optical wavelength λ (λ is given in Figure 5.17), i.e. go down in optical transition energy, we can additionally watch the middle resonance due to the transition between $\psi_{g;2}$ and $\psi_{g;3}$, until we finally see also the low field resonance between $\psi_{g;1}$ and $\psi_{g;2}$ at 692.149 nm. The photo-voltage, which is proportional to the optical transmission is also displayed in the figures. When the EPR resonance condition is met, the populations change and little 'holes' appear on the transmission curve.

The three experimentally visible transitions are the ones, which would be magnetic dipole allowed (magnetic quantum number M_S^z changes by ± 1) in a longitudinal experiment ($\boldsymbol{B_0}$ along the crystal c axis), but care must be taken to use such concepts in this transverse experiment ($\boldsymbol{B_0}$ perpendicular to the c axis), when M_S^z is not a good quantum number, since the Hamiltonian $\mathcal{H}_g$ (Equation 5.12) is not diagonal in this basis ($\phi_{g;n}$). From calculation (Figure 5.21) we see, that also the 0.393 T resonance should give rise to a small but non-zero ODEPR, but this is not observed in the experiment.

From the theory, Equation 2.16, we would expect the signal to be proportional to the laser intensity (square of the laser field). Furthermore, it is proportional to ω_R, i.e. the square-root of the microwave power.

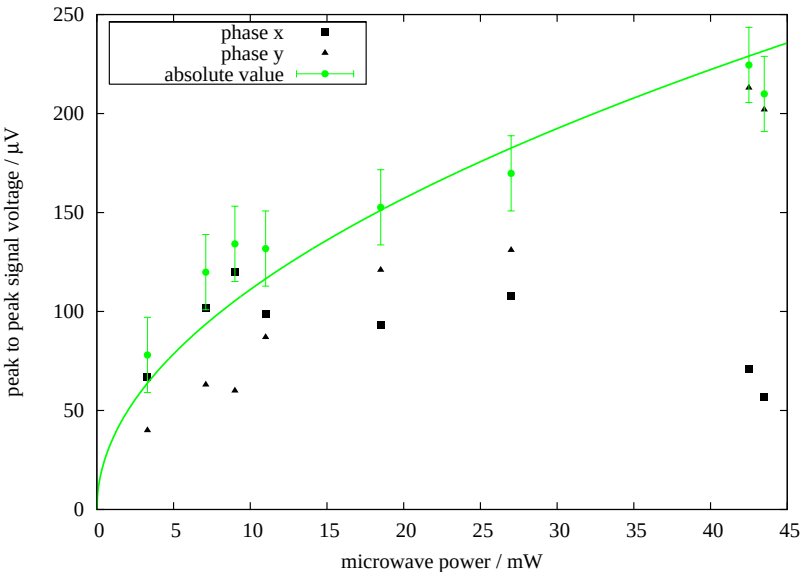

Figure 5.19: Microwave power dependence of 35 GHz ODEPR. on the example of the high field resonance, $\lambda = 692.14$ nm. The fit is proportional to the square root of the microwave power.

In order to measure a complete ODEPR spectrum, we need to down convert the signal with some arbitrary microwave reference phase φ and then a second time with the quadrature phase $\varphi + 90°$. The signals obtained from these two references are x and y. In the 35 GHz spectrometer this needs to be done in two separate runs. Figure 5.18 shows the peak-to-peak voltages of the high field resonance of one particular wavelength as an example for the linearity of the laser power dependence. Squares and triangles denote two quadrature phases x and y, while the green circles show the absolute value $\sqrt{x^2 + y^2}$. The error bars in the figure show the peak-to-peak noise of the instrument. The fitted straight line goes through the origin. The square-root dependence from the microwave power is demonstrated in Figure 5.19.

Obviously the absolute phase φ is not stable between the runs, but when both phases are evaluated, the dependencies are as expected. The main reason for this phase change is the change of the liquid helium level in the waveguide of the probe by evaporation. It can partially be compensated by optimising the helium flow into the sample space. This was done in the experiments presented here.

Under the conditions of the experiment (1.6 K, 43.5 mW MW power), the absorption phase of the signal is fully microwave power saturated. This

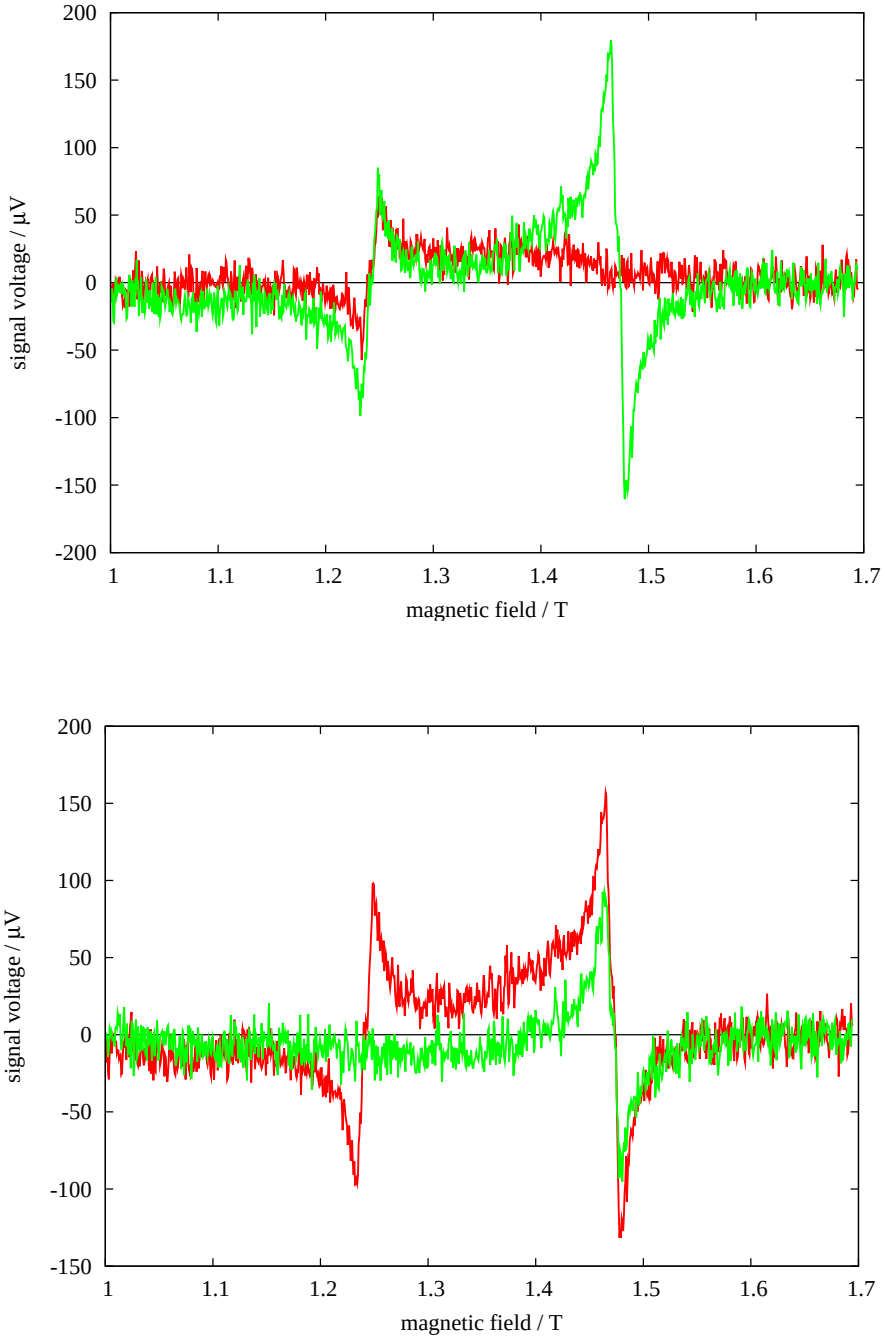

Figure 5.20: The absorption phase of middle and high field resonance is microwave power saturated, as can be shown by turning the phase. Both plots show the same spectrum. $P_{\mathrm{mw}} = 43.5$ mW, $\lambda = 692.141$ nm.

is demonstrated on the middle and high field resonances in Figure 5.20. Both plots show the same two spectra at quadrature phases (green and red). In the upper graph, the absolute phase φ was adjusted, so that the high field resonance shows only the dispersion signal (green), while the red line is flat at high field, where absorption would be expected. In the lower graph, φ was chosen such that the low field resonance shows a flat (green) line for the absorption.

For inhomogeneously broadened lines the absorption saturates easier than the dispersion also in EPR [67]. In particular, ODEPR measurements at 14 GHz show fully saturated absorption for the R lines of ruby [6]. However, it is interesting, that also at higher frequency (35 GHz instead of 14 GHz) and with lower power (43.5 mW instead of 150 mW) the absorption is still fully saturated. As mentioned before, it is theoretically expected, but sometimes not observed in the experiment, that T_1 is shorter and saturation less likely at higher frequency [57]. We can only measure T_1 at a single frequency of 14 GHz with our experimental equipment (Section 6.1).

5.4.2 Wavelength Dependence

Prediction

The dependence of the ODEPR spectra on magnetic field and laser wavelength can also be calculated numerically with the theory from Section 2.2. At 14 GHz we found experimentally [6], that the triple-Lorentzian line-shape function (Equation 2.14) needs to be slightly modified:

$$\Lambda_{123}(\omega_L, \omega_{MW}) = \frac{1}{\omega_{23} - \omega_L - \omega_{MW} + i f_b \gamma_{23}} \cdot \left\{ \frac{\rho_{33}^{(0)} - \rho_{11}^{(0)}}{\omega_{13} - \omega_L + i\gamma_{13}} + f_s \frac{(\rho_{22}^{(0)} - \rho_{11}^{(0)})(\omega_{21} - \omega_{MW})}{(\omega_{21} - \omega_{MW})^2 + (\gamma_{21})^2} \right\}, \tag{5.20}$$

where the population difference $(\rho_{22}^{(0)} - \rho_{11}^{(0)})$ was assumed to be zero for the absorption component, since it is fully saturated. The dispersion component was multiplied with the scaling factor f_s, since partial saturation of the EPR dispersion modifies the ground state populations. The additional broadening factor f_b represents the experimental fact, that the magneto-optical lines (first resonance denominator in Equation 5.20) are broader than the optical lines (second resonance denominator).

With the Equations 2.16 and 5.20 we can predict the expected shape of the ODEPR signal of the R_2 line of ruby. The calculation has to be done for all three-level subsystems of the 8 level system $\psi_{g,e;n}(n = 1..8)$. Two

computer programmes were written by Marc Oliver Schweika-Kresimon [68] for the calculation of ODEPR signals of the R lines of ruby and to fit such a calculation to the experimental data.

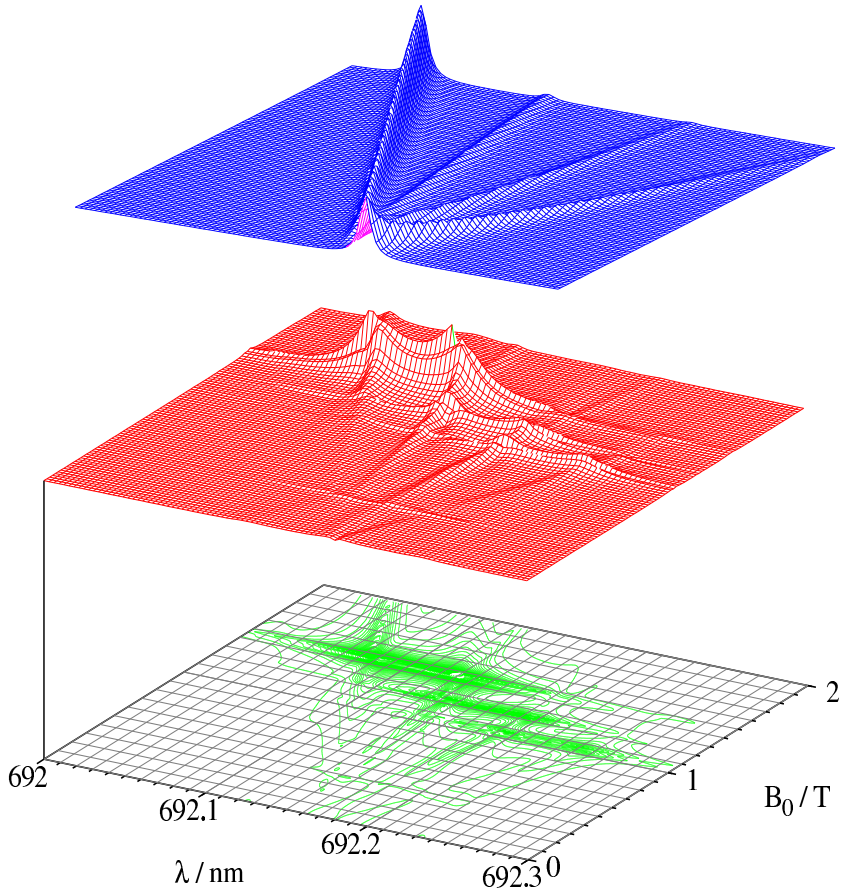

Figure 5.21: Predicted ODEPR (red surface, arbitrary units) of the R_2-line of ruby as a function of wavelength λ and magnetic field B_0. The green lines show the projection of the 3 dimensional red surface onto the λ-B_0-plane as contour lines. The ODEPR is shown in arbitrary units as an absolute amplitude ($\sqrt{x^2+y^2}$), rather than both quadrature phases x and y. The blue surface indicates the optical absorption for the same model.

A prediction for the 35 GHz ODEPR signal can be made under the assumption that all experimental parameters, but the microwave frequency and the magnetic field, are as found at 14 GHz. Such a prediction was calculated with the parameters, which we found earlier [6] (see also Table 5.5). The result is shown in Figure 5.21. It is presented as the absolute value, rather

than two separate phases, since we are interested in the positions on the field and wavelength axes, where we would expect ODEPR. In the experiment, the phase is arbitrary. The figure shows signal contributions from magnetic resonances parallel to the wavelength axis, crossed by four 'oblique' optical contributions.

The prediction is used to set the wavelength and magnetic field range of the experiment.

Experimental

The experimental determination of the wavelength dependence of 35 GHz ODEPR is obstructed by a poor signal to noise ratio. However, ODEPR has been measured for several wavelengths of the R_2-line.

Qualitatively three of the predicted microwave resonances are found, the small resonance at low field is not observed. Depending on the wavelength the signal decreases and increases qualitatively as predicted. It comes as a surprise, however, that the optical contributions seem to be missing.

Attempts were made, to fit the spectra. The calculation depends on 62 parameters (Table 5.5), which can selectively be fitted or kept constant.

Single 35 GHz spectra can be fitted nicely to the theory, when the γ_{ij} are kept constant at the values found at 14 GHz. In this case most of the fits result in a negative sign for f_s. While I cannot find any physical argument for this 'wrong' sign, it is absolutely needed to follow the direction of high and low field resonances, when the optical relaxation rates are kept at the 14 GHz values. However, similar shapes can be simulated by changes in the optical relaxation rate: the overlapping of optical and magnetic contributions can invert the resonances, which looks like a 180° phase change of one magnetic resonance relative to the others.

A simultaneous fit of spectra at different λ would be useful. Since the microwave phase varies between the measured spectra, a simultaneous fit of all experimental data seemed impossible. However, for 18 spectra between 692.048 nm and 692.225 nm the phase φ was fitted as the only parameter for each spectrum individually. With this rather crude estimate, the spectra could be used for simultaneous fits.

Parameters like T, ν, λ, which were determined during the experiment, were not fitted in order to minimise the number of necessary variable parameters. g-values were taken from the literature and transition matrix elements from the theory. The remaining 20 parameters are a pre-factor, the optical linewidths γ_{ij} as well as the magnetic linewidth γ^{mag} and the factors f_b and f_s, which all have a strong influence on the lineshape. However, a simultaneous fit was not possible, since not all transitions are relevant for the ODEPR

index	parameter	14 GHz [6]	fitted	35 GHz
1—16	μ_{ij}^{+}	see [6]	no	see [6]
17—32	μ_{ij}^{-}	see [6]	no	see [6]
33	γ_{51}	$16.473 \cdot 10^9 \mathrm{s}^{-1}$	no	$1.00 \cdot 10^{13} \mathrm{s}^{-1}$
34	γ_{52}	$10.244 \cdot 10^9 \mathrm{s}^{-1}$	no	$1.00 \cdot 10^{13} \mathrm{s}^{-1}$
35	γ_{53}	$17.690 \cdot 10^9 \mathrm{s}^{-1}$	no	$1.00 \cdot 10^{13} \mathrm{s}^{-1}$
36	γ_{54}	$56.972 \cdot 10^9 \mathrm{s}^{-1}$	no	$1.00 \cdot 10^{13} \mathrm{s}^{-1}$
37	γ_{61}	$13.263 \cdot 10^9 \mathrm{s}^{-1}$	no	$1.00 \cdot 10^{13} \mathrm{s}^{-1}$
38	γ_{62}	$11.046 \cdot 10^9 \mathrm{s}^{-1}$	no	$1.00 \cdot 10^{13} \mathrm{s}^{-1}$
39	γ_{63}	$17.040 \cdot 10^9 \mathrm{s}^{-1}$	no	$1.00 \cdot 10^{13} \mathrm{s}^{-1}$
40	γ_{64}	$5.244 \cdot 10^9 \mathrm{s}^{-1}$	no	$1.00 \cdot 10^{13} \mathrm{s}^{-1}$
41	γ_{71}	$15.973 \cdot 10^9 \mathrm{s}^{-1}$	yes	$3.92 \cdot 10^{13} \mathrm{s}^{-1}$
42	γ_{72}	$10.961 \cdot 10^9 \mathrm{s}^{-1}$	yes	$2.18 \cdot 10^{13} \mathrm{s}^{-1}$
43	γ_{73}	$15.111 \cdot 10^9 \mathrm{s}^{-1}$	no	$1.00 \cdot 10^{13} \mathrm{s}^{-1}$
44	γ_{74}	$9.614 \cdot 10^9 \mathrm{s}^{-1}$	no	$1.00 \cdot 10^{13} \mathrm{s}^{-1}$
45	γ_{81}	$11.376 \cdot 10^9 \mathrm{s}^{-1}$	yes	$2.85 \cdot 10^{11} \mathrm{s}^{-1}$
46	γ_{82}	$5.525 \cdot 10^9 \mathrm{s}^{-1}$	yes	$7.67 \cdot 10^{11} \mathrm{s}^{-1}$
47	γ_{83}	$15.535 \cdot 10^9 \mathrm{s}^{-1}$	no	$1.00 \cdot 10^{13} \mathrm{s}^{-1}$
48	γ_{84}	$23.370 \cdot 10^9 \mathrm{s}^{-1}$	no	$1.00 \cdot 10^{13} \mathrm{s}^{-1}$
49	λ	as measured	no	as measured
50	ν	as measured	no	as measured
51	γ^{mag}	$2.165 \cdot 10^9 \mathrm{s}^{-1}$	yes	$1.161 \cdot 10^9 \mathrm{s}^{-1}$
52	T	as measured	no	as measured (~ 1.6 K)
53	φ	arbitrary	no	fitted individually
54	pre-factor	arbitrary	yes	arbitrary units
55	f_s	1.318	yes	2.24
56	f_b	1.253	yes	0.469
57	$g_x^{(1)}$	0.1335	no	0.1335
58	$g_z^{(1)}$	-2.44	no	-2.44
59	$g_x^{(2)}$	0.0394	no	0.0394
60	$g_z^{(2)}$	1.48	no	1.48
61	B_0 offset	arbitrary	no	-120 G
62	signal offset	arbitrary	no	0.0

Table 5.5: ODEPR parameters of ruby. $\mu_{ij}^{\pm}$: transition matrix element; γ_{ij}: optical linewidths; λ: optical wavelength; ν: microwave frequency; γ^{mag}: magnetic linewidth; T: temperature; φ: phase angle; f_s: saturation factor; f_b: broadening factor; $g_{x,y}^{(1,2)}$ spectroscopic splitting factors ('g-values') for the 2 R-lines. 'as measured' means for the respective spectrum.

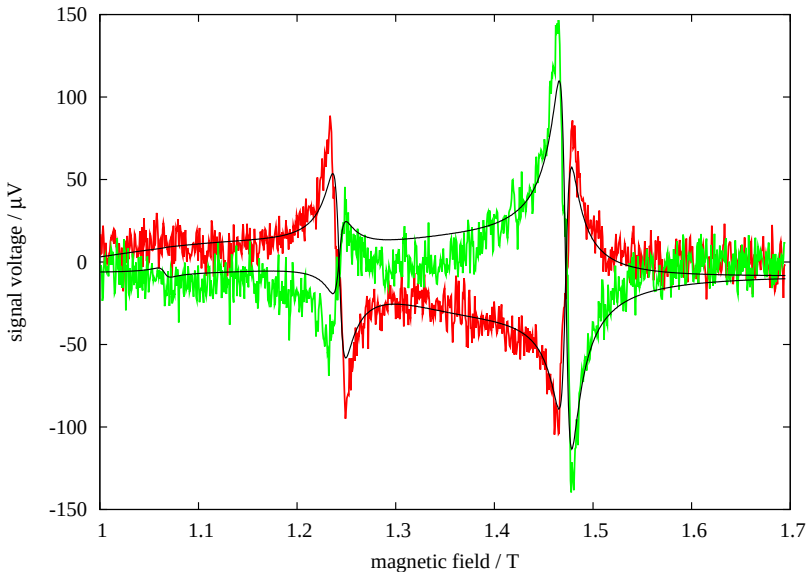

Figure 5.22: ODEPR of ruby I at $\lambda = 692.159$ nm. The black lines shows a fit with $\gamma^{\mathrm{mag}} = 1.10 \cdot 10^9 \mathrm{s}^{-1}$, $\varphi = 52.81°$, $f_s = -0.538$, $f_b = 2.313$. Other parameters as found at 14 GHz (Table 5.5).

signal.

Since optical contributions were not observed experimentally, all optical γ_{ij} were arbitrarily set to $10^{13}\frac{1}{s}$, to make their contribution negligible. At 14 GHz it was found [68], that especially at 692.08 nm the main contribution to the ODEPR signal arises from the 3 level systems $\psi_{g;1}$, $\psi_{g;2}$, $\psi_{e;7}$ and $\psi_{g;1}$, $\psi_{g;2}$, $\psi_{e;8}$. In this wavelength region we expect a strong optical contribution at high field for the 35 GHz experiment. Assuming that these two 3 level systems are the most relevant in our case, γ_{71}, γ_{72}, γ_{81}, and γ_{82} were included as fit parameters. This is of course a very rough approximation only, but it makes a simultaneous fit possible.

The result of the simultaneous fit is compared to the experimental data for two examples in Figure 5.23. The upper spectrum shows a wavelength of 692.072 nm, where we would expect some optical contribution at high field. In the calculation the absence of such contribution corresponds to the very large values for γ_{ij}. In the lower spectrum the wavelength is 692.126 nm. Obviously the simultaneous fit does not represent the phases correctly at low field for this wavelength. I attribute this to the fact, that some more optical contribution would be needed for this single spectrum in the low field region.

However, from the simultaneous fit we can draw at least the qualitative

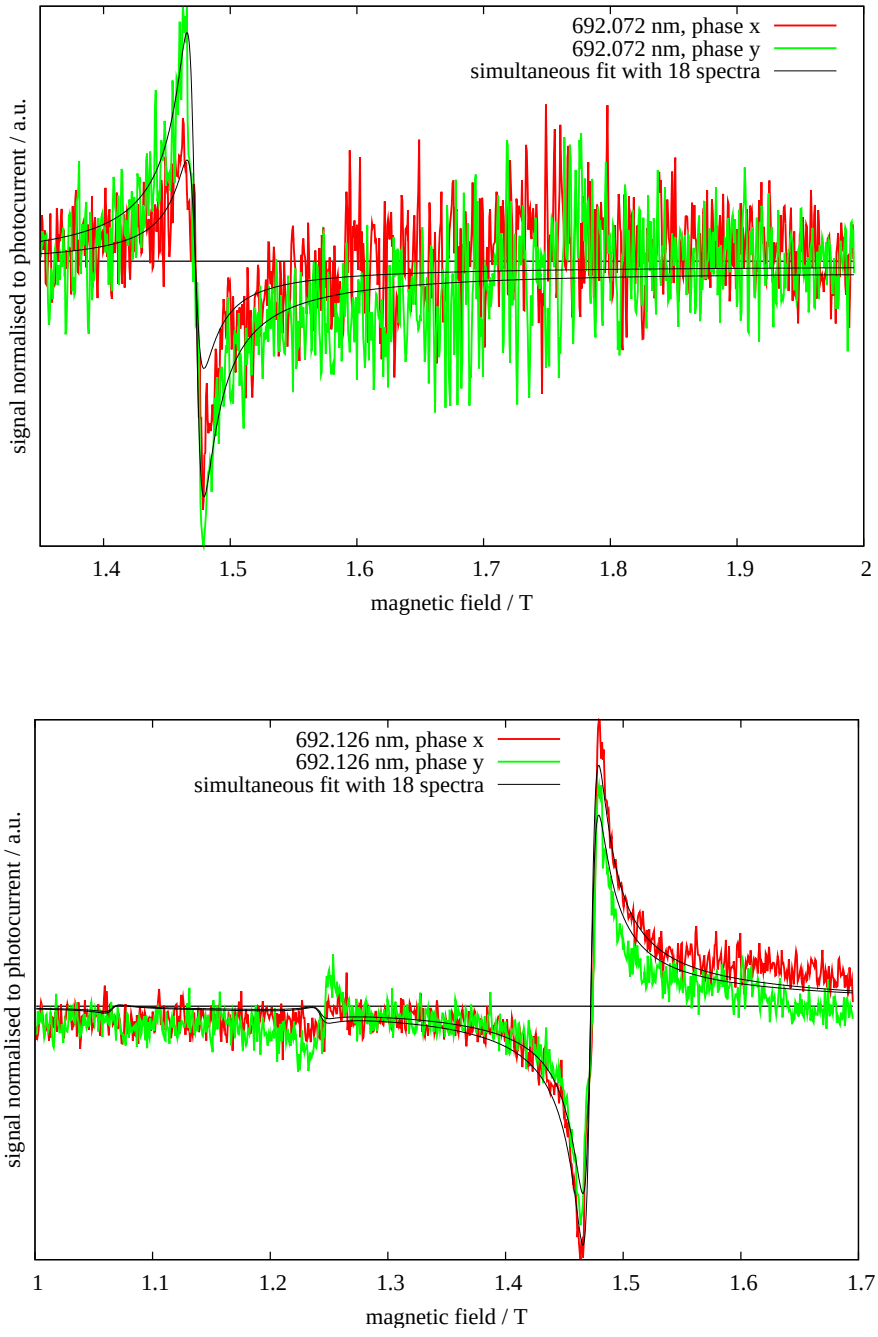

Figure 5.23: ODEPR of ruby I at $\lambda = 692.072$ nm and $\lambda = 692.126$ nm.

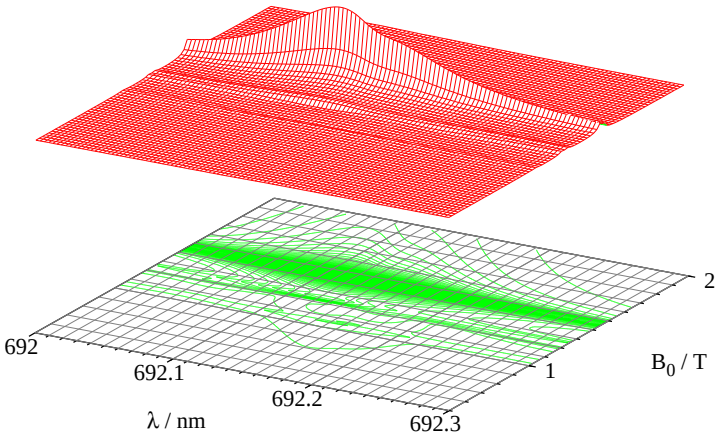

Figure 5.24: Fit result of 35 GHz ODEPR.

conclusion, that the spectra can be interpreted in the coherent Raman picture under the assumption, that the optical relaxation rates increase drastically from 14 to 35 GHz ODEPR. Furthermore we can calculate with these new parameters the result for the 35 GHz ODEPR wavelength and field dependence, which is shown in Figure 5.24. In order to compare it to Figure 5.21 and for reasons of clarity the phase information is not contained in Figure 5.24. Instead the absolute value is plotted.

Bearing in mind the difficulties to fit the experimental data, this figure can only be interpreted as a qualitative result. We can see, however, that the 35 GHz ODEPR of the R_2-line of ruby shows less features than predicted from the parameters obtained with 14 GHz ODEPR. Within the coherent Raman model this can be attributed to bigger optical relaxation rates. A physical explanation for this behaviour has yet to be found. The relaxation rates depend strongly on temperature and concentration, but both experiments have been performed at pumped helium temperatures between 1.5 and 2 K. Moreover the concentration of the two samples is similar: at 14 GHz, sample 3 with $5 \cdot 10^{-4}$ Cr:Al was used, while sample I for the 35 GHz experiments has a concentration of $4 \cdot 10^{-4}$ Cr:Al.

Chapter 6

Pulsed Microwave Excitation

6.1 Optically detected saturation recovery

Optically detected saturation recovery (ODSR, Section 2.3.1) can be measured with the 14 GHz spectrometer (Section 5.1) with some modifications. ODSR has been done to measure the spin-lattice relaxation T_1 of ruby.

The experimental set-up is depicted in Figure 6.1. Most components are identical with those in the ODEPR set-up in Figure 5.1. The main difference is, that I introduced a microwave switch in the excitation arm. When high power is needed, an additional travelling wave tube amplifier (TWTA) is also placed in the excitation arm. Besides, the reference arm and main mixer from the ODEPR set-up (Figure 5.1) are not needed, since ODSR is not a coherent experiment. Furthermore this is a longitudinal experiment, with the magnetic field along the direction of light propagation. This requires a different resonator, which is detailed elsewhere [68]. Our AFC system (Section 5.3) cannot be used with pulsed microwave excitation.

In the experiment laser light at 692 nm is modulated between left and right circularly polarised. The MCD of a ruby sample is measured with a photodiode. The electrical signal is demodulated with a lock-in amplifier and passed to an oscilloscope. Alternatively the optical excitation can be done with a linear polarisation, which contains both circular components at the same time. In this case, the two circular components are separated with the help of a quarter wave-plate and a polarising beam splitter behind the sample and measured with a difference detector. This method has the advantage, that it is not bandwidth limited by the PEM modulation.

The MCD signal can be destroyed with microwave excitation, while the oscilloscope is triggered to the pulse generator. Figure 6.2 shows the destruction and recovery of the MCD of ruby. Here the MCD was destroyed with a

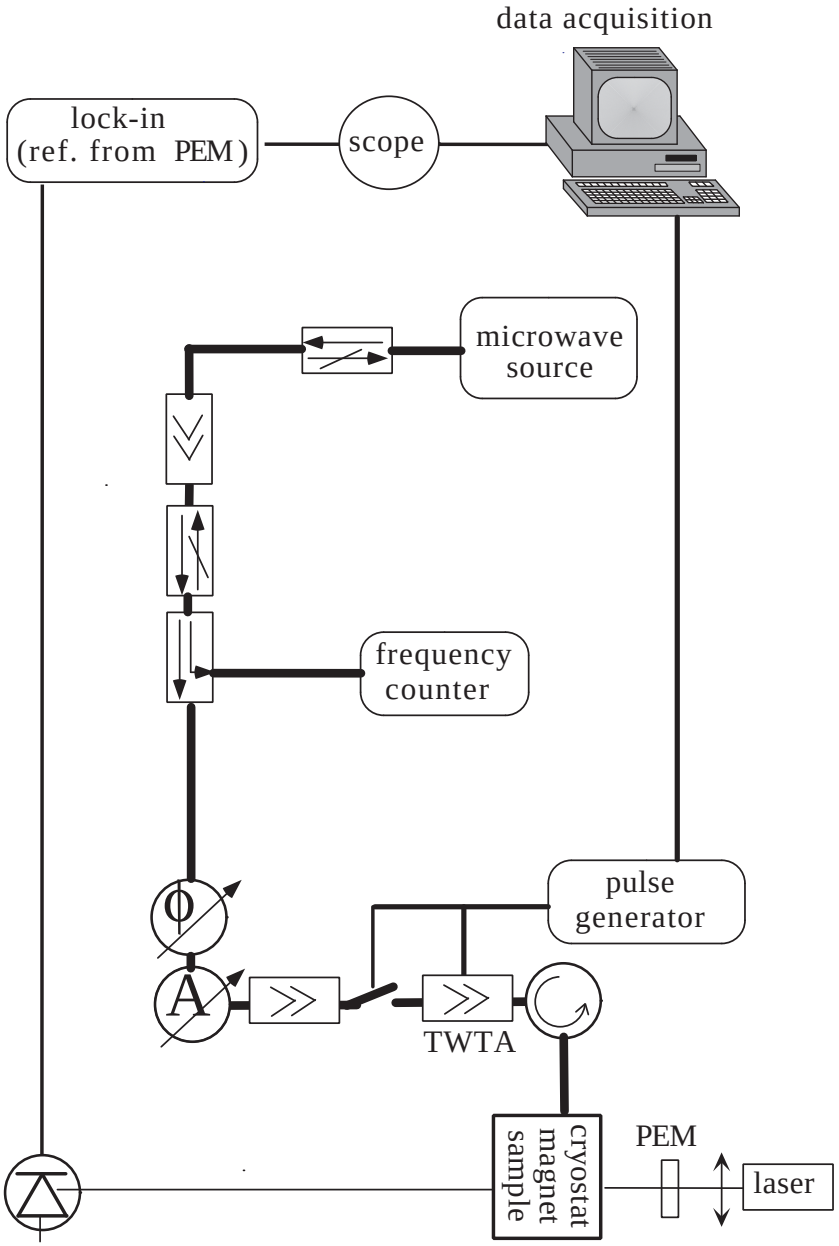

Figure 6.1: Experimental set-up for optically detected saturation recovery.

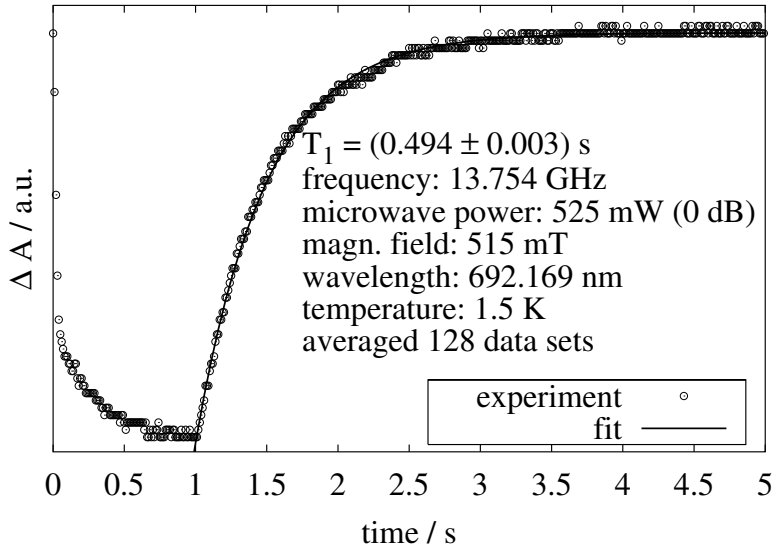

Figure 6.2: ODSR of Ruby sample 3. Parameters are given in the figure.

525 mW excitation of 1 s duration. The recovery time of half a second was determined by fitting it with equation 2.18 and an additional offset.

When a series of long pulses, each of length τ_p, is used to saturate the spin-system, each pulse reaches only a small frequency band, while it reaches a broader spectrum, when τ_p is smaller. The saturation with long τ_p leads to spin diffusion effects, which in turn lead to a reduced value for T_1.

This was tested experimentally: Short, high power pulses of length τ_p separated by an inter pulse delay τ_{ip} were used. τ_p dependent measurements confirm a tendency of T_1 to decrease with longer τ_p, as expected with increased spin-diffusion.

Temperature dependence of T_1 was measured in liquid helium. The temperature T was determined with the vapour pressure of He. With a series of 1000 pulses of $\tau_p = 16$ ns and $\tau_{ip} = 16$ μs the MCD was destroyed and T_1 was determined from the recovery as above. The pulse power was 1 kW. Figure 6.3 shows the result, which confirms a linear dependence on reciprocal temperature, as expected from direct processes.

Spin-lattice relaxation in ruby under our experimental conditions happens in about half a second.

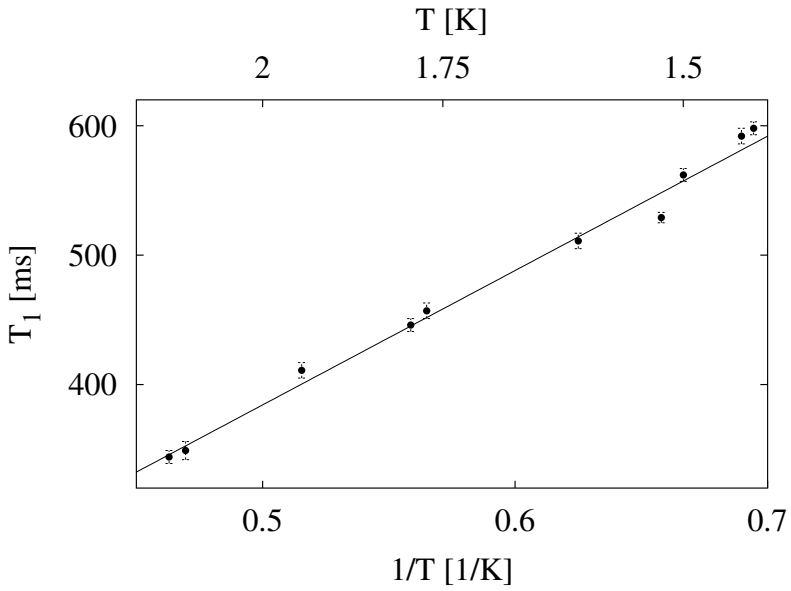

Figure 6.3: Temperature dependence of Ruby ODSR.

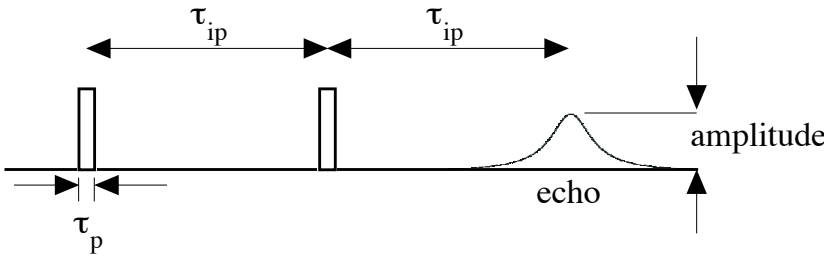

Figure 6.4: Pulse Sequence for T_2 measurements.

parameter	ruby 3	ruby I
resonator	'ODEPR´	'dielectric´
T	1.56 K	1.60 K
B_0	688 mT	696 mT
ν	13.3 GHz	13.6 GHz
τ_p	28 ns	28 ns
number of spectra	60	65
accumulations per spectrum	40	100
points per spectrum	5000	5000
T_2 (from fit)	(433 ± 5) ns	(604 ± 8) ns

Table 6.1: Parameters of the echo decay experiments on ruby.

6.2 Conventionally Detected Pulse EPR

With some modifications [31] to the 14 GHz spectrometer, it is also possible to measure pulse EPR [30] with conventional electronic detection. Spin echo experiments have been performed, to measure the phase memory time T_2, which determines also the ODEPR signal size (Equation 2.5).

Figure 6.4 shows the pulse sequence. The first pulse flips the magnetisation by some angle, the spins de-phase, and after the inter pulse delay τ_{ip} the second pulse refocusses the spins again, so that the echo appears after another period of length τ_{ip}. It was found experimentally [31] that it is favourable in our instrument to use two pulses of the same length. After each 2-pulse sequence a waiting time τ_w is introduced, in which the magnetisation can recover. As a rule of thumb, $\tau_w \geq 5T_1$, since the magnetisation recovers with a time constant T_1. Here, T_1 is about half a second (Section 6.1). After τ_w the 2-pulse sequence is repeated with an incremented τ_{ip}. Finally the echo amplitude can be displayed vs τ_{ip} to document the decay.

Two-pulse echo experiments have been done for sample ruby 2 with the 14 GHz ODEPR resonator and for sample ruby I with a dielectric resonator [31]. A list of our ruby samples can be found in Table 3.1. The experimental parameters are summarised in Table 6.1.

The resulting echo amplitudes M are displayed vs τ_{ip} in Figures 6.5 and 6.6 for ruby 3 and I respectively. The experimental data were fitted with the function

$$M(\tau_{ip}) = M_0 \, e^{-\frac{2\tau_{ip}}{T_2}} \tag{6.1}$$

Phase memory times of about half a microsecond were found (Table 6.1).

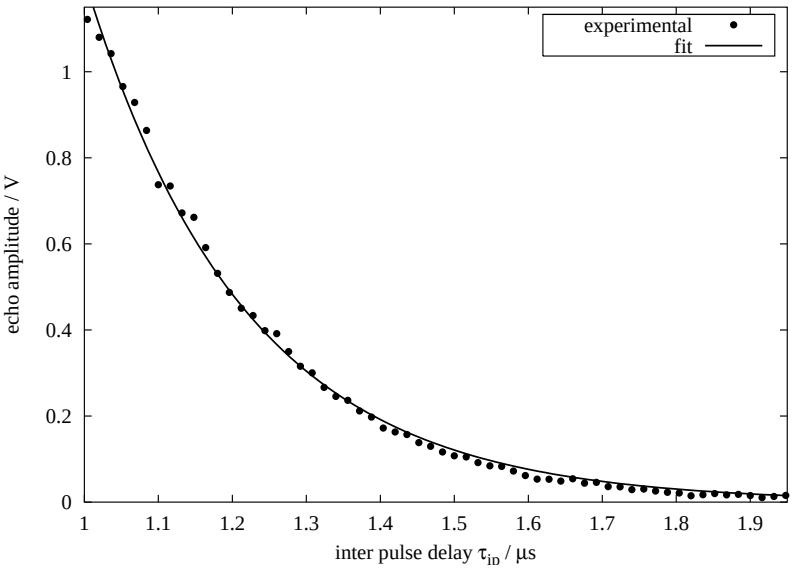

Figure 6.5: Decay of the echo amplitude for ruby 3 yields $T_2 = 433$ ns.

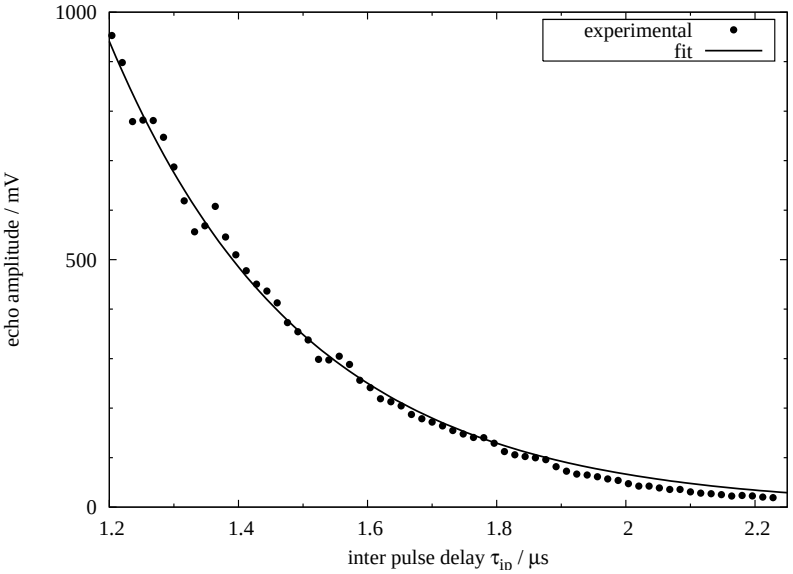

Figure 6.6: Decay of the echo amplitude for ruby I yields $T_2 = 604$ ns.

Chapter 7

Summary and Future Prospects

7.1 Conclusion

ODEPR is a relatively young technique and not many ODEPR spectrometers exist. With this thesis a spectroscopic toolbox for the investigation of electronic structure has been created and a theory of ODEPR in the coherent Raman picture has been developed*.

In particular, the newly created facilities comprise the complete re-implementation of 14 GHz ODEPR and the new 35 GHz ODEPR spectrometer. This has been the first successful attempt to do ODEPR at such a high microwave frequency. A new TE_{011}-mode microwave cavity has been developed for this spectrometer.

With $12\frac{\mu V}{\sqrt{Hz}}$ the noise of the 35 GHz spectrometer is comparable to that of the 14 GHz spectrometer, whereas the measured signals are smaller at 35 GHz. This leads to a poorer signal-to-noise ratio.

Furthermore conventional continuous wave EPR of a metalloprotein has been measured in the ODEPR spectrometer for the first time, which is an important step towards a successful ODEPR measurement of unknown samples. Also MCD has been implemented as a helper tool for ODEPR.

Additionally, first steps were made towards a coherent Raman detected ODEPR with pulsed microwave excitation. The extension of the spectrometer for pulse EPR has been planned and first measurements have been performed. With pulse techniques spin-lattice relaxation times of about half a second have been found for a ruby sample, while phase memory times of the order of half a microsecond have been determined in the same substance.

Measurements of myoglobin (Mb) MCD revealed two Gaussian bands, which had not been described by other authors. The measurements can also

*Theory in collaboration with M. O. Schweika-Kresimon, published elsewhere [6].

be considered as a successful test of the MCD spectrometer. Also the possibility to measure conventional EPR with the ODEPR equipment has been demonstrated with Mb. In these measurements g-values from the literature have been confirmed.

35 GHz ODEPR measurements on the R_2 line of ruby have shown the expected linear dependence on light power as well as on the square root of microwave power. Wavelength dependent measurements have given the surprising result, that optical as well as magneto-optical contributions are not found as predicted. In the calculation this can be simulated by very high relaxation rates for the optical transitions, which, however, remains to be explained.

7.2 Outlook

The long term aim must clearly be to further establish ODEPR as a common tool for the investigation of electronic structure of metalloproteins, for which we have already demonstrated its potential at 14 GHz. The 35 GHz hardware offers new possibilities in terms of resolution of g-tensor anisotropy. Here lies the greatest potential of the technique.

The hardware can be improved by introduction of an amplifier in the excitation arm, which would increase the signal without effecting the noise. For consistent measurements of both quadrature phases, a quadrature mixer would be helpful. Furthermore this would half the data acquisition time. With an improved signal-to-noise ratio the analysis of possible optical and magneto-optical contributions to the 35 GHz ruby ODEPR signal should be tackled again.

Moreover, application of the theory in the coherent Raman picture to metalloproteins might give new insights into the microscopic details especially for high spin systems, where the rotating MCD picture is not valid.

In order to find proper applications in biological systems a collaboration with other groups with a background from biochemistry could be very fruitful.

I want to encourage everyone to try to make this sophisticated technique handier, so that it will more readily be used by spectroscopists, who still refrain from it.

Appendix A

Design Drawings

In this appendix design drawings of certain parts of the various spectrometers are summarised. Complete drawings can be found in the drawing office under the given reference number. Some of the details in the overview drawings might not come out clearly in the printout. These details are nevertheless included and can be zoomed bigger in the digital version of this thesis.

A.1 Changes to the MCD Spectrometer

Figure A.1 shows an overview of the design changes made to the MCD spectrometer described in section 4.1.1. The design was made in the drawing-office of our Physics department.

The main part of the spectrometer, including the monochromator, was placed on a new support (parts 20 to 31 in the figures) in order to bring it to the correct height for the optical table and the cryostat windows. Further, the sample compartment was removed. Instead the monochromator is connected to the cryostat windows with an adapter tube (parts 5 and 11). A similar construction holds the photomultiplier tube on the other side of the cryostat. A tiny plastic tube, part 14, is used to de-mist the windows with nitrogen which evaporates from the reservoir of the cryostat.

The sensitive parts of the spectrometer, i.e. the photomultiplier (PM) tube, the xenon lamp, and the photoelastic modulator (PEM) were shielded from the magnetic field. The PM was shielded with a μ-metal tube (not shown) provided by Jasco. The iron shields of the PEM and the lamp are shown in Figure A.2.

Detailed drawings are available in the drawing-office of our department under the reference number e3.866.8.01.

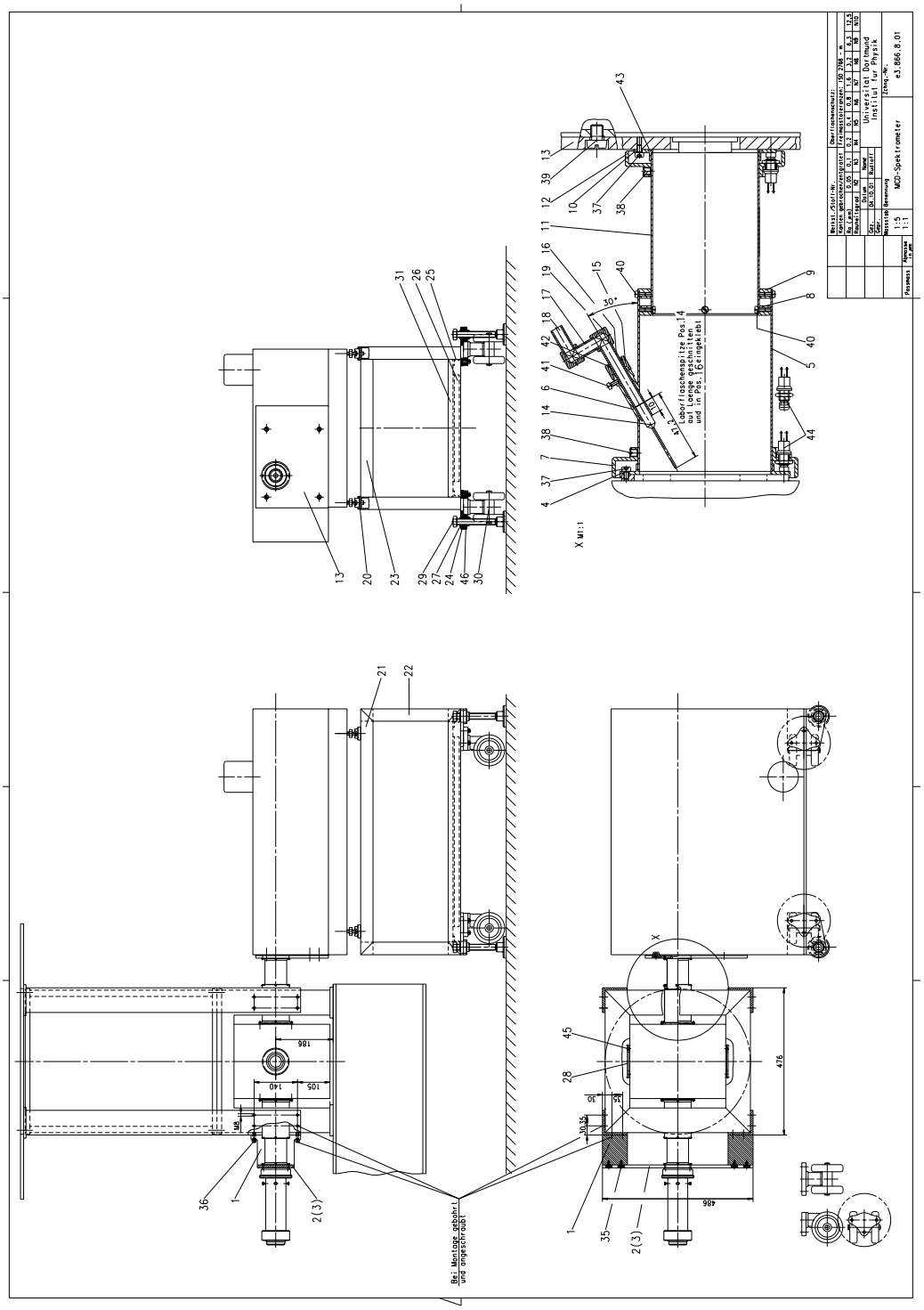

Figure A.1: Overview of the changes made to the Jasco MCD spectrometer.

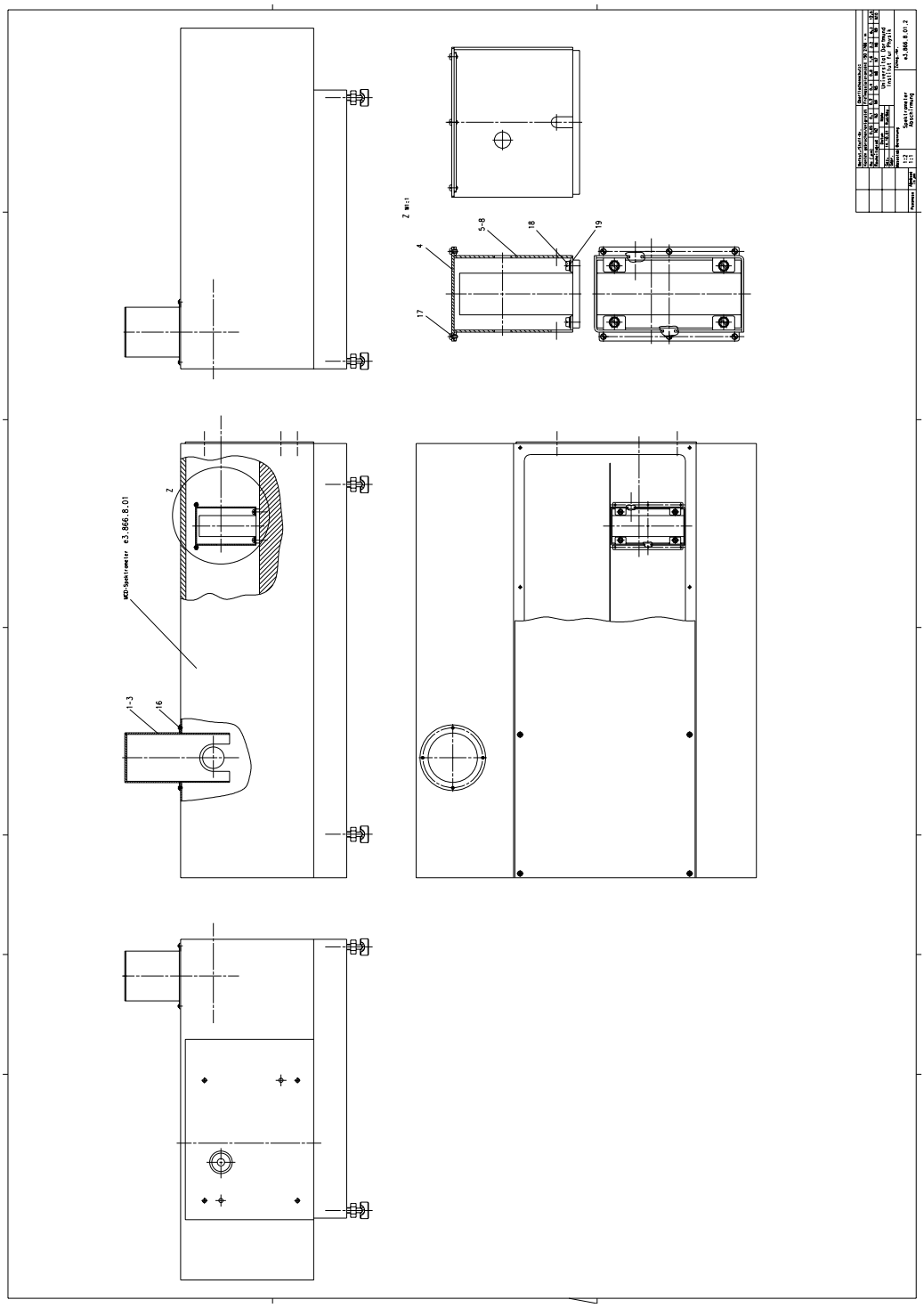

Figure A.2: Shielding the Jasco MCD spectrometer from the magnetic field.

A.2 35 GHz Spectrometer

A.2.1 35 GHz Bridge

Figure A.3 shows an overview design drawing of the main bridge of the 35 GHz ODEPR spectrometer. The part numbers relate this overview to the detailed drawings with the reference number e3.882.1.02 in the drawing office.

The top of the figure shows a top view of the cryostat, where parts 19-22 make the waveguide connection to the probe, which is described in Section A.2.2. Parts 35-36 of the waveguide can be replaced by a slide-screw tuner, which is detailed in Section A.2.3.

Microwaves are produced in the tuneable source 57 of the rectangular bridge. The heart of the bridge is the optical heterodyne detection arm with the phase shifter 55, mixer 53, low noise amplifier 52, isolator 51, and photodiode 50.

The excitation arm goes through the couplers 56, 58, 60 and circulator 61. The output of coupler 60 can be used for frequency measurements.

The AFC-system gets conventional EPR input from the detection diodes 63 and 66 on the right hand side of the bridge. The signal on diode 66 can be mixed with microwaves from the reference arm (in the centre of the bridge) via coupler 65.

A.2.2 35 GHz Probe

The design considerations for the 35 GHz cavity are described in Section 5.2.2. The resulting design is shown here. Figure A.4 shows the dimensions of the cavity itself in detail.

Figure A.5 shows the complete probe. There is a big box (upper left corner), which can hold plugs for electrical connections of the hall-probe, field modulation and helium level meter. The wave-guide in the probe ends at the top of this box, where it is sealed with a thin plastic foil (not shown) and some vacuum grease. The wave-guide from the spectrometer (not shown) is flanged on the top of the big box which is in turn flanged onto the cryostat (indicated below the o-ring at the bottom of the box). 945 mm lower is the optical access to the microwave cavity. In the middle of the cavity the sample holder with the optical cuvette (parts 47-48) for the metalloprotein solution can be seen. For ruby measurements, the crystal replaces the complete cuvette. The necessary gap in the copper at the place, where the sample holder is attached to the wall, was made to be close to a quarter wavelength, in order to prevent microwave leakage. Part 44 is the movable wall of the resonator, which allows frequency tuning by means of a screwdriver.

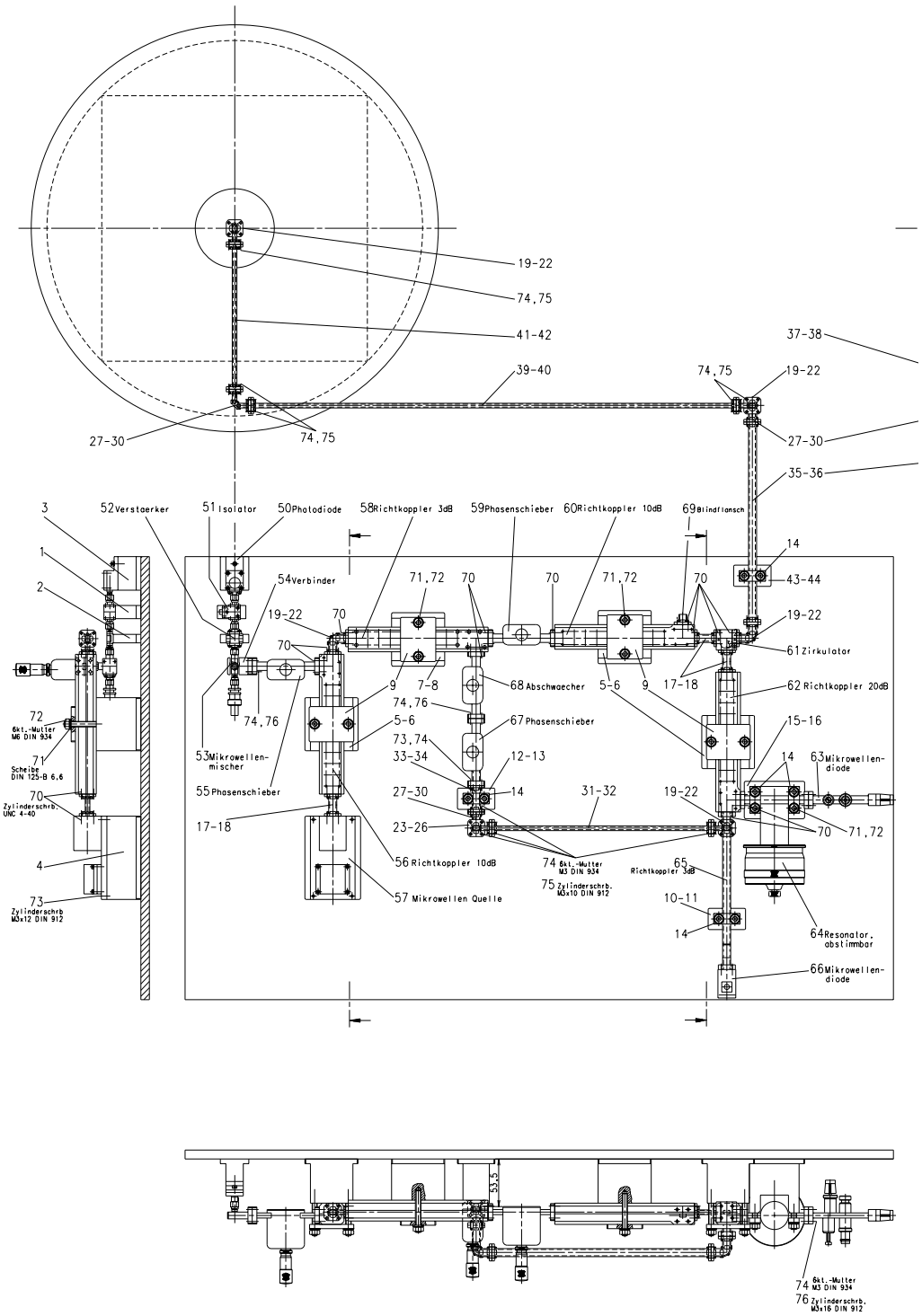

Figure A.3: Overview of the 35 GHz ODEPR bridge.

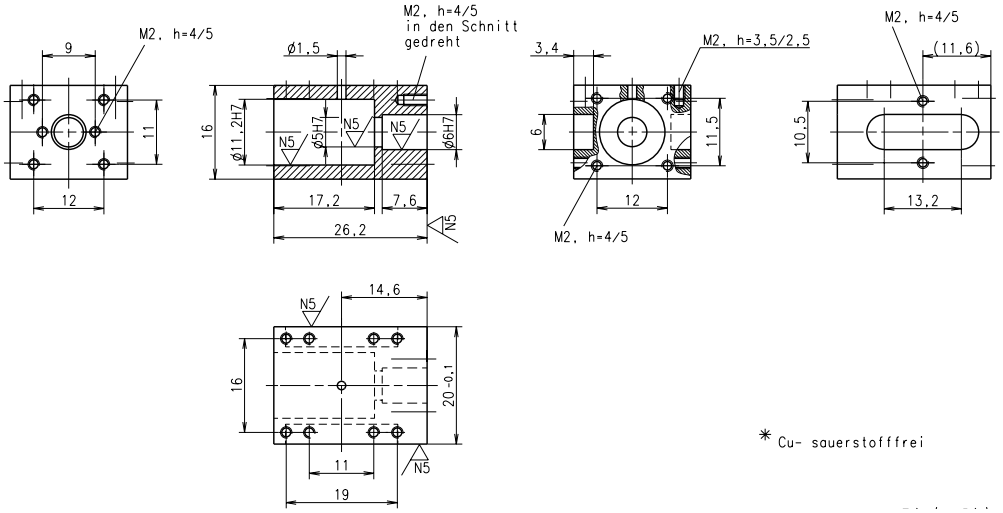

Figure A.4: Microwave cavity at the lower end of the 35 GHz probe.

The upper right drawing in this figure shows a view in which the tuning mechanism (similar to [63]) can be seen better. The long mechanism of lever arms provides a means to adjust a little coupling pin right above the cavity. This pin goes into the wave-guide directly above the circular iris, which provides the coupling to the cavity, as described in Section 5.2.2.

In the drawing most to the right, a side view of the cavity shows an oval shape, where the cavity wall is thinner to allow better field modulation. The holder for the modulation coils can be seen on the side of the cavity in the drawing most to the left.

The upper wave-guide part of the probe is made of stainless steel in order to reduce thermal conductivity. The high frequency electrical conductivity is re-established with gold plating.

More detailed drawings are available in the drawing-office of our department under the reference number e3.939.01.03. The original design of the complete probe, which is not detailed here, has the reference number e3.769.1.99.

A.2.3 Slide Screw Tuner

A slide screw tuner (cp. chapter 4G in [60]) is a devices which introduces reactance and susceptance into a transmission line by means of a movable pin introduced to the longer wall of a waveguide. It can be used as an

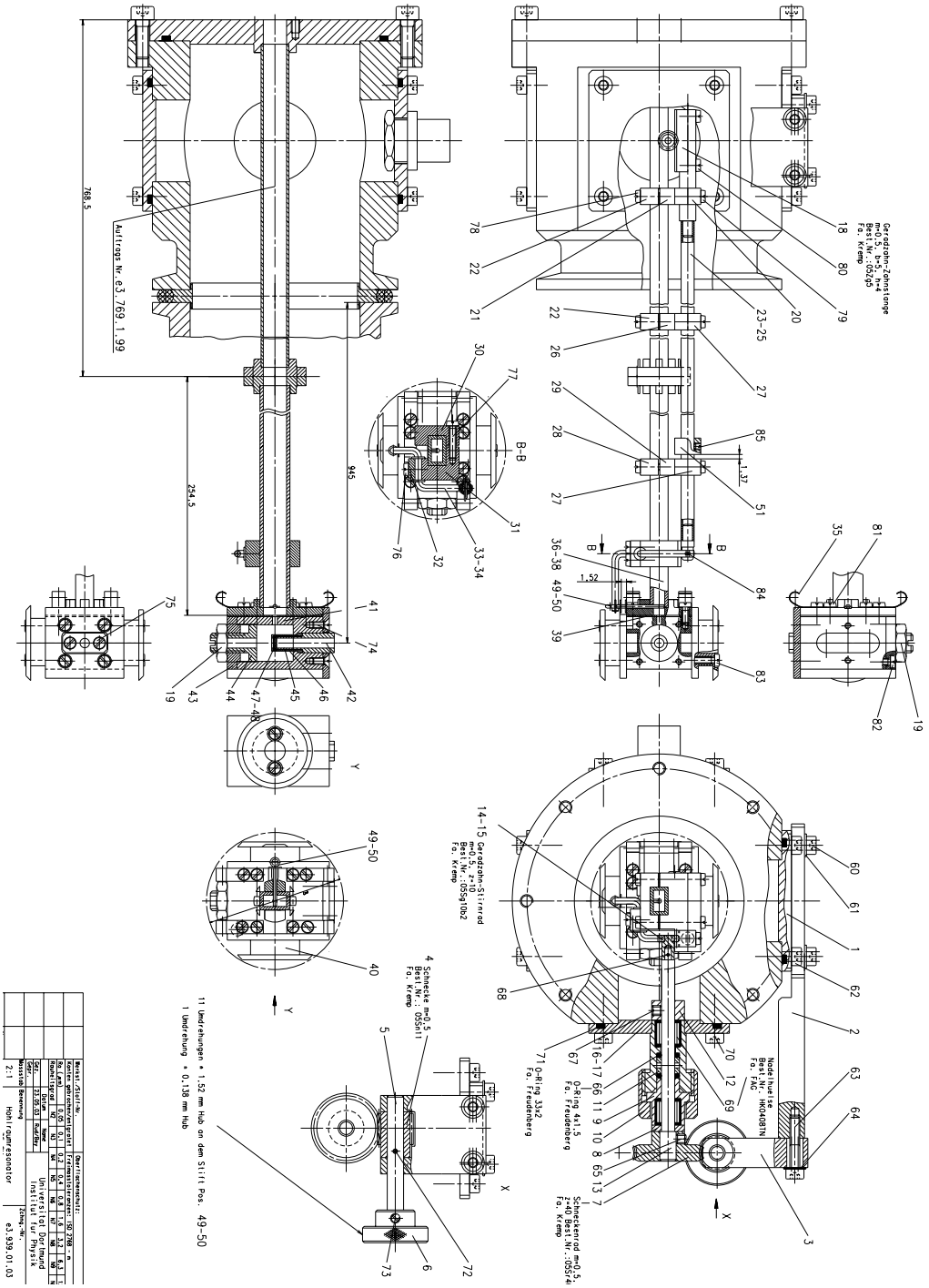

Figure A.5: Overview of the 35 GHz probe for ODEPR and conventional EPR.

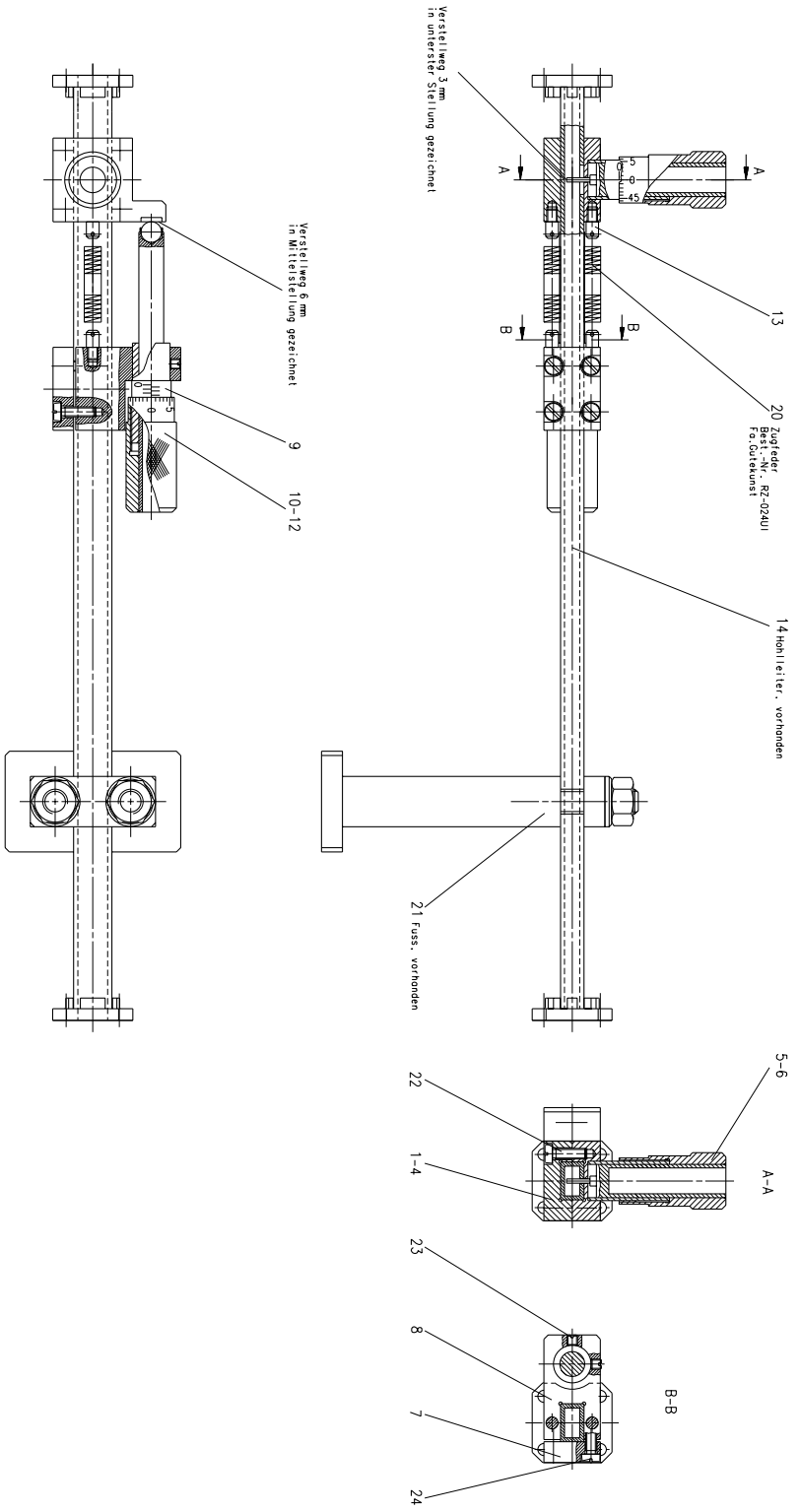

Figure A.6: Slide screw tuner.

impedance matching device.

At the frequency of 35 GHz commercial devices were not available. Figure A.6 shows the design drawing of our slide screw tuner. The stainless steel pin was gold plated in the preparation lab for better electrical conductivity.

The design fits into the microwave bridge, where it replaces parts 35-36 (Figure A.3).

Appendix B

Electrical Components

B.1 Electrical Circuitry of the AFC-system

The circuit diagrams of the electronics of the AFC are summarised here for convenience.

For the AFC system, I needed to build an 11 kHz phase shifter. Its circuit diagram is shown in Figure B.1. The concept was taken from [69]. The resistor and operational amplifier on the left are for impedance match between the AFC box and the all pass filter. The other components make up the all pass filter (cp. [69], chapter 13.10.2) which is used as a variable phase shifter here. Further information on electronic design can be found elsewhere [70, 66].

The AFC box was developed by Norbert Koch from the electronics workshop. Details of the circuitry are shown in Figures B.2 and B.3.

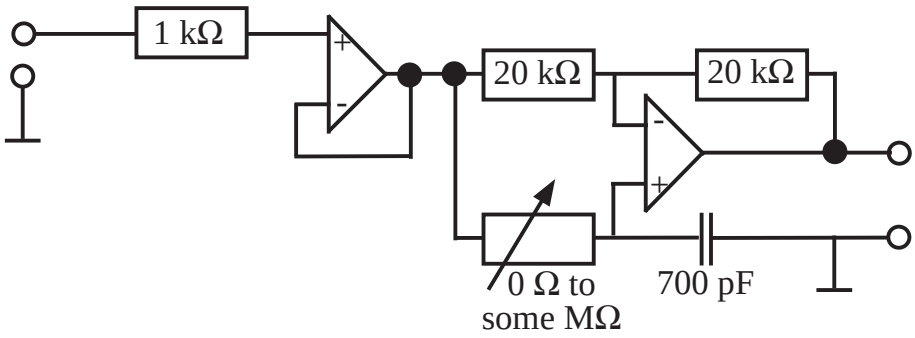

Figure B.1: 11 kHz Phase Shifter.

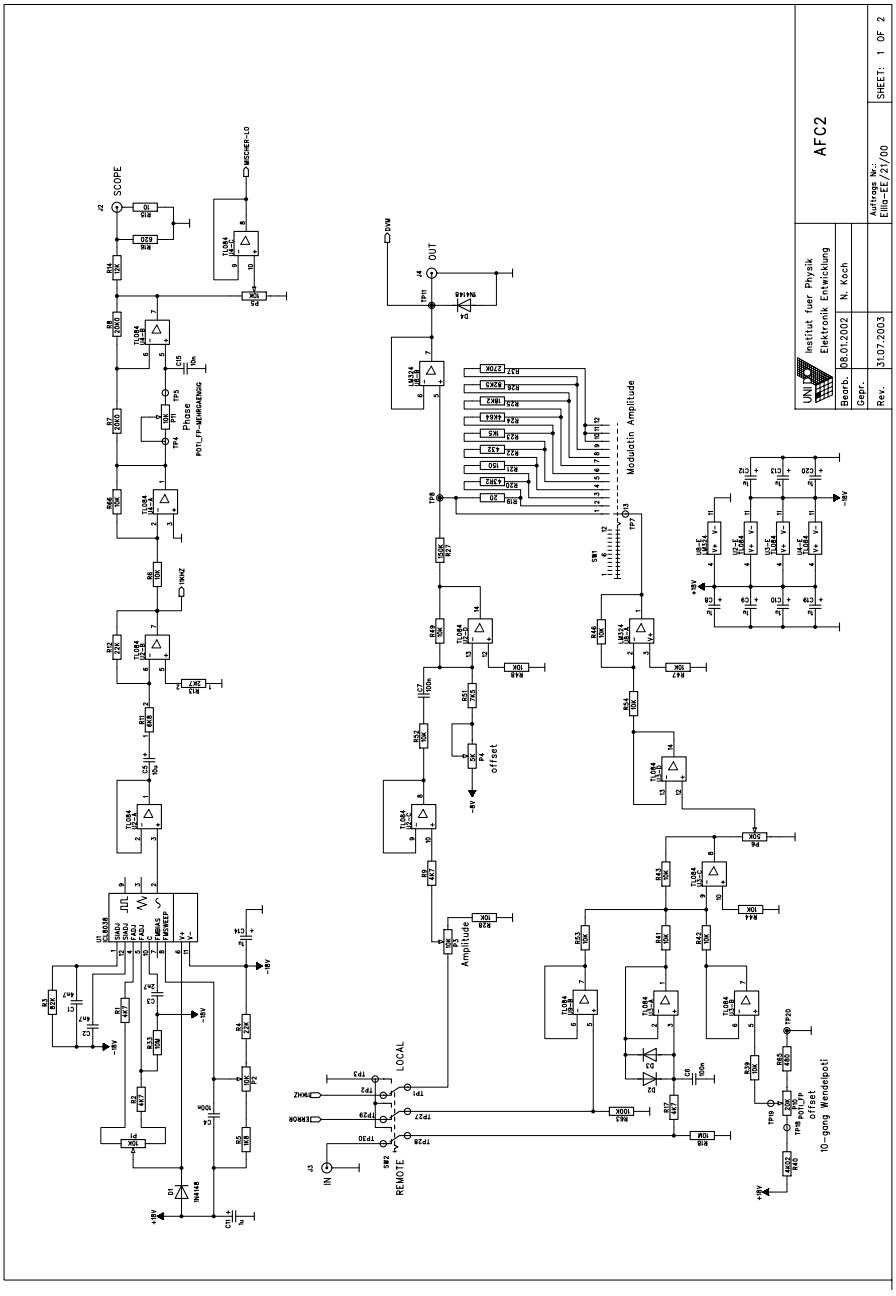

Figure B.2: AFC circuit diagram, page 1 of 2. This part creates the modulation signal with variable offset and amplitude.

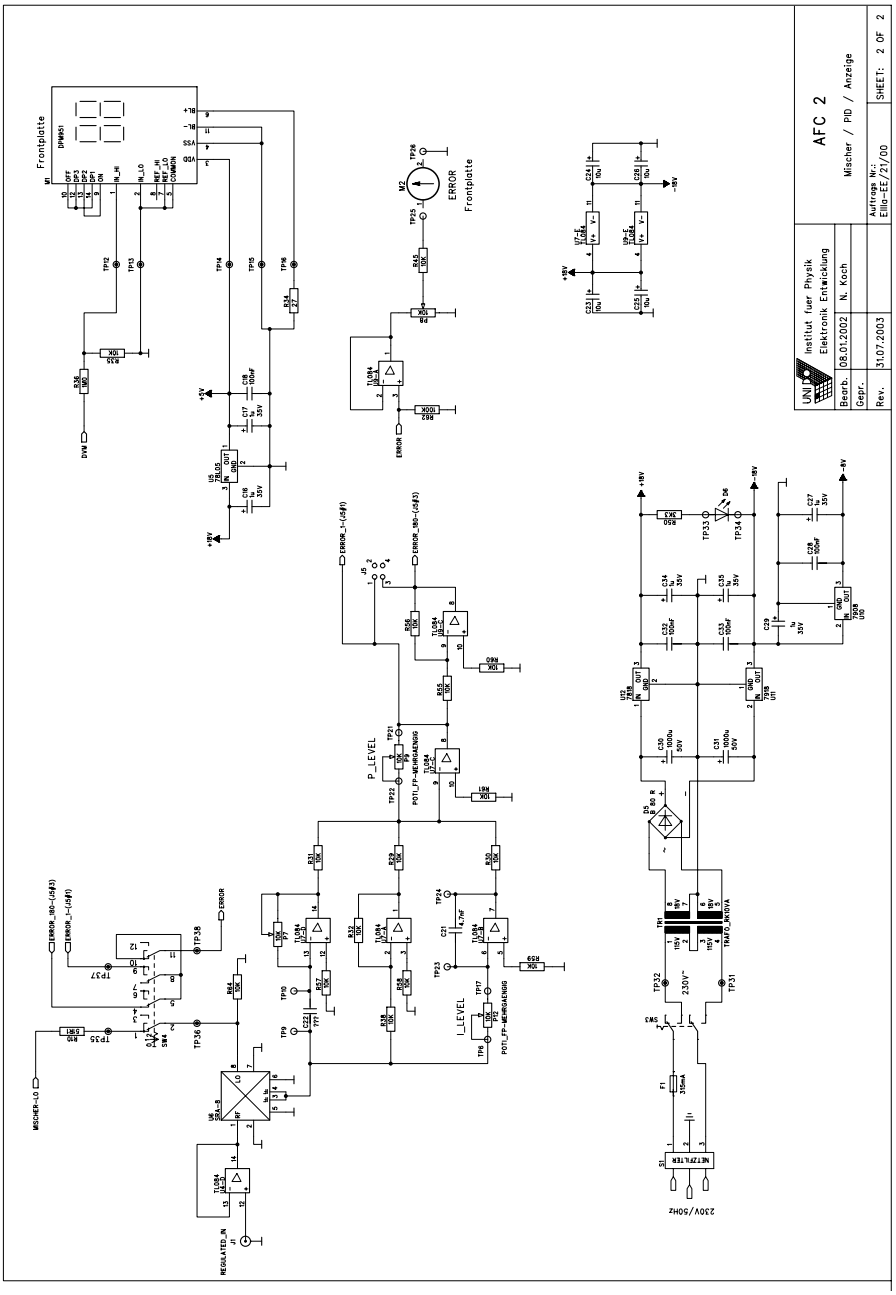

Figure B.3: AFC circuit diagram, page 2 of 2. This part contains the phase sensitive detection with a mixer and PID-controller. Further it displays the offset voltage.

B.2 Microwave Parts

Details on the manufacturers and models of the microwave components together with some calibration data are summarised here for convenience.

B.2.1 35 GHz

part no.	distributor	manufacturer	model	serial no.
1	Parzich	MWO	28ET100-35	105
2	Semic	Quinstar	QJR-A10300	5047002
2A	Semic	Quinstar	QAS-A00000	5047006
2B	Semic	Quinstar	QWA-2800-BK	135
2C	Parzich	Miteq	M3435	587953
2D	Parzich	Miteq	JSD4-34353565 -38-10P	592787
2E	unknown	PAMTECH	PTA-1267-2	1429-0438
2F	Laser 2000	New Focus	NFI-1004	2506
3	Semic	Quinstar	QJR-A03300	5047003
3A	Semic	Quinstar	QAL-A00000	4766115
3B	Semic	Quinstar	QAS-A00000	4766114
4	Semic	Quinstar	QAL-A00000	5047007
5	Semic	Quinstar	QJR-A10300	5047001
5A	Pro Nova	XLM	3400A	120635536
6	unknown	PAMTECH	RYB2046 A113-110	55387
7	Semic	Quinstar	QJR-A20300	5047008
7A	unknown	mid century	unknown	39218
7B	Semic	mri	DETR-X	102
8	unknown	unknown	unknown	unknown
9	Semic	mri	DETR-X	102

Table B.1: Microwave part list of the 35 GHz Spectrometer. Parzich GmbH, Pürgen; MWO: millimeter-wave oscillator company, Longmont USA; Semic RF Taufkirchen; Quinstar Technology Inc., Torrance, CA, USA; Miteq Inc. Hauppauge New York USA; Pro Nova Nachrichtentechnik GmbH, Ludwigsburg; XLM: XL Microwave Inc., Oakland, CA, USA; PAMTECH, USA; Laser 2000 GmbH, Wessling; New Focus, San Jose, CA, USA; mid century microwave gear;

The microwave components of the 35 GHz spectrometer are related to their manufacturers in Table B.1. The numbers refer to the same components as

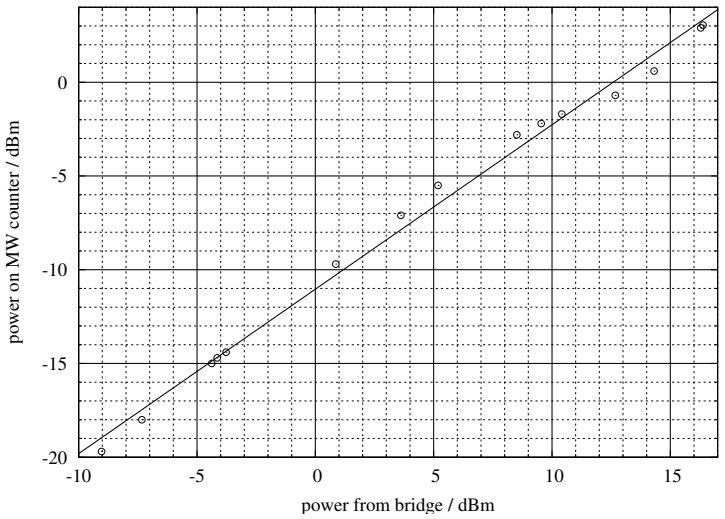

Figure B.5: Power on microwave counter vs bridge output power.

those in Figure 5.2 and Table 5.2. The full company name and the city are given, under the table, when known. The companies can be contacted via the distributors and details can be found on the internet. Further specifications can be found in the manual collection of our group in manual number 143.

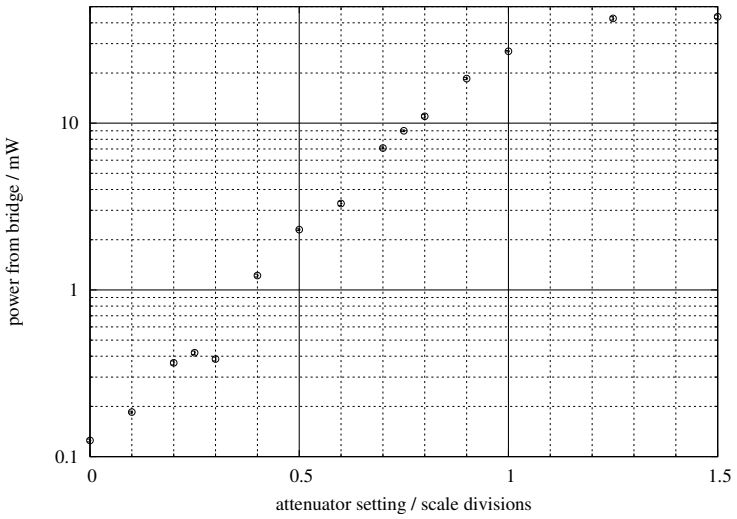

Figure B.4: Microwave output power for different attenuator settings.

With attenuator 4 the power output from the microwave bridge to the probe can be adjusted. Figure B.4 shows the resulting power for different attenuator settings. It can also be convenient, to monitor the output power from the bridge by means of the power measurement function of the microwave counter connected to directional coupler 5. Figure B.5 shows the reading of the microwave counter's power meter for the respective output power from the bridge, i.e. on the top of the probe. The voltage response of the diodes 7B and 8 was measured for different input powers. It is shown in Figure B.6.

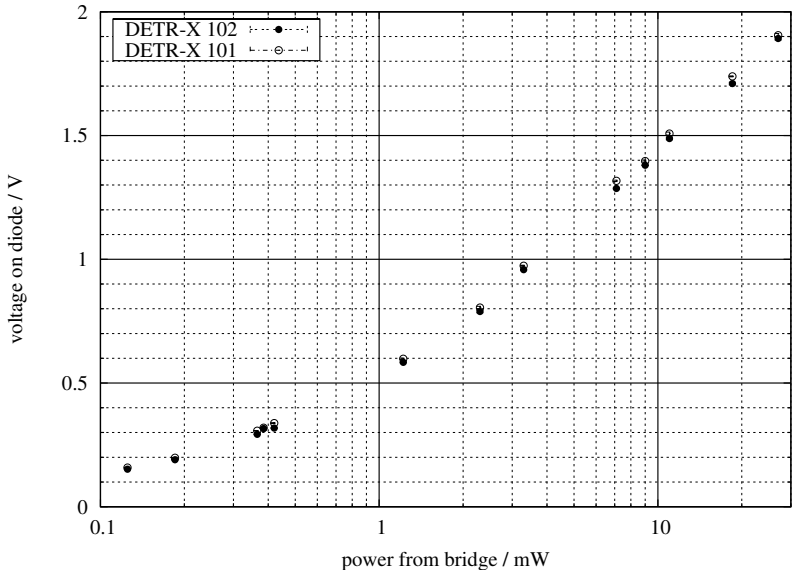

Figure B.6: Voltage response of the microwave diodes.

B.2.2 14 GHz

Specifications of the 14 GHz components can be found in the data sheets with manual number 142 in the manual collection of our group. Manufacturers and distributors of the components are summarised in Table B.2 . The numbers in this table refer to the same items as those Figure 5.1 and Table 5.1.

part no.	distributor	manufacturer	model	serial no.
6	Laser 2000	New Focus	1437M	0244
7	Parzich	RYT	202718	10
8	Parzich	Miteq	AMF-4F-134141-12	669790
9	Parzich	Miteq	OTC-1CM-134-141-15P-AFC	656795
10	Parzich	RYT	200219	188
11	unknown	GHz	A3207-10 Rev. 4	23448R1-1 12-99
12	unknown	Anaren	250129	9519 0026
13	IE	MA-Ltd	AL 28-13.4-14.1-12	2525
14	Parzich	RYT	200219	187
15	unknown	mac technology	CA206820G	699002
15 a	Pro Nova	XL microwave	3260	960230696
16	Pro Nova	ARRA	9428B	7913
17	unknown	GHz	A3207-10 Rev. 4	23448R1-2 12-99
18	MBMT	HP	382A	670
19	IE	MA-Ltd	AL 7-13.4-14.1-30-30	001 2523
20	unknown	Quest MW	SR1314C11	9950
21	Semic	ARRA	9426B	2122
22	Parzich	MCLI	CA8-20	229
23	IE	MA-Ltd	AL 18-13.4-14.1-20	001 2216
24	unknown	Pulsar microwave	IDOH-D8-458	0023
24 a		home made		
25		home made		
26		Stanford Research	SR-830	23602, 36808

Table B.2: Microwave part list of the 14 GHz Spectrometer. Laser 2000 GmbH, Wessling; New Focus, San Jose, CA, USA; Parzich GmbH, Pürgen; RYT Industries; Miteq Inc. Hauppauge New York USA; Anaren Microwave Inc.; IE industrial electronics GmbH, Eschborn; mac technology inc. USA; Pro Nova Nachrichtentechnik GmbH, Ludwigsburg; XL Microwave Inc., Oakland, CA, USA; ARRA Inc., Bay Shore, NY, USA; MBMT Messtechnik, Bassum; HP: Hewlett-Packard; Quest Microwave Inc., Morgan Hill, CA, USA; Semic RF, Taufkirchen; Pulsar Microwave Corporation, Clifton, NJ, USA; Stanford Research Systems Inc., Sunnyvale, CA, USA.

B.3 Modelling the Cylindrical Cavity

Since the experimental behaviour of the final cavity design could not fully be understood analytically, an attempt was made to calculate its electromagnetic properties numerically.

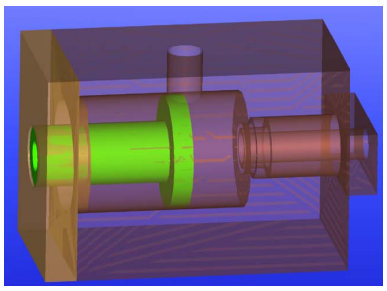

Figure B.7: Three dimensional model of the cylindrical microwave cavity. The green part is the tuning plunger, which changes the length of the cavity.

In Section 5.2.2 the 35 GHz microwave cavity was explained in terms of an analytical model, assuming a hollow cylinder with perfectly conducting walls either homogeneously filled with liquid helium or no dielectric at all. A more realistic model has to include the exact geometry including optical access holes and microwave coupling iris, the tuning plunger, the finite conductivity of the copper walls, the geometry and dielectric constant of the sample holder and the sample itself.

Such a model was made and Robert Stonies from the *Lehrstuhl für Hochfrequenztechnik* implemented it with the software *Microwave Studio*.

First simulations did not include the sample holder and sample, but only the copper cavity with no dielectric inside. With the so called transient solver of the software, a frequency swept excitation between 30 and 40 GHz was simulated for 6 different cavity lengths in the tuning range of the design with a cavity radius of $R = 5.6$ mm. The resulting frequency of the resonance peaks is plotted vs. cavity length together with the analytically calculated mode frequencies (Equations 5.1, 5.2) in Figure B.8. The simulation is indicated by black dots. As a guide to the eye, those points of the simulation which seem to belong to the same mode are connected by black lines. That TM modes are suppressed, as explained earlier, is confirmed by the simulation. We can see that the frequency of the simulation is below the analytical calculation. This can qualitatively be understood by the fact that additional holes for the optical access make the cavity bigger than the perfect cylinder assumed for the analytical solution. A bigger resonance structure leads to a lower resonance frequency.

There are some resonances in the simulation, which cannot be understood as one of the modes from the analytical solution. These arise from the complicated geometry of the cavity. When the eigenmode solver is used to calculate field distributions, one can see that the fields are sometimes concentrated, for instance, on the wrong side of the plunger, i.e. outside the cavity.

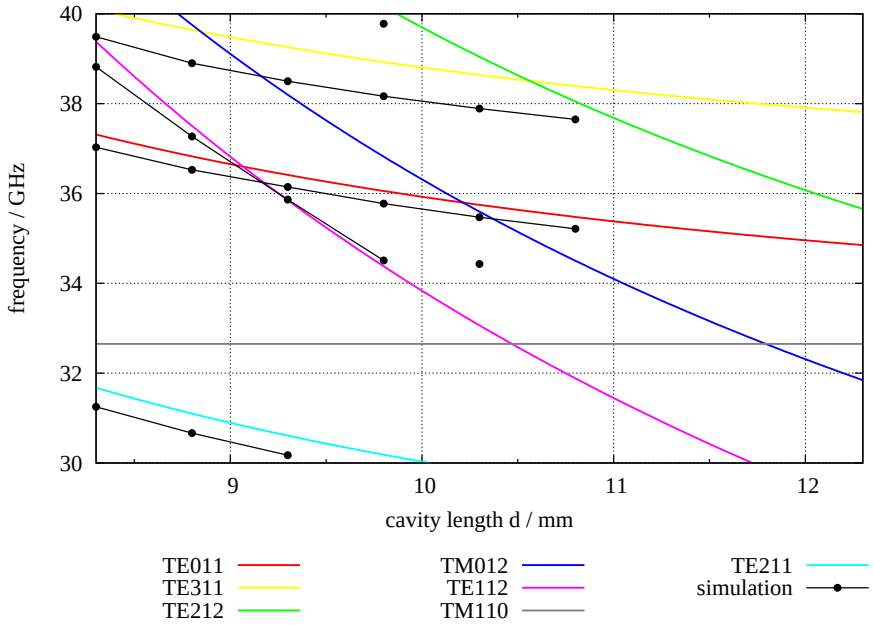

Figure B.8: Simulated cavity resonances compared to analytical modes.

This leads to resonances, which do not exist for a perfect cylinder.

Additionally, the eigenmode solver was used to calculate field distributions for a cavity length of 8.3 mm. From these we could identify which is the TE_{011} mode and check that the frequencies correspond to the findings from the transient solver.

The next step was the inclusion of holder and ruby sample in the simulation. The holder is made of Q 200.5 with a dielectric constant of 2.5, whereas the dielectric constant ϵ_r of ruby is somewhere between 7.5 and 11.5*. We assumed $\epsilon_r = 9$ for ruby. With these additional dielectrics in the cavity, the TE_{011} mode resonance frequency goes down to 27.999 GHz, even with the shortest possible cavity length of 7.9 mm†. This is far away from the spectrometer range. We also found, that the fields are mostly concentrated in the ruby crystal.

This effect is considerably less strong for my first cavity design with $R = 7$ mm, because the electric field distribution is the same for both designs, but for $R = 5.6$ mm the fields are more concentrated, as shown in Figure B.9. In this figure the field amplitudes are shown in a colour code, where red indicates

*www.goodfellow.com

†normal tuning is only possible to 8.3 mm, but when the tightening nut on the plunger is removed it can be slightly smaller

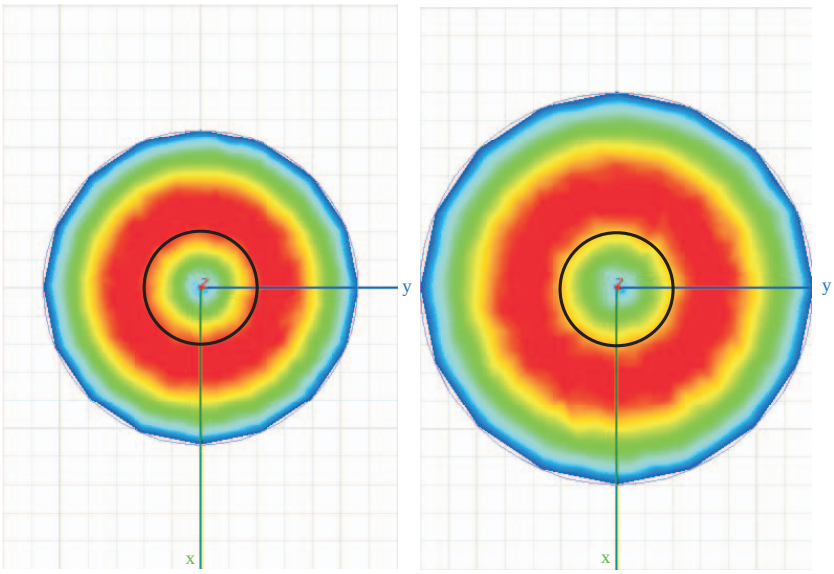

Figure B.9: Electric fields of the TE_{011} mode in a perfectly conducting cylinder. The cylinder on the left has $R = 5.6$ mm, while that on the right has $R = 7$ mm. The black circle indicates the size of our ruby sample. The grid in the background has a spacing of 1 mm.

the strongest field and blue means weak. For clarity the picture shows a simplified model of a perfectly conducting cylinder without any dielectric inside[‡]. In this simple model we can already see, that our ruby sample (its size is indicated with a black circle in the figure) fills a space of more intense fields in the cavity of less radius. In a more detailed model, the field gets even more intense within the ruby crystal.

The result of the numerical calculations is, that for a 35 GHz TE_{011} cavity with $2R \simeq d$ the analytical solution is not sufficient. The resonance frequency needs to be calculated for the exact cavity geometry and for the sample used in the experiment, before a cavity is machined.

[‡]Calculated by Ryszard Narkovicz with the software HFSS from Ansoft.

Appendix C

Myoglobin MCD Data

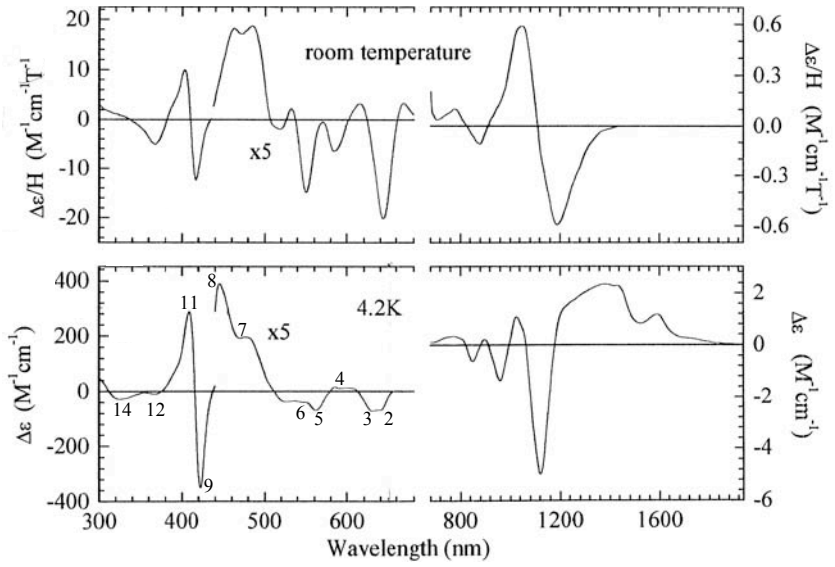

Figure C.1: Myoglobin MCD measured by M. Cheesman. The numbers refer to the features listed in Table 4.1.

Myles Cheesman from the UEA Norwich kindly provided some of his MCD data. His sample was myoglobin from horse skeletal muscle in aqueous solution buffered at pH 5.5. The magnetic field was 5 T. The spectrum is reproduced in Figure C.1.

Bibliography

[1] D. Suter and J. Gutschank. Laser-assisted magnetic resonance: Principles and applications. In *Novel NMR and EPR techniques*. Springer, 2005. to be published.

[2] J. Gutschank, D. Suter, and B. Enkisch. Orientational information from unoriented metalloproteins by optically detected electron paramagnetic resonance. *J. Anal. At. Spectrom.*, 19(1):34–40, 2004.

[3] B. Börger, S. J. Bingham, J. Gutschank, M. O. Schweika, and D. Suter. Optically detected electron paramagnetic resonance by microwave modulated magnetic circular dichroism. *J. Chem. Phys.*, 111(18):8565–8568, 1999.

[4] S. J. Bingham, B. Börger, J. Gutschank, D. Suter, and A. J. Thomson. Probing the electronic structure of transition metal ion centers in proteins by coherent raman-detected electron paramagnetic resonance spectroscopy. *J. Biol. Inorg. Chem.*, 5(1):30–35, 2000.

[5] S. J. Bingham, J. Gutschank, B. Börger, D. Suter, and A. J. Thomson. Magnetic circular dichroism anisotropy form coherent raman detected electron paramagnetic resonance spectroscopy: Application to spin-1/2 transition metal ion centers in proteins. *J. Chem. Phys.*, 113(10):4331–4339, 2000.

[6] M. O. Schweika-Kresimon, J. Gutschank, and D. Suter. Magneto-optical and epr transitions in raman heterodyne spectroscopy. *Phys. Rev. A*, 66(4):043816, 2002.

[7] B. Börger, J. Gutschank, D. Suter, A. J. Thomson, and S. J. Bingham. Deconvolution and assignment of different optical transitions of the blue copper protein azurin from optically detected electron paramagnetic resonance spectroscopy. *J. Am. Chem. Soc.*, 123(10):2334–2339, 2001.

[8] B. Börger and D. Suter. Magnetic and optical anisotropy of clostridium pasteurianum rubredoxin from optical detected electron paramagnetic resonance. *J. Chem. Phys.*, 115(21):9821–9826, 2001.

[9] G. Palmer. *Methods for Determining Metal Ion Environments in Proteins*, volume 2 of *Advances in Inorganic Biochemistry*, chapter 6 Electron Paramagnetic Resonance. Elsevier, 1980.

[10] R. H. Clarke, editor. *Triplet State ODMR Spectroscopy.* John Wiley, New York, 1982.

[11] A. B. Dennison. Magnetic resonance involving the optically excited state. *Magnet. Resonance Rev.*, 2(1):1–33, 1973.

[12] C. P. Barrett, J. Peterson, C. Greenwood, and A. J. Thomson. Optical detection of paramagnetic resonance by magnetic circular dichroism. application to aqueous solutions of metalloproteins. *J. Am. Chem. Soc.*, 108:3170–3177, 1986.

[13] H. G. Dehmelt. Modulation of a light beam by precessing absorbing atoms. *Physical Review*, 105:1924–1925, 1957.

[14] E. W. Bell and A. L. Bloom. Optical detection of magnetic resonance in alkali metal vapor. *Physical Review*, 107:1559–1565, 1957.

[15] N. Bloembergen, P. S. Pershan, and L. R. Wilcox. Microwave modulation of light in paramagnetic crystals. *Physical Review*, 120:2014–2023, 1960.

[16] S. J. Bingham, D. Suter, A. Schweiger, and A. J. Thomson. Optical detection of transition metal ion electron paramagnetic resonance by coherent raman spectroscopy. *Chem. Phys. Letters*, 266:543–547, 1997.

[17] A. Abragam and B. Bleaney. *Electron Paramagnetic Resonance of Transition Ions.* Oxford University Press, London, 1970.

[18] L. J. Berliner, editor. *Spin Labeling. Theory and Applications.* Academic Press, New York, 1976.

[19] S. J. Lippard and J. M. Berg. *Principles of Bioinorganic Chemistry.* University Science Books, Mill Valley, 1994.

[20] J. R. Pilbrow. *Transition Ion Electron Paramagnetic Resonance.* Clarendon Press, Oxford, 1990.

[21] S. B. Piepho and P. N. Schatz. *Group Theory in Spectroscopy with Applications to Magnetic Circular Dichroism*. Wiley, New York, 1983.

[22] P. J. Stephens. Magnetic circular dichroism. *Advances in Chemical Physics*, 35:197–264, 1976.

[23] J. C. Sutherland. Magnetic circular dichroism. *Methods in Enzymology*, 246:110–131, 1995.

[24] A. J. Thomson, M. R. Cheesman, and S. J. George. Variable-temperature magnetic circular dichroism. *Methods in Enzymology*, 226:199, 1993.

[25] R. Bernheim. *Optical Pumping. An Introduction*. Benjamin, New York, 1965.

[26] J. Gutschank. Raman heterodyne detected electron paramagnetic resonance spectroscopy of metalloproteins. Master's thesis, University Dortmund, 1998.

[27] J. A. Giordmaine and W. Kaiser. Light scattering by coherently driven lattice vibrations. *Phys. Rev.*, 144(2), 1966.

[28] R. W. Boyd. *Nonlinear Optics*. Academic Press Inc., San Diego, 1992.

[29] C. Wei, S. A. Holmstrom, N. B. Manson, J. P. D. Martin, X.-F. He, P. T. H. Fisk, and K. Holliday. Raman heterodyne detected magnetic resonance: I. cw and coherent transient measurements. *Appl. Magn. Reson.*, 11:521–538, 1996.

[30] A. Schweiger and G. Jeschke. *Principles of pulse electron paramagnetic resonance*. Oxford University Press, New York, 2001.

[31] M. Meier. Mikrowellengepulste (optisch detektierte) Elektronenspinresonanz. Master's thesis, University Dortmund, 2004.

[32] R. W. G. Wyckoff. *Crystal Structures*, volume 2. John Wiley & Sons, New York, second edition, 1964.

[33] B. Henderson and G. F. Imbusch. *Optical Spectroscopy of Inorganic Solids*. Clarendon Press, Oxford, 1989.

[34] S. Sugano, Y. Tanabe, and H. Kamimura. *Multiplets of Transition-Metal Ions in Crystals*. Academic Press, Inc., New York, 1970.

[35] Birgit Börger. Optically detected electron paramagnetic resonance of ruby and metalloproteins. Master's thesis, University Dortmund, 1998.

[36] R. Winter and F. Noll. *Methoden der Biophysikalischen Chemie*. Teubner, Stuttgart, 1998.

[37] P. W. Atkins. *Physikalische Chemie*. VCH, Weinheim, 2 edition, 1996.

[38] J. C. Kendrew and R. G. Parrish. The crystal structure of myoglobin III. sperm whale myoglobin. *Proc. Roy. Soc. A*, 238:305–324, 1956.

[39] L. Stryer. *Biochemistry*. Freeman, New York, 4 edition, 1995.

[40] M. Weissbluth. *The Physics of Hemoglobin*, volume 2 of *Structure and Bonding*, chapter 1, pages 1–125. Springer-Verlag, 1967.

[41] B. R. James. *Interaction of Dioxygen with Metalloporphyrins*, volume V of *The Porphyrins*, chapter 6. Academic Press, New York, 1978.

[42] E. Antonini and M. Brunori. *Hemoglobin and Myoglobin in their Reactions with Ligands*, volume 21 of *Frontiers of Biology*. North-Holland Publishing Company, Amsterdam, 1971.

[43] A. E. Pond, M. P. Roach, M Sono, A. H. Rux, S. Franzen, R. Hu, M. R. Thomas, A. Wilks, Y. Dou, M. Ikeda-Saito, P. R. Ortiz de Montellano, W. H. Woodruff, S. G. Boxer, and J. H. Dawson. Assignment of the heme axial ligand(s) for the ferric myoglobin (H93G) and heme oxygenase (H25A) cavity mutants as oxygen donors using magnetic circular dichroism. *Biochemistry*, 38:7601–7608, 1999.

[44] M.A. Gadsby and A.J. Thomson. Assignment of the axial ligands of ferric ion in low-spin hemoproteins by near-infrared magnetic circular dichroism and electron paramagnetic resonance spectroscopy. *J. Am. Chem. Soc.*, 112:5003–5011, 1990.

[45] A.J. Thomson and M.K. Johnson. Magnetization curves of haemoproteins measured by low-temperature magnetic-circular-dichroism spectroscopy. *Biochem. J.*, 191:411–420, 1980.

[46] L. Vickery, T. Nozawa, and K. Sauer. Magnetic circular dichroism studies of myoglobin complexes. correlations with heme spin state and axial ligation. *J. Am. Chem. Soc.*, 98(2):343–350, 1976.

[47] S. Yoshida, T. Iizuka, T. Nozawa, and M. Hatano. Studies on the charge transfer band in high spin state of ferric myoglobin and hemoglobin by low temperature optical and magnetic circular dichroism spectroscopy. *Biochim. et Biophys. Acta*, 405:122–135, 1975.

[48] J. Bolard and A. Garnier. Circular dichroism studies of myoglobin and cytochrome c derivatives. *Biochim. Biophys. Acta*, 263:535–549, 1972.

[49] V.S. Oganesyan, S.J. George, M.R. Cheesman, and A.J. Thomson. A novel, general method of analyzing magnetic circular dichroism spectra and magnetization curves of high-spin metal ions: Application to the protein oxidized rubredoxin, desulfovibrio gigas. *J. Chem Phys.*, 110(2):762–777, 1999.

[50] F. Neese and E.I. Solomon. Mcd c-term signs, saturation behaviour, and determination of band polarizations in randomly oriented systems with spin s$\geq$ 1/2. application to s=1/2 and s=5/2. *Inorg. Chem.*, 38:1847–1865, 1999.

[51] U. Damm. Optische Frequenzverdopplung und Magnetooptische Spektroskopie. Master's thesis, University Dortmund, 2002.

[52] P.J. Stephens, W. Suëtaak, and P.N. Schatz. Magneto-optical rotatory dispersion of porphyrins and phthalocyanines. *J. Chem. Phys.*, 44(12):4592–4602, 1966.

[53] T. H. Wilmshurst. *Electron Spin Resonance Spectrometers*. Adam Hilger Ltd., London, 1967.

[54] A. S. Brill, C. I. Shyr, and T. C. Walker. Power saturation of electron paramagnetic resonance from high-spin ferric haemoproteins at 4.2 k. *Molecular Physics*, 29(2):437–454, 1975.

[55] L.C. Dickinson and M.C.R. Symons. Electron spin resonance of haemoglobin and myoglobin. *Chem. Soc. Revs.*, 12:387–414, 1983.

[56] S. J. Bingham, B. Börger, D. Suter, and A. J. Thomson. The design and sensitivity of microwave frequency optical heterodyne receivers. *Rev. Sci. Instrum.*, 69(9):3403–3409, 1998.

[57] T. F. Prisner. Pulsed high-frequency / high-field EPR. *Advances in Magnetic and Optical Resonance*, 20:245–299, 1997.

[58] J. F. Reintjes and G. T. Coate. *Principles of Radar*. McGraw-Hill, New York, 1952.

[59] C. P. Barrett. *Optical-Microwave Double Resonance*. PhD thesis, School of Chemical Sciences, University of East Anglia, Norwich, UK, 1985.

[60] C. P. Poole. *Electron Spin Resonance*. John Wiley, New York, second edition, 1983.

[61] S. Y. Liao. *Microwave Circuit Analysis and Amplifier Design*. Prentice-Hall Inc., Englewood Cliffs, New Jersey, 1987.

[62] J. D. Jackson. *Classical Electrodynamics*. John Wiley, New York, 2nd edition, 1975.

[63] J. E. Whitehouse. EPR cavity matching device for use at low temperatures. *Rev. Sci. Instrum.*, 49(4):541–542, 1977.

[64] A. van der Ziel. *Noise*. Prentice-Hall, Englewood Cliffs, 1970.

[65] D. M. Pozar. *Microwave Engineering*. John Wiley & Sons, New York, 2nd edition, 1998.

[66] K.-H. Rohe. *Elektronik für Physiker*. Teubner, Stuttgart, 3. edition, 1987.

[67] A. M. Portis. Electronic structure of f centers: Saturation of the electron spin resonance. *Phys. Rev.*, 91(5):1071–1078, 1953.

[68] M. O. Schweika-Kresimon. *Optisch Detektierte Paramagnetische Resonanzspektroskopie am Rubin*. PhD thesis, University Dortmund, 2001.

[69] U. Tietze and Ch. Schenk. *Halbleiter-Schaltungstechnik*. Springer-Verlag, Berlin, 5th edition, 1980.

[70] P. Horowitz and W. Hill. *The Art of Electronics*. Cambridge University Press, Cambridge, 1986.

Acknowledgements

I would like to thank a number of people who have encouraged and inspired me during this work.

Firstly, my thanks must go to Professor Suter for giving me the opportunity to work on this fruitful project. The work at EIII has been very autonomous, but always with the chance to rely on the master's support.

Thanks must be extended to the whole workgroup, especially to Birgit Enkisch and Marc Oliver Schweika-Kresimon, with whom I have very closely worked together for a couple of years. We have been a good team and they have always made time for discussions on experiment and theory. Also Marcus Eickhoff, Robert Klieber, and Ryszard Narkovicz deserve credit for their willingness to help in the lab and with computing issues. Further, 'my' diploma students Uwe Damm and Mirko Meier must be mentioned for their hard work and the refreshing coffee breaks.

The teams of all the workshops, especially Gisela Pike from the preparation lab, have been very helpful with their expertise on all the nitty gritty, which is needed for a good experiment.

Further I would like to thank some people from far away, who have helped with comments and suggestions: Professor Andrew J. Thomson, Harriet Seward, and Myles Cheesman from the Centre of Metalloprotein Spectroscopy at the School of Chemical Sciences of the University of East Anglia, Norwich, UK. Also thanks must go to Professor Thomas Prisner for some short but encouraging discussions during a pulse EPR workshop.

Natalie Bleimling from the Max-Planck-Institute Dortmund has also helped me with the sample preparation and Robert Stonies from the *Lehrstuhl für Hochfrequenztechnik* made time for the microwave simulations.

Also many other people have influenced me during this period and thanks must go to all of them, but they are far too many to be named. As an outstanding example I thank especially my friend Marcus Weber, with whom I founded the *Physikanten*. Together we found a new and very encouraging approach to physics. Thanks also to the people, which I do not mention: grazie, ευχαριστώ, danke, спаси́бо.

Last, but not least, I would like to thank my family. Ich danke meinen Eltern, dass sie mir diese Studium ermöglicht und mich immer unterstützt haben. Meiner Lebensgefährtin Светлана Маркова und ihrem Sohn Егор Евсенин danke ich dafür, dass sie so viel Verständnis für meine Arbeit hatten und mein Leben bereichert haben. Unserer Tochter Claudia danke ich, dass sie mich immer wieder aus der Physik zurück ins Leben ruft. Für sie werde ich nun mehr Zeit haben.